THE EFFECT OF NEAR WALL DISTURBANCES ON A COMPRESSIBLE TURBULENT BOUNDARY LAYER

by

Jonathan Gaskins

A Thesis

Submitted to the Faculty of Purdue University

In Partial Fulfillment of the Requirements for the degree of

Master of Science in Aeronautics and Astronautics

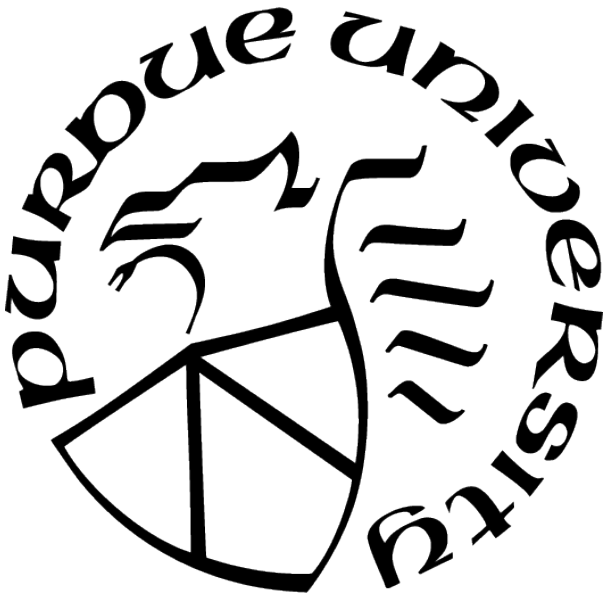

School of Aeronautics and Astronautics

West Lafayette, Indiana

August 2021

THE PURDUE UNIVERSITY GRADUATE SCHOOL
STATEMENT OF COMMITTEE APPROVAL

Dr. Jonathan Poggie, Co-Chair

School of Aeronautics and Astronautics

Dr. Gregory Blaisdell, Co-Chair

School of Aeronautics and Astronautics

Dr. Joseph Jewell

School of Aeronautics and Astronautics

Approved by:

Dr. Gregory Blaisdell

ACKNOWLEDGMENTS

I would like to thank Dr. Jonathan Poggie for his mentorship during this project. I entered this program as someone who had very little background in computational fluid dynamics and the use of high performance computing systems. In my education of these subjects he served as a great source of information which allowed me the unique opportunity to carry out computationally intensive simulations. I would also like to thank him for his sensibility and understanding in the unique situation that a pandemic and the stress of graduate school created. I would also like to thank Dr. Gregory Blaisdell for his mentorship during this program. For any question I had regarding turbulence, his responses would be thorough and accessible to a newcomer to the field. He is a gifted teacher and I would like to thank him for his time and patience. Additionally I would like to thank Dr. Joseph Jewell for being a member of my committee and providing feedback for the completion of this thesis. I would also like to thank Mohammadreza Kadivar and their co-authors for the permission to reuse multiple figures from a useful recent review article regarding turbulent rough wall-bounded flows.

The present work was funded by the Air Force Research Laboratory, under the Multidisciplinary Hypersonics Program. Computer hours were provided by the DoD HPCMP under a Frontier Project. This thesis has been approved for public release: distribution unlimited. Case number: AFRL-2021-2691.

TABLE OF CONTENTS

LIST OF TABLES

LIST OF FIGURES

LIST OF SYMBOLS

A_f	frontal projected area of roughness
A_w	wall-normal projected area
B	additive constant from the log-law
C_f	skin friction coefficient
$\overline{f}$	mean value of a quantity
f'	fluctuating value of a quantity using Reynolds decomposition
$\tilde{f}$	Favre average of a quantity
f''	fluctuating value of a quantity using Favre decomposition
f^+	quantity scaled in inner units
f_f	friction factor
k	roughness height
k_s	equivalent sand grain roughness (also denoted as ϵ
k_s^+	roughness Reynolds number
k_u	kurtosis of roughness
k/δ	blockage ratio
M	mach number
p	pressure
p_∞	freestream pressure
R	universal gas constant
R_q	root-mean-square of roughness
R_a	arithmetic mean deviation of roughness
R_v	maximum valley depth of roughness
R_p	maximum peak height of roughness
R_z	maximum peak to valley height of roughness
$R_{z(DIN)}$	Ten-point height of roughness based on DIN standard
$R_{z(ISO)}$	Ten-point height of roughness based on ISO standard
Re_D	Reynolds number using pipe diameter
R_{ij}	Reynolds stress tensor

s_k	skewness of roughness
T_w	wall temperature
T_∞	freestream temperature
u_i	velocity
u_∞	freestream velocity
$\overline{u}_D$	mean defect velocity
u_τ	friction velocity
δ	boundary layer thickness
δ_0	initial boundary layer thickness
Δu^+	roughness function
ϵ/d	relative roughness from Moody diagram
γ	ratio of specific heats
κ	von Karman constant
λ	solidity
ρ	density
ρ_w	density at the wall
ρ_∞	freestream density
τ_w	wall shear stress
μ	dynamic viscosity
ν	kinematic viscosity
Π_i	Buckingham Pi dimensionless parameter
Ψ	average roughness element spacing
Ξ	diagnostic function

ABBREVIATIONS

DNS	direct numerical simulation
ES	effective slope
ILES	implicit large-eddy simulation
PDF	probability density function
RANS	Reynolds Averaged Navier-Stokes Equations
TKE	turbulent kinetic energy
UTSI	University of Tennessee Space Institute

ABSTRACT

This study investigates the effects of near wall disturbances in the form of roughness on a compressible turbulent boundary layer. The studies were carried out using numerical methods which directly solve the Navier-Stokes equations. This provides for unique opportunities to investigate three dimensional structures of the flow as well as avoid the loss of physical fidelity with turbulence modeling. Three cases were ran, a smooth wall case, and two rough wall cases with different heights of the roughness elements between the cases. The results are first visualized with different approaches. Then statistical methods were used to characterize the flow.

The idea of wall-similarity is common in rough wall studies. This theory assumes that at high enough Reynolds numbers, the difference of length scales between those relevant to the near-wall flow and those relevant to the outer layer are separated enough that the effect of roughness is localized to a region of the boundary layer known as the roughness sublayer. Some studies have suggested that the disruption of commonly seen coherent streaks of low and high-speed fluid near the wall will disrupt ejections and sweeping events, affecting the outer layer of the boundary layer. This study found that the presence of the roughness elements seemed to make the near wall streaks less visible when plotting planes that cut through roughness elements, but did not disrupt the presence of the vortices associated with the streaks. The presence of the streaks was also found to be better observed when plotting a plane of constant wall-normal distance. This is consistent with the statistical findings that wall-similarity is generally observed. One exception is a shift in the Reynolds stress profiles in the outer region of the rough wall cases from the smooth wall case. This may suggest that there is a need in compressible flow studies for another scaling parameter involving the roughness geometry. These findings are consistent with recent compressible flow rough wall studies.

1. INTRODUCTION

The study of roughness effects in turbulent flows dates back to the 1850's when Hagen [1] and Darcy [2] set out to investigate pressure losses in water conduits. The rough surfaces of the conduits outlined some issues in laminar flow theory and went on to encourage further development in turbulence theory [3]. Eighty years later, Nikuradse [4] began studying wall roughness effects on turbulent flow by using pipes coated in sand. His work developed some of earliest methods in predicting rough-wall flows. The work was further developed by Colebrook [5] and later by Moody [6] who developed the Moody diagram, a tool commonly used for engineering practices in predicting drag.

Studying roughness has many practical applications. Smooth surfaces have a viscous sublayer very close to the surface, where viscous forces are important. Roughness can lead to increased flow instability near the surface and cause turbulent fluctuations to disrupt the viscous sublayer [7]. This can cause changes in the transfer of heat and momentum through a boundary layer. For vehicles with rough surfaces, this can consequently affect performance.

Roughness is seen on surfaces from a wide variety of application. It can be a result of the manufacturing processes used on the surface [7], or a result of mechanisms. These mechanisms include erosion, corrosion, and deposition [7]. In marine vehicles and machinery, biofouling such as barnacles can be considered roughness. In aircraft, ice accretion is an example of a deposition, as are insects that are unfortunate enough to become a feature of the surface. In turbines, pitting of the blades can become an issue and be considered a rough surface as well. The breadth of roughness types and the variety of applications where roughness is significant has led to a multitude of studies involving roughness.

Part of the difficulty in studying roughness comes from the difference in roughness characteristics. As in much of turbulence research, there are attempts to find common themes or patterns among the effects a range of roughness types can have. Townsend's [8] Reynolds number similarity hypothesis (and its extension from Perry and Chong [9] and Raupach et al. [10]), also known as wall similarity, is an attempt to find similarity between rough surfaces and smooth surfaces. The hypothesis states that at sufficiently high Reynolds number, the turbulent structure of the boundary layer outside of an area close to the wall known

as the roughness sublayer is unchanged. The only role the roughness has is in its effects in modifying the scaling friction velocity (u_τ) and the outer length scale (δ). The scaling friction velocity is a function of the coefficient of friction of the surface which can be affected by roughness.

Moody [6] sought to describe the frictional coefficient of various types of rough surfaces with one parameter, the equivalent sand grain roughness (k_s). The parameter comes from a series of studies using uniform sand of various sizes. The equivalent sand grain roughness is defined by a hydrodynamic test over a rough surface where the flow is considered in the fully rough regime (defined in section 1.3.1). The skin friction can be matched to an equivalent sand grain roughness. This can be problematic because knowing the sand grain roughness cannot be accomplished without a hydrodynamic test of the surface.

The irregularity of turbulence, and the uniqueness of many rough surfaces offers a challenge to finding overarching relationships which can reduce the complexity of problems. As applications for high speed vehicles have increased, an additional level of complexity is added. Many studies into roughness over the past century have been in water channels and in incompressible flows. As vehicles approach and exceed the speed of sound of a fluid, compressibility becomes relevant. There are open questions as to how these high speed environments subject to compressibility effects will be affected by roughness. This study aims to investigate with numerical methods how roughness can affect a compressible turbulent boundary layer.

The structure of this thesis is as follows. In the first chapter, background information relevant to turbulent boundary layers and roughness will be discussed. The second chapter will present the process used to set up and execute the computations. The following chapter will present results, first in the form of visualizing the flow, then in the form of statistics. Finally, conclusions and future work will be discussed.

1.1 Reynolds Averaged Navier-Stokes Equations

It will be useful to begin with a brief description of the Reynolds-Averaged Navier-Stokes equations (RANS). Though this study is concerned with compressible flows, the concepts associated with incompressible studies are still useful and will be discussed.

Laminar and turbulent flows are bounded by the dynamical equations for a fluid. The dynamical equations are derived to enforce conservation of mass, momentum, and in the case of compressible flows, energy as well. This study focuses on compressible flow, but for simplicity, we illustrate here the RANS approach for incompressible flow. For incompressible flow, the equations are

$$\frac{\partial u_{\mathrm{i}}}{\partial t} + u_{\mathrm{j}} u_{\mathrm{i,j}} = -\frac{1}{\rho} p_{,\mathrm{i}} + \nu u_{\mathrm{i,jj}} \tag{1.1}$$

$$u_{\mathrm{i,i}} = 0 \tag{1.2}$$

where u is the velocity, ρ is density, p is pressure, and ν is kinematic viscosity. Cartesian tensor index notation is used as well as the Einstein summation convention. A subscript with a comma denotes a derivative of that quantity. For example, $u_{\mathrm{i,i}}$ could also be written as $\frac{\partial u_{\mathrm{i}}}{\partial x_{\mathrm{i}}}$. Equation 1.1 represents Newton's second law for a continuum in a Eulerian reference frame. It represents a total of three equations which relate the rate of change of momentum per unit mass to the forces applied in the continuum. Equation 1.2 is the incompressible conservation of mass equation. These equations are referred to as the Navier-Stokes equations.

The Navier-Stokes equations are a set of nonlinear partial differential equations and can be difficult to solve analytically (if not impossible) without the aid of simplifying conditions. The equations often lead to chaotic structures in flow referred to as turbulence which can have very different time dependent spatial values from one instant to another. In engineering applications, the values of most interest are typically (though not necessarily) the mean statistics of the flow. It is possible to reduce the Navier-Stokes equations into functions of mean values.

The Reynolds decomposition is an important method used to derive the mean flow RANS equations. In the Reynolds decomposition the instantaneous value of some variable can be split into its mean (denoted with an overline) and fluctuating (denoted with a prime symbol) component. For velocity this can be written as

$$u = \overline{u} + u' \tag{1.3}$$

where u is the instantaneous value, $\overline{u}$ is the mean value, and u' is the fluctuation from the mean value. The mean can also be used as an operator. Taking the mean of both sides results in $\overline{u} = \overline{u} + \overline{u'}$ which can be simplified to $\overline{u'} = 0$. The average of the fluctuations is equal to zero.

Beginning with the conservation of mass (equation 1.2), if the mean is taken of $u_{\mathrm{i,i}} = 0$, the result is $\overline{u}_{\mathrm{i,i}} = 0$. Taking note of this equation, and expanding using the Reynolds decomposition results in $\overline{\overline{u}_{\mathrm{i,i}} + u'_{\mathrm{i,i}}} = 0$. Noting that $\overline{u}_{\mathrm{i,i}} = 0$, this can be simplified to $\overline{u'}_{\mathrm{i,i}} = 0$. The fluctuation of the divergence of velocity in incompressible flow is also zero.

Looking at 1.1, we can start deriving the RANS momentum equation by taking the average of each term. This results in

$$\frac{\partial \overline{u}_{\mathrm{i}}}{\partial t} + \overline{u_{\mathrm{j}} u_{\mathrm{i,j}}} = -\frac{1}{\rho}\overline{p}_{,\mathrm{i}} + \nu \overline{u}_{\mathrm{i,jj}}. \tag{1.4}$$

Looking closer at the convective term on the left of equation 1.1, since $u_{\mathrm{j,j}} = 0$, then $u_{\mathrm{j}} u_{\mathrm{i,j}}$ can be turned into $(u_{\mathrm{i}} u_{\mathrm{j}})_{,\mathrm{j}}$ since u_{j} is independent of the j derivative in incompressible flow. Using the Reynolds decomposition to expand this term, the result is $[(\overline{u}_{\mathrm{i}} + u'_{\mathrm{i}})(\overline{u}_{\mathrm{j}} + u'_{\mathrm{j}})]_{,\mathrm{j}} = [\overline{u}_{\mathrm{i}}\overline{u}_{\mathrm{j}} + \overline{u}_{\mathrm{i}} u'_{\mathrm{j}} + u'_{\mathrm{i}}\overline{u}_{\mathrm{j}} + u'_{\mathrm{i}} u'_{\mathrm{j}}]_{,\mathrm{j}}$. Taking the average of both sides causes terms which have both a mean and a fluctuating component to cancel, since the mean of the fluctuations is zero. This reduces to $\overline{u_{\mathrm{j}} u_{\mathrm{i,j}}} = \overline{u}_{\mathrm{j}}\overline{u}_{\mathrm{i,j}} + \overline{(u'_{\mathrm{i}} u'_{\mathrm{j}})}_{,\mathrm{j}}$. Returning to 1.4 and replacing the second term with the relationship just derived leads to the RANS momentum equation (1.5)

$$\frac{\partial \overline{u}_{\mathrm{i}}}{\partial t} + \overline{u}_{\mathrm{j}}\overline{u}_{\mathrm{i,j}} = -\frac{1}{\rho}\overline{p}_{,\mathrm{i}} + (\nu \overline{u}_{\mathrm{i,j}} - \overline{u'_{\mathrm{i}} u'_{\mathrm{j}}})_{,\mathrm{j}}. \tag{1.5}$$

This equation is similar to the unaveraged momentum equation except for an additional term similar in form to a stress, $\overline{u_i' u_j'}$. This term is referred to as the Reynolds stress and is important to studies of turbulence. It represents turbulent transport of momentum. This term leads to a closure issue when trying to solve the Reynolds averaged equations. Different methods are used in turbulence models to close the system of equations, but those methods will not be discussed here.

This study is concerned with compressible turbulent flows, for which the methods we used to derive the RANS equations are not valid since density is variable in compressible flows. Favre or mass-weighted averaging is another method used to derive mean flow equations. However, some statistics taken of compressible flows of values typical to incompressible flows, such as Reynolds stresses, can be rescaled in certain ways which map the compressible behaviors onto the incompressible behaviors. This will be further discussed in section 3.2.1.

1.2 The Flat-Wall Boundary Layer

The boundary layer is formed as a result of the no-slip condition, where the instantaneous and mean velocity of a fluid moving relative to a surface is zero. The flows where the fluid is subject to this boundary condition can be called wall-bounded. Many theoretical studies of boundary layers are derived from surfaces which can be considered ideal smooth surfaces. If a surface departs from being ideally smooth with disturbances in the near wall region, the boundary layer can show deviations from the classic flat-wall boundary layer structure. As a baseline, it will be useful to discuss the classical structure of a flat-wall boundary layer.

In turbulent boundary layers, the mean velocity as a function of wall-normal distance is often of interest. The study of the mean velocity profiles ends up helping define different regions of the turbulent boundary layer. The section that follows will first describe analytical approaches to defining regions of a turbulent boundary layer. Then a description of the structures seen in turbulent boundary layers will follow.

1.2.1 The Regions of a Turbulent Boundary Layer

The coordinate system which will be used in this study is defined as: $x_1 = x =$ streamwise, $x_2 = y =$ wall-normal, $x_3 = z =$ spanwise. The components of velocity are defined as u, v, and w for streamwise, wall-normal, and spanwise respectively. The freestream velocity, u_∞, is defined completely in the x-direction. The edge of the boundary layer will be defined as the y coordinate where $\overline{u(x,y)} = 0.99(u_\infty)$ unless otherwise specified. This study is concerned with compressible flow, however, it will still useful to begin with incompressible concepts and derivations such as the derivation of the RANS equations in the previous section.

Often in fluid experiments, there may be statistics of interest which can vary with a number of different parameters. Performing experiments for each possible independent variable can be costly and time consuming. Full-scale experiments may also be impossible, and in that case tests on models are the only option. Dimensional analysis alleviates some of the demand on the number and scale of the experiments required to obtain relationships between variables. The variables which may seem important to the dependent quantity of interest are identified, and nondimensional groups of parameters are created. The Buckingham Pi theorem is used to create the nondimensional groups and relate a function of nondimensional parameters to another function of a group of nondimensional parameters (see Anderson's *Fundamentals of Aerodynamics* [11]). We will begin our look into the structure of a boundary layer with dimensional analysis.

The parameters which may be significant to a flowfield vary according to the wall-distance. In the region near the wall, aptly called the wall-region, the parameters which are assumed to be significant to the flow are the kinematic viscosity (ν) $[L^2/T]$, the density (ρ) $[M/L^3]$, the wall shear stress ($\tau_w = \mu\frac{\mathrm{d}U}{\mathrm{d}y}$) $[M/LT^2]$, the mean velocity ($\overline{u}(y)$) $[L/T]$, and the distance from the wall (y) $[L]$. The dimensions of the quantities are listed in brackets where M is a unit of mass, L is a unit of length, and T is unit of time. Density and viscosity are assumed to be constants. There are five dimensional parameters and three primary dimensions. Using the Buckingham Pi theorem the difference between the number of dimensional parameters and the number of primary dimensions yields the number of possible dimensionless parameters. The groups of dimensionless parameters are

$$\Pi_1 = \frac{y}{\nu}\left(\frac{\tau_w}{\rho}\right)^{\frac{1}{2}} = y^+ \tag{1.6}$$

$$\Pi_2 = \overline{u}\left(\frac{\tau_w}{\rho}\right)^{-\frac{1}{2}} = u^+. \tag{1.7}$$

The value of $\left(\frac{\tau_w}{\rho}\right)^{\frac{1}{2}}$ is referred to as the friction velocity (u_τ) and is used as a scaling velocity. The value of ν/u_τ is the length scale for the inner wall region. Quantities which are nondimensionalized using these parameters are denoted with a $^+$ superscript. These variables are also described as being in *inner units*.

The Buckingham Pi theorem allows us to set one nondimensional group as a function of other nondimensional groups. Since there are only two nondimensional groups, this can be written as

$$u^+ = f(y^+). \tag{1.8}$$

Equation 1.8 is referred to as the "law of the wall". It represents a function which defines the shape of the velocity profile of a boundary layer in inner units. The shape of the function is often described by experiments, but the shape of the velocity distribution in some regions of the boundary layer can be derived analytically.

A Taylor series expansion of the $\overline{u}$ velocity can be written as

$$\overline{u} = C_1 y + O(y^2) + O(y^3) + ... \tag{1.9}$$

In the region very near the wall, the higher order terms become very small and can be omitted. This leaves $\overline{u} = C_1 y$. The constant C_1 is related to the wall shear stress since on an ideally smooth wall the shear stress on the surface is

$$\tau_w = \rho\nu\frac{\partial u}{\partial y}. \tag{1.10}$$

Equation 1.10 is also the equation for the shear stress of a laminar flow. Even in turbulent flow there is assumed to a very small laminar flow region near the surface where turbulent

velocity fluctuations are negligible. Taking the derivative of 1.9 and omitting higher order terms results in $\frac{\partial \overline{u}}{\partial y} = C_1$. From equation 1.10, the value of $C_1 = \frac{\tau_w}{\rho\nu}$, leaving the equation for the very near wall region to be $\overline{u} = \frac{\tau_w}{\rho\nu} y$, or written in inner units

$$u^+ = y^+. \tag{1.11}$$

Equation 1.11 is the expected function bounding the shape of the inner-scaled velocity profile very near the wall. The region is a small layer of viscous laminar fluid, present due to the negligible turbulent velocity fluctuations near the wall. It is referred to as the viscous sublayer, or sometimes the laminar sublayer.

So far the discussions have mostly comprised the velocity distribution of the region of the boundary layer where the wall's presence is a dominant factor. The outer region of the boundary layer is less impacted by the presence of the wall and will need to be investigated using dimensional analysis as well. The outer region of the boundary layer acts like a wake of the boundary layer further upstream, and it is useful to work in terms of the defect velocity ($\overline{u}_D = u_\infty - \overline{u}$). As the wall-normal distance is increased, viscosity's effects compared to convection are very small, and viscosity is not expected to be a relevant scaling parameter (with the exception perhaps of the viscous superlayer where irrotational freestream fluid meets rotational fluid from the boundary layer). In the outer region, the relevant scaling parameters are assumed to be the distance from the wall (y) [L], density (ρ) [M/L^3], the wall shear stress (τ_w) [M/LT^2], the boundary layer thickness (δ) [L], and the defect velocity ($\overline{u}_D$). There are five parameters and three fundamental dimensions so there are two dimensionless groups. These groups are

$$\Pi_1 = \frac{\overline{u}_D}{u_\tau} = {\overline{u}_D}^+ \tag{1.12}$$

$$\Pi_2 = \frac{y}{\delta}. \tag{1.13}$$

Setting Π_2 as a function of Π_1 results in

$$\overline{u}_D{}^+ = g\left(\frac{y}{\delta}\right). \tag{1.14}$$

Though equation 1.14 does not give any specific shape of a function, it shows that the defect velocity in inner units will be a function of the wall-normal distance and the boundary layer thickness. Equation 1.14 will be useful in deriving the distribution of velocity in the next region of interest.

Equation 1.8 and equation 1.14 show the expected behaviors in the inner and outer region of a boundary layer. A continued analysis can be carried out with the assumption that there is a region where both laws could apply. If a functional analysis of the matching of the inner and outer forms is carried out, the result is a region referred to as the logarithmic overlap region. The equation for the logarithmic region is

$$u^+ = \frac{1}{\kappa} log(y^+) + B, \tag{1.15}$$

where κ is the von Karman constant (typically 0.41) and B is an additive constant (~ 5.2). The values of the constants can vary, but they are typically within 5% of the listed values [12]. Figure 1.1 shows the log law superimposed over a variety of Reynolds number in a fully developed turbulent channel flow. The data show a nice collapse onto the logarithmic region for $y^+ > 30$. It is worth noting that the derivation of the log law assumed a high Reynolds number, and the log law may not be valid for low Reynolds numbers and for developing flows.

At large y^+ values, experimental data tend to deviate from the log law as the outer layer dynamics have a larger effect on the flow. To account for the effect of the wake in the outer region of the turbulent boundary layer, Coles [14] suggested adding an extra term to the log law written as

$$u^+ = \frac{1}{\kappa} log(y^+) + B + \frac{\Pi(x)}{\kappa} w\left(\frac{y}{\delta}\right). \tag{1.16}$$

The function $w\left(y/\delta\right)$ is referred to as the law of the wake. This term represents how the outer region will affect the distribution of the mean velocity with increasing y location. The

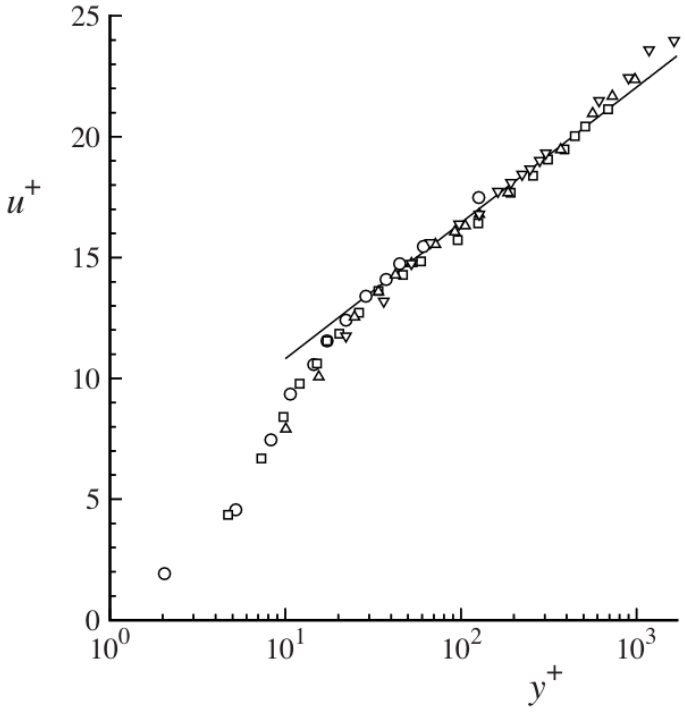

Figure 1.1. Mean velocity profiles in fully developed turbulent channel flow measured by Wei and Willmarth [13]:circles, $Re_0 = 2,970$; squares, $Re_0 = 14,914$; point up triangle, $Re_0 = 22,776$; point down triangle, $Re_0 = 39,582$; line, the log law 1.15. Figure and caption from Pope's *Turbulent Flows* [12]. Reproduced with permission of the Licensor through PLSclear. Copyright of Cambridge University Press.

shape of the wake function is assumed to be universal [12]. It is normalized so that $w(0) = 0$ and $w(1) = 2$. The parameter Π is called the wake strength parameter and its value depends on the flow conditions. Coles [14] determined the wake function using experimental data and expressed the function as

$$w\left(\frac{y}{\delta}\right) = 2\sin^2\left(\frac{\pi}{2}\frac{y}{\delta}\right). \tag{1.17}$$

The wake function is typically negligible below $y/\delta = 0.15$ [3]. According to Jiménez [3], in zero-pressure-gradient boundary layers, Π is at most of order unity. From analyzing the order of magnitude of terms, Jiménez proposes that in the logarithmic region 70% to 80% of the velocity difference occurs across the boundary layer. The logarithmic region is also responsible for over half of the overall production of turbulent energy [3]. There have been further developments to equation 1.17, and many equations fit a universal profile very nicely such as Spalding's [15] law-of-the-wall and Reichardt's law [16].

The discussion of the boundary layer so far involved the distribution of the mean velocity profile. From this discussion we have identified a few regions of interest to the boundary layer including the linear sublayer, the logarithmic region, and the outer region. There are several regions of the boundary layer, mostly classified by properties of the mean velocity or the mechanisms which dominate the transfer of momentum. A summary of the regions are seen in Table 1.1. The Reynolds number and flow conditions can affect the exact locations of these regions, but generally the locations in Table 1.1 can be used as a guideline.

From the analysis of this section and some empirical evidence, we are left with a general description of the regions of flow. This will be useful in our further investigations into boundary layers, especially those boundary layers with disturbances near the wall.

1.2.2 Structures in a Turbulent Boundary Layer

In the study of turbulence there is a constant effort to see patterns in the flow. Any observed consistency or pattern allows some order to be brought to the fundamental chaos of turbulence. Identifying structures in a flow field can give information regarding dominant mechanisms of momentum and energy transfer and be of practical engineering use in efforts to

Table 1.1. Descriptions of regions in a turbulent boundary layer. Table and descriptions from Pope's *Turbulent Flows* [12] with some adjustments. Reproduced with permission of the Licensor through PLSclear. Copyright of Cambridge University Press.

Region	Location	Defining property
Viscous Sublayer/Linear Sublayer	$y^+ < 5$	The Reynolds shear stress is negligible compared with the viscous stress
Buffer Layer	$5 < y^+ < 30$	The region between the viscous sublayer and the log-law region
Log-law Region	$y^+ > 30, y/\delta < 0.3$	The log-law applies
Viscous Wall Region	$y^+ < 50$	The viscous contribution to the shear stress is significant
Inner Layer	$y/\delta < 0.1, y^+ < 1000$	$\overline{u}$ is determined by u_τ and y^+ and is independent of u_∞ and δ
Overlap Region	$y^+ > 50, y/\delta < 0.1$	Region of overlap between inner and outer layer (present for large Reynolds numbers)
Outer Layer	$y^+ > 50$	Direct effect of viscosity on $\overline{u}$ is negligible

manipulate the flowfield. Turbulent structures or quasi-coherent structures can be defined as regions of space and time in the flowfield where there is a characteristic or coherent pattern. These are best identified using visualization techniques, conditional sampling techniques, or by eduction methods [12].

Pope's *Turbulent Flows* textbook [12] provides a good summary of turbulent structures, and that information will be reviewed here as well.

There are different types of coherent structures observed within boundary layers. In addition to Pope [12], Kline and Robinson [17] and Robinson [18] provide a useful list of observed behaviors. The most commonly observed and documented structures are as follows: low-speed streaks in the region $y^+ < 10$, ejections of low-speed fluid outward from the wall, sweeps of high-speed fluid toward the wall, vortical structures of different forms, strong

internal shear layers in the wall region ($y^+ < 80$), near wall pockets, backs (surfaces where the streamwise velocity changes abruptly), and large scale motions in the outer layers [12].

The streaks observed in the near-wall region are of particular interest to this study, since disturbances near the wall can impact these streaks. The streaks are representative of slow-moving fluid with high-speed fluid between them. These streaks are visualized in Figure 1.2 with a gray-scale contour of streamwise velocity as Mach number relative to the fixed freestream sound speed. They have been found to be related to a phenomena known as bursting. As the streaks move downstream, they begin to move away from the wall. Around $y^+ = 10$ the streaks rise more rapidly away from the wall and cause ejections of lower speed fluid into the outer layer of the boundary layer. The ejections are associated with breakdown into fine-scale turbulence. In the absence of strong compressibility effects, conservation of mass would expect that movements away from the wall would not occur without movements towards the wall. Movements of high-speed fluid towards the wall are called sweeps and are also a frequently seen behavior in boundary layers.

In the near-wall region ($y^+ < 100$) the dominant structures seen are pairs of counter-rotating vortices. These vortices are associated with the near wall streaks and can lead to the lifting motion which is eventually seen as the bursting in the outer layer.

Hairpin vortices are a common structure commonly seen in laminar to turbulent transition. Head and Bandyopadhyay [20] conjectured that larger structures in the boundary layer could be composed of many hairpin vortices. Perry et al. found that this explanation could explain the behavior of statistics in boundary layers [9] [21] [22].

Observations of coherent structures in turbulence is often a subjective effort. There are other eduction techniques such as proper orthogonal decomposition which aims to mathematically describe some coherent structures. These methods will not be reviewed here.

1.3 Roughness

Thus far the discussion has been in regards to surfaces which are ideally smooth. These smooth surfaces are seen in practice at times and are a useful canonical reference case for research. In engineering practice, surfaces are often subject to different processes which can

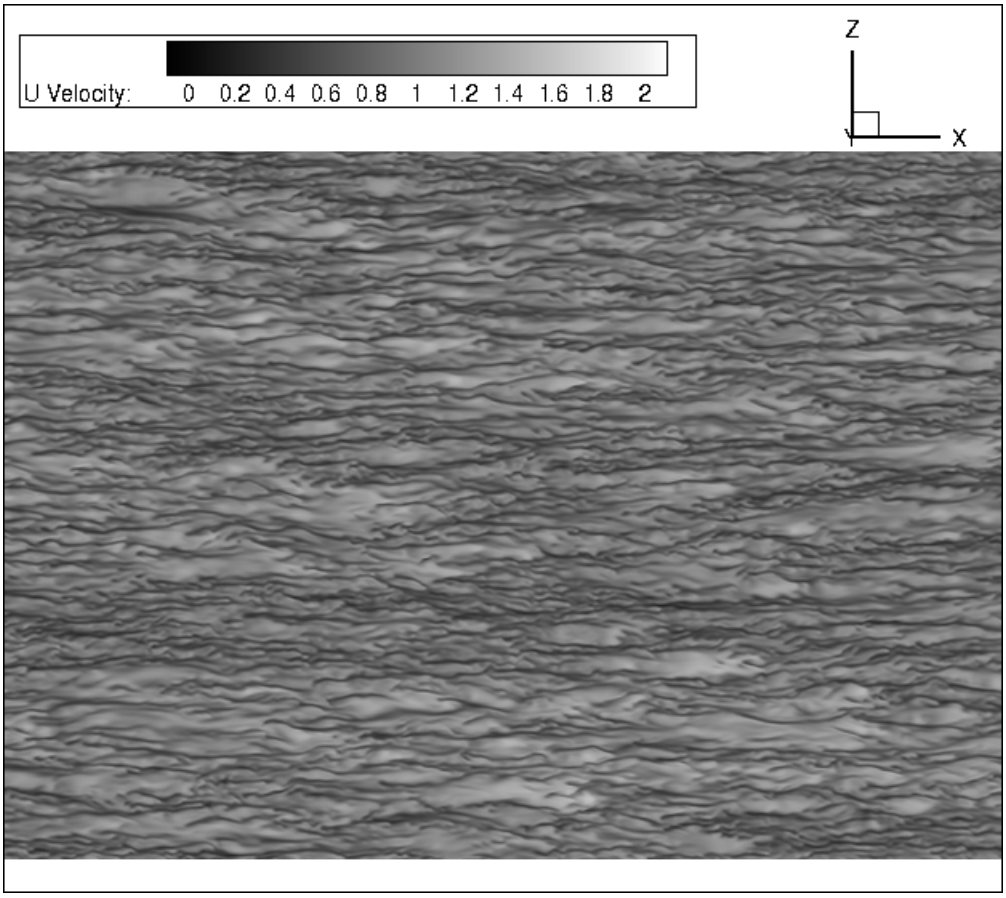

Figure 1.2. Contour of instantaneous u velocity (as Mach number relative to freestream sound speed) at $y^+ = 18$ from a numerical study by Gaskins et. al [19], $Re_{\theta i} = 15,000$.

affect the quality of the surface. Wear and tear can affect a surface's quality as well as processes such as erosion or corrosion. Even in the atmosphere, the features on land such as trees or buildings can be considered roughness in the atmospheric boundary layer. There are many instances where boundary layers form over rough surfaces. Of practical interest is the effect roughness can have on the friction coefficient of a surface. Friction can affect performance of systems as energy is lost to heat. In high-speed flight applications, the impact of roughness on heat transfer is of strong interest as well.

In the following section, the different ways of characterizing a rough surface and the impacts roughness has on turbulent boundary layers will be discussed. Following these discussions, methods of predicting engineering quantities of interest will be discussed.

1.3.1 Roughness Effects on a Turbulent Boundary Layer

The review of turbulent boundary layers in the prior sections has built a foundation for understanding the effect near wall disturbances can have on a turbulent boundary layer.

The inner law of smooth wall boundary layers was derived assuming there were no characteristic length scales of the surface that were relevant to the flow besides the distance from the wall y. For rough surfaces, a scaling variable which can classify the contribution of roughness to the boundary layer is needed. Nikuradse [4] performed some of the earliest studies regarding rough-wall turbulent flows with pipes coated in uniform sand. Following Nikuradse's work, work by Colebrook [5] and Moody [6] further developed the understanding of roughness effects. A consequence of the early tests involving sand is that the parameter which has been commonly used for scaling is referred to as the equivalent sand grain roughness height (k_s). If the roughness is similar to the sand used by Nikuradse in shape and distribution, then k_s is equivalently just the height of the roughness elements (k). Variations in the surface elements in shape, sizing, distribution etcwill cause k_s to deviate from k. In these cases the value of k_s is the value of the uniform sand grain roughness height from Nikuradse's experiments that will match the friction of the irregular rough surface in the fully rough regime (defined shortly). There is difficulty in determining k_s because it can only be determined by hydrodynamic tests. There are attempts to correlate geometric parameters of the roughness topology with k_s so that hydrodynamic tests are not needed, but that is ongoing work.

In smooth wall boundary layers there is a region very close to the wall ($y^+ < 5$) where viscosity dominates the transfer of momentum. As discussed in a previous section, this layer is referred to as the viscous sublayer. The viscous sublayer is a laminar layer of fluid where the Reynolds stress is negligible compared to the viscous stress. Disturbances near the wall can act to increase flow instability in this laminar flow and introduce turbulence disruptions [7]. The severity of the disruptions classifies different rough-wall flow regimes.

An illustration of the different regimes of flow can be seen in Figure 1.3. For roughness that is minimally disruptive to the viscous sublayer, the flow can be classified as hydraulically smooth. Here the wall shear stress is purely a function the Reynolds number Re_D, where D

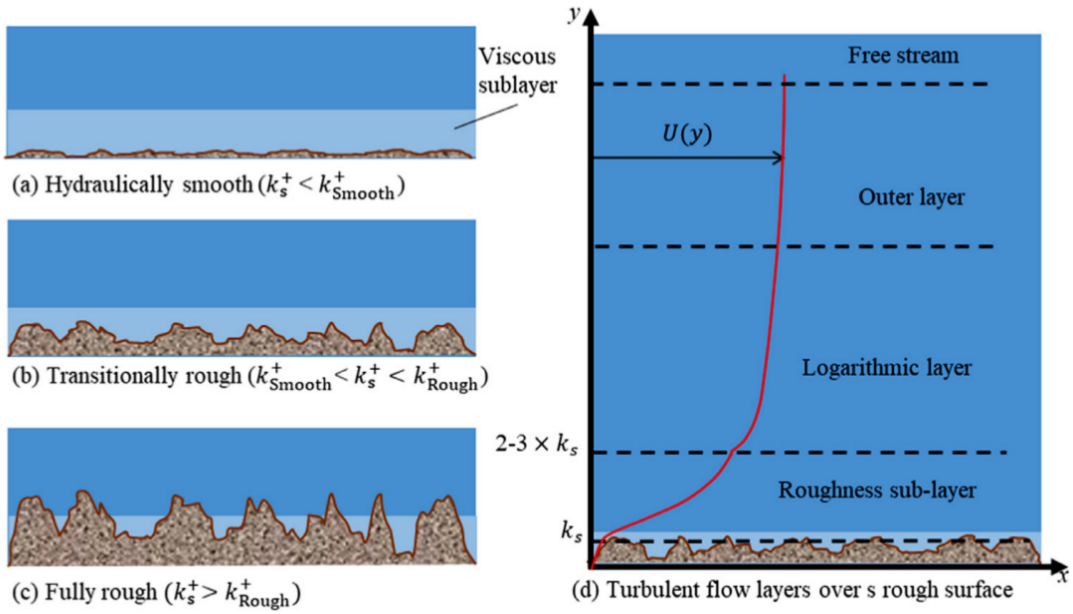

Figure 1.3. The types of flow regimes for turbulent flows over rough surfaces; (a) the hydraulically smooth regime where the roughness is not a significant portion of the viscous sublayer, (b) the transitionally rough regime where the viscous sublayer is partially disrupted, (c) the fully rough regime where the viscous sublayer is no longer present, (d) illustration of the different regions of a turbulent rough-wall boundary layer. Figure and caption courtesy of Kadivar et al. [7] with permission from the author and publisher.

is the pipe diameter (from the early roughness studies involving pipes coated in sand). In the transitionally rough regime, the wall shear stress is a function of viscous and form drag on the roughness elements (becoming an effective shear stress). In the fully rough regime, the viscous sublayer is lost, and the effective shear stress on the surface is purely a function of the form drag of the roughness elements. Terminology here can be conflicting at times, as these descriptions are dependent on the flow conditions and geometry of the roughness elements. In the next subsection, surfaces will be described as rough purely on geometric parameters. From Nikuradse's experiments[4], surfaces are considered hydraulically smooth if $k_s^+ < 5$, transitionally rough for $5 < k_s^+ < 70$, and fully rough for $k_s^+ > 70$. The layer which is directly influenced by the length scale associated with the roughness typically extends to $3k_s$ to $5k_s$ [23]. This region is known as the roughness sublayer.

Investigations into the mean velocity profile of rough flows led Clauser [24] and Hama [25] to define the roughness function (Δu^+). When the mean velocity profile is plotted in inner coordinates, it was found that the log law region had a downward shift as seen in Figure 1.4. The shape of the mean velocity profile in the outer layer appeared to be unaffected by roughness. The roughness function can be incorporated into the log law with an extra term

$$u^+ = \frac{1}{\kappa} log(y^+) + B - \Delta u^+. \tag{1.18}$$

The roughness function allows comparisons of rough surfaces with differing geometries [26].

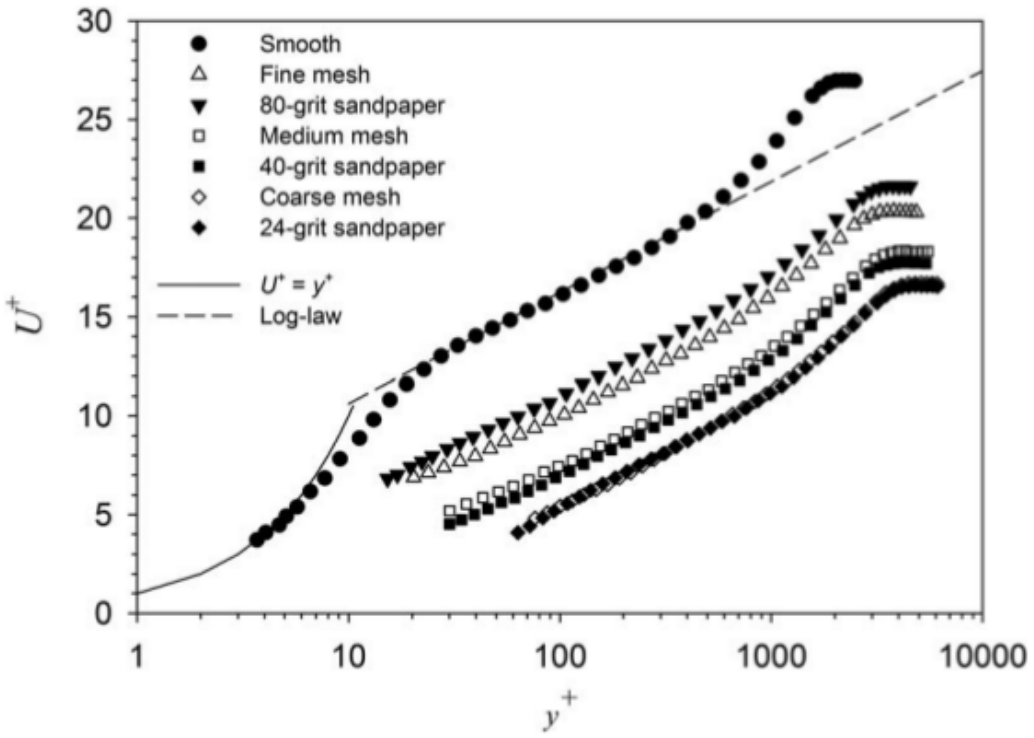

Figure 1.4. Roughness function for mesh and sandgrain roughness. Reprinted from Karen A. Flack and Michael P. Schultz , "Roughness effects on wall-bounded turbulent flows", Physics of Fluids 26, 101305 (2014), with the permission of AIP Publishing. [27]

Some questions regarding roughness are in regards to if the interactions near the wall can have a cascading nonlinear effect and affect large scale structures of the flow. Townsend

[8] offered the Reynolds number similarity hypothesis to try and answer this question. Flack and Schultz [26] summarize the hypothesis as "at sufficiently high Reynolds number, the turbulent motions outside the roughness sublayer are independent of the wall boundary condition except in the role it plays in modifying the outer velocity (u_τ) and the length scales (δ)." The assumption associated with the hypothesis is that there is a significant separation of scales between the boundary layer thickness (δ) and the roughness height (k). To investigate the idea of wall similarity, it is useful to plot velocity profiles as defect velocity profiles. Wall similarity would lead to collapse of various defect velocity profiles. Figure 1.5 shows a collapse of the defect velocity for various roughness types. Flack and Schultz [26] have found wall similarity is valid for many roughness types.

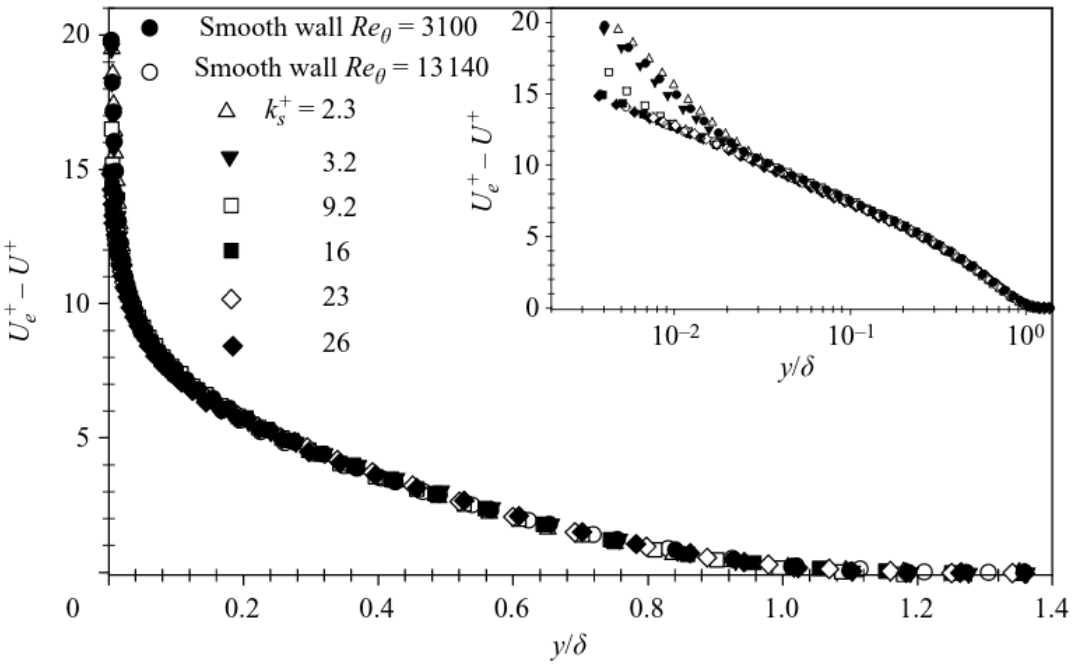

Figure 1.5. Mean velocity profiles as defect velocities for smooth walls and rough walls of various inner-scaled equivalent sandgrain roughness. Reprinted with permission for use in Master's Thesis from M. Schultz and K. Flack, "The rough-wall turbulent boundary layer from the hydraulically smooth to the fully rough regime,"J.Fluid Mech. 580, 381-405(2007). [28]

Jiménez has proposed that roughness elements effects could vary according to the friction Reynolds number k_s^+ and the blockage ratio k/δ (defined by Jiménez as δ/k but for the sake

of clarity is inverted here). The value of k_s^+ measures the effect the roughness has on the buffer layer. In the buffer layer there is a nonlinear self-sustaining cycle which is responsible for generating a majority of the turbulent energy [29]. This region is home to the streaks of high and low speed fluid which have been found to be a part of the development of large scale structures in the flow. The blockage ratio will determine if a logarithmic region survives. For flows with large roughness elements compared to the boundary layer thickness, much of the dynamics of the boundary layer is changed and the flow behavior is dependent on the geometry of the surface. Jiménez classifies these flows as "flows around obstacles." The suggested value by Jiménez to expect similarity laws to hold is $k/\delta < 0.025$. Experimental results from Flack and Schultz have shown that wall similarity can still be found for some flows with large blockage ratios [26].

1.3.2 Geometric Descriptions of Rough Surfaces

The surface texture of a rough surface, also known as the surface finish or surface morphology is a set of geometrical irregularities which can be randomly or uniformly distributed over a surface [7]. Some of the difficulty in roughness studies is in the breadth of surface textures which can be considered rough. Roughness elements can vary not only in their height and shape, but also in their surface density. To quantify the description of a rough surface, there have been parameters proposed which depend solely on the geometric features of the surface. These parameters can be seen in Table 1.2.

It is worth mentioning that the parameters in Table 1.2 are purely geometric and independent of flow conditions. These quantities are of interest because dimensional analysis may require another parameter in rough wall-bounded flows which is related to the roughness geometry. They are also of interest because the length scale commonly associated with roughness k_s may be possible to determine based on geometric measures of the surface topology.

The first parameter in Table 1.2 is the effective slope. It is a parameter that was introduced by Napoli et. al [30] to attempt to differentiate between a rough and a wavy surface. If a rough surface can be thought of simplistically as a pattern of sinusoidal features, a rough

Table 1.2. Roughness parameters and their corresponding descriptions. Table adapted from Kadivar et al. [7] with permission from the author and publisher.

Parameter	Description	Equation
ES	Effective Slope	$ES = \frac{1}{l_x l_z} \int_0^{l_x} \int_0^{l_z} \left\lvert \frac{\partial k(x,z)}{\partial x} \right\rvert dxdz$
R_q	Root-mean-square roughness	$\sqrt{\frac{1}{l} \int y^2 dx}$
R_a	Arithmetic mean deviation	$\frac{1}{l} \int \lvert y \rvert dx$
R_v	Maximum valley depth below the mean line, within a single sampling length	$\lvert min(y(x)) \rvert$
R_p	Maximum peak height above the mean line, within a single sampling length	$max(y(x))$
R_z	Maximum peak to valley height of profile	$R_v + R_p$
$R_{z(DIN)}$	Ten-point height based on the definition in DIN standard, within a five sampling length	$\frac{1}{10} \left(\sum_{\mathrm{j}=1}^{5} R_{p,\mathrm{j}} + \sum_{\mathrm{j}=1}^{5} R_{v,\mathrm{j}} \right)$
$R_{z(ISO)}$	Ten-point height based on the definition in ISO standard, within a five sampling length	$\frac{1}{10} \left(\sum_{\mathrm{j}=1}^{5} R_{p,\mathrm{j}} - \sum_{\mathrm{j}=1}^{5} R_{v,\mathrm{j}} \right)$
s_k	skewness	$\frac{1}{(R_q)^3} \frac{1}{l} \int y^3 dx$
k_u	kurtosis	$\frac{1}{(R_q)^4} \frac{1}{l} \int y^4 dx$
λ	solidity	A_f / A_w

surface would be a surface with short wavelengths (high frequency of roughness elements) relative to the height of the roughness elements. Medium wavelength surfaces are considered wavy surfaces. In the function defining the effective slope, $k(x, z)$ is the roughness amplitude and l_x l_z are the sampling lengths in the x and z directions. The effective slope can be thought of as an average magnitude of the slope of the roughness elements. The threshold for a wavy surface is found to be $ES < 0.35$ [30] [31]. Wavy surfaces have roughness functions which do not scale with the roughness height [26].

Some of the parameters are based on information of the amplitude of the roughness along a sampling line l. These are known as R parameters [7]. The value of y in the equations is the roughness amplitude and must be centered at the mean value of the roughness height. An illustration of the R parameters can be seen in Figure 1.6. R_a represents an average deviation of the roughness height from the mean along a sampling line. R_q represents the standard deviation of the roughness heights and may be physically more significant than R_a [7]. R_z is a parameter which is sensitive to occasional high peaks or low valleys. Though R parameters can be useful in describing a rough surface, but they may not have sufficient information to characterize a surface because different surface textures can result in similar values of R parameters.

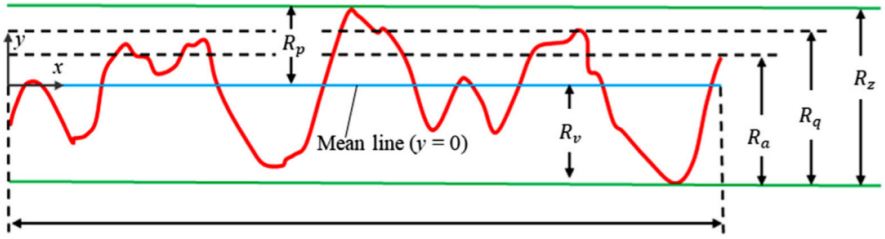

Figure 1.6. Illustration of the various R parameters. Figure courtesy of Kadivar et al. [7] with permission from the author and publisher.

Surface features of rough surfaces can be stochastic in nature, so it can be useful to describe the surface using information derived from a probability density function (PDF). This idea was first introduced by Musker [32]. The value of R_q can be derived from the PDF as well as the skewness(s_k) and kurtosis (k_u) of the PDF. The skewness is a measure of the PDF profile symmetry. A negative skewness would be indicative of more valleys on the surface. More valleys on the surface would be characteristic of processes removing material from the surface such as from erosion, corrosion, or pitting etc. A positive skewness would be indicative of more peaks which is characteristic of surface deposits [26]. The kurtosis is representative of the range of scales in the roughness heights and characterizes whether the PDF is flat or peaked. It is a strictly positive value. Figure 3.35 shows examples of different values of skewness and kurtosis and their associated PDF's. A Gaussian surface has values $s_k = 0$ and $k_u = 3$ [26]. These parameters together can describe the profile of rough

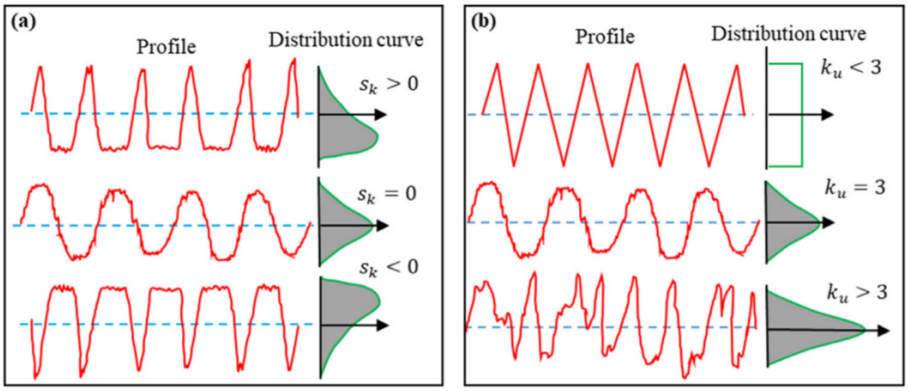

Figure 1.7. Skewness and kurtosis of different roughness types along with their associated pdf distribution curves. Figure courtesy of Kadivar et al. [7] with permission from the author and publisher.

surfaces well, but there is information missing regarding the surface density of the roughness elements. Also, for certain distributions, like power laws, moments such as skewness and kurtosis may not converge. According to Flack et al [26], predictive scales will likely need to be supplemented by a density parameter for sparse roughness. A commonly used parameter to describe the density on the surface is the solidity (λ). The solidity is defined as the ratio between the frontal projected area of the elements (A_f) to the unit projected wall-parallel area (A_w) [26]. This can also be calculated by the ratio of the average roughness element spacing (ψ) to the roughness height (k).

These parameters listed in Table 1.2 can aid in the description of a rough surface in an objective quantifiable way. A combination of these parameters may prove helpful in an effort to scale turbulent rough wall-bounded flows.

1.3.3 Prediction of Drag on a Rough Surface

In engineering applications pertaining to fluid flows, frictional losses are often a quantity of interest. In rough-wall flows, there are typically changes in the friction of the surface compared to the smooth wall cases. The Moody diagram [6], seen in Figure 1.8, is a predictive tool developed to help predict the friction factor (f_f) in a variety of Reynolds numbers and relative roughness ϵ/d. Figure 1.8 illustrates the various regimes of rough flow. Though the

diagram is a useful engineering tool, there are some shortcomings that Moody acknowledged. Moody expected the diagram to be accurate to within about 10% [26].

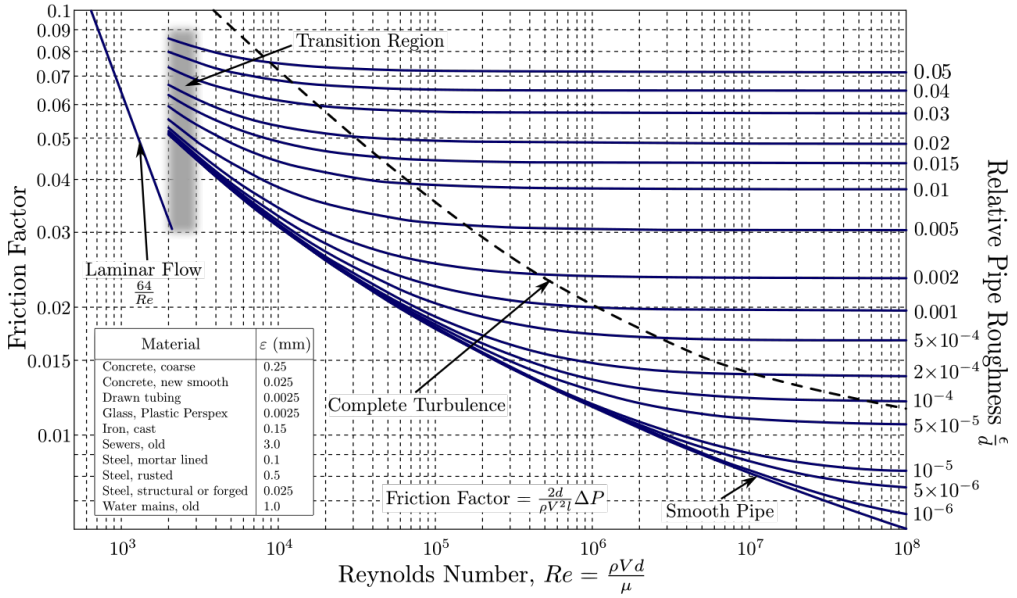

Figure 1.8. Moody diagram. The value of ϵ is equivalently k_s. Figure courtesy of S. Beck and R. Collins, University of Sheffield [33].

One of the shortcomings of the Moody diagram is the need to know what k_s is for a surface prior to predicting surface friction. The parameter k_s is not a physical measure of the surface but is the value of the uniform sand roughness height from Nikuradse's experiments that produce the same friction factor as the surface of interest in the fully rough regime [26]. A hydrodynamic test is required in the fully rough regime on the surface of interest to determine k_s. This can be troublesome if there is a need to predict friction without the possibility of a hydrodynamic test on a surface.

The value of k_s is still a useful parameter. Correlations between k_s^+ and the roughness function Δu^+ have been found. Using k_s^+ as a predictive tool for Δu^+ is possible, and it would be troublesome to abandon the use of k_s completely. What would be useful is a way to relate the geometric parameters outlined in section 1.3.2 to the value of k_s.

Flack and Schultz [26] offer an equation to relate the root mean square roughness height R_q and the skewness s_k to the equivalent sand grain roughness height k_s. The equation is

$$k_s = 4.43 R_q (1 + s_k)^{1.37}. \tag{1.19}$$

This equation has shown a fair correlation and is worth investigating for future studies. In addition to equation 1.19, Flack and Schultz [26] offer another equation representing the prediction of the skin friction coefficient C_f (defined as the ratio of the wall shear stress versus the dynamic stress of freestream) over a flat plate of length L. This equation is

$$\sqrt{\frac{2}{C_f}} = -2.186 \ln\left(\frac{k_s}{L}\right) + 0.495. \tag{1.20}$$

Equations 1.19 and 1.20 would allow the prediction of engineering quantities with only measurements of the surface texture. It is worth mentioning that an assumption used to find equation 1.20 is that the fully rough regime is achieved with $k_s^+ > 70$. New constants may be needed if the fully rough regime is achieved at a significantly different value of k_s^+ as some studies have shown that the fully rough regime can be achieved with values less than 70 [26].

It is worth noting that there are also roughness types called k-type and d-type where there are distinctions between the flow dynamics between the elements. However, these will not be discussed.

1.3.4 Recent Compressible Flow Findings

When it comes to rough-wall studies, there have been far fewer studies in compressible flow compared to incompressible flow. Most studies have dealt with the mean response of a turbulent boundary layer in the presence of roughness, and it was not until 2000 that the turbulent response of a compressible boundary layer to roughness was measured by Bowersox and Latin [34] [35]. Kocher et al. [36] provides a summary of key findings for recent compressible flow studies, which are discussed here.

Bowersox and Latin [34] [35] found that the roughness elements when in the fully rough regime can protrude into the supersonic region of the boundary layer. This causes shock waves and expansion fans around the roughness elements. This suggested that the behavior

of the flows may vary significantly from incompressible flows. They also found that the Reynolds stress profiles did not collapse when scaled by outer parameters. This indicates a possible dependency on the roughness elements' geometry.

A commonly studied roughness topology for compressible studies has been diamond roughness elements. This is due to the pattern of roughness observed from thermal protection systems. Ekoto et al. [37] [38] investigated the diamond roughness pattern and found that the Reynolds stresses and turbulent intensities increased at the forward portion of each diamond roughness element and decreased in the trailing portion. Studying the same roughness elements in a Mach 4.9 flow, Peltier et al. [39] found that the roughness elements increased turbulent fluctuations in the lower half of the boundary layer and decreased turbulent fluctuations in the upper half of the boundary layer. Peltier et al. also found that the Reynolds stresses and inner-scaled mean velocity profiles were lower in magnitude than the smooth wall case. The difference in the inner-scaled mean velocity profile is the roughness function (Δu^+) and is also seen in incompressible studies. Sahoo et al. [40] found a similar behavior of the Reynolds stresses and mean velocity profiles. Kocher et al. [36] found that the effects of roughness develop downstream with the boundary layer and that the velocity fluctuations continue to increase along the streamwise locations. The roughness function approached a converged value as the boundary layer developed downstream in the rough cases. Kocher et al. also found that the Reynolds stress values were higher in the rough cases than the smooth case.

These collective findings give a baseline of possible expectations for results in the present study.

1.4 Scope of Study

This study aims to investigate the effects of roughness on a compressible turbulent boundary layer. The roughness geometry considered is a sinusoidal plane similar to an egg carton. The in-house code WABASH is used to numerically simulate the flow and collect statistics via direct solution of the Navier-Stokes equations.

The flow will first be investigated visually for any effect on structures commonly seen in flow. Then standard statistics are calculated to describe the flow. Due to a wide variety of flow conditions and roughness types, often drawing conclusions in roughness studies involves the amalgamation of results from many studies. This study aims to contribute some data in the compressible regime of rough flows.

2. METHODOLOGY

This chapter outlines the process used to conduct the numerical simulations. First the selection of experimental conditions will be discussed. The subsequent sections will discuss the mesh generation, configuration of the simulation, and further details regarding the numerical tools used.

2.1 Experimental Background

It is useful to have experimental data to compare to the data generated by numerical simulations. This helps to validate the tool being used and can give insight into the physical phenomena happening in the experiment. For this study, the baseline case chosen is an experiment conducted by Kocher et al. [36] at the University of Tennessee Space Institute (UTSI) at the Mach 2 facility.

In the UTSI experiments, a low-enthalpy, blow-down Mach 2 wind tunnel was used. The stilling chamber upstream of the test section was maintained at approximately 210 kPa exhausted to atmospheric conditions. The average stagnation temperature was 285 K (unheated room temperature). The test section of the wind tunnel was square and measures 203 mm x 203 mm. The test section floor has a naturally occurring turbulent boundary layer with 11 mm thickness. The free-stream velocity was 507 m/s. These conditions resulted in a Mach number of 2.01 and a unit Reynolds number of $3 \times 10^7\ m^{-1}$.

Three interchangeable floor pieces were used in the test section to investigate the effect of roughness on the boundary layer. The floor pieces were inserted so that the crests of the roughness elements were flush with the floor. Three roughness topologies were used. The first floor insert was a hydraulically smooth acrylic piece. The second test article was a mesh of uniformly distributed diamond roughness elements. The diamond roughness elements were used to replicate some of the roughness patterns typically seen in thermal ablative protection systems. The roughness height of the diamond elements was 0.33mm. The final test article was referred to as realistic roughness. The roughness was highly non-uniform and was fabricated with a high-precision additive manufacturing technique.

Table 2.1 shows the values of the blocking ratio (k/δ), the Mach number (M), the roughness height in inner units (k^+), and the Reynolds number (δ^+). These values were used as a guideline to set the flow in fully rough regime. Kocher et al. [36] quote that a value of $k^+ > 70$ and a value of the friction Reynolds number $\delta^+ > 3000$ [39] would set the flow regime as fully rough. The value of δ^+ is equivalent to $k^+ (\delta/k)$. Jiménez recommended small enough blockage ratios to maintain normal wall processes of roughness while having large enough k^+ values to be in the fully rough regime. Multiplying the two values results in δ^+ which can be used as a general guideline for checking if his recommendations are met.

Table 2.1. Mach number and flow-dependent roughness descriptions. Values from UTSI experiment [36]

Roughness Type	M	k/δ	k^+	δ^+
Smooth Wall	2.01	0	0	7500
Diamond Roughness	2.01	0.03	270	9000
Realistic Roughness	2.01	0.04	240	6000

Though the use of k^+ in some roughness types as the appropriate roughness length scale may be appropriate, it is not so in all cases. The fully rough regime is typically classified by values of k_s^+, which is determined by hydrodynamic tests. The replacement of k_s^+ with the inner-scaled roughness height k^+ may be misleading.

The flow conditions and height of the roughness elements are taken from this experiment for use in this study's simulations.

2.2 Mesh Generation

In the following sections, the coordinate system will be defined as follows: x is the streamwise direction, y is the wall-normal direction, z is the spanwise direction.

For this study, three cases were run. A baseline smooth wall case, a medium roughness height case (Case R1), and a small roughness height case (Case R2). The use of medium and small is used in relative terms for the cases. The flow conditions were chosen to match that of the UTSI experiment. A summary of the conditions can be seen in Table 2.2.

Table 2.2. Flow conditions for the numerical simulations.

Parameter	Value
δ_0	5 mm
U_∞	506 m/s
p_∞	26.4 kPa
T_∞	158 K
T_w	266 K
M	2.01
$U_\infty \delta_0 / \nu_\infty$	1.364×10^5

The value of δ_0 is equal to the the boundary layer thickness at the inflow plane. The other parameters are the freestream velocity (U_∞), the freestream pressure (p_∞), the freestream temperature (T_∞), the wall temperature (T_w), the Mach number (M) and the Reynolds number based on the initial boundary layer thickness. The wall temperature was selected as the nominal adiabatic wall temperature for flow of the given Mach number.

The grids were generated with the intent for use in a direct numerical simulation (DNS) or an implicit large-eddy simulation (ILES) of a flat-plate boundary layer. The shape of each grid is a rectangular box comprised of structured hexahedral cells. Three cases were run, and thus three grids generated. The dimensions of each grid were set in terms of δ_0. The length (x-direction), height (y-direction), and width (z-direction) were respectively set to $100\delta_0$, $6\delta_0$, and $6\delta_0$. The length was set to allow sufficient development of the boundary layer. The spanwise sizing is set so that the farthest spanwise planes are uncorrelated from the middle spanwise plane. The wall normal sizing was set to allow for the largest ejections from the boundary layer. The number of grid points in each direction was initially set with the intent of having fair resolution of Δx^+, Δy_e^+ and Δz^+ (the metrics used to evaluate resolution of DNS simulations). Selection of the initial number of grid points in each direction was set to the number of grid points used in previous simulations at a similar Mach number [41]. Achieving the desired resolution involved iterations of different grid sizes, where computations were run with a certain grid and the resolution was inspected. Depending upon the resolution observed, the grid was refined further and calculations were continued on the new grid.

The grid spacing in the wall-normal direction was set to have $\Delta y_0^+ < 1$ at the wall, as that has been seen as a necessary condition to resolve the near wall region [41]. Some iterations of grid sizes were needed to find the sufficient step size at the wall. After the first cell off the wall, the value of Δy^+ was stretched in the wall-normal direction, which is a standard practice as the smallest structures that need to be resolved are generally located near the wall. The grids were generated algebraically, and the stretching ratio defined as $r = \Delta y_{\mathrm{j}+1}/\Delta y_{\mathrm{j}}$ was calculated from a root finding function which aimed to match the specified height of $6\delta_0$ with the specified number of grid points in the wall-normal direction. The values of the number of cells and sizing of the grids are seen in Table 2.3. A sponge layer of 25 cells and a stretching ratio of 1.2 was attached to the top and end of the domain. For the periodic condition in the spanwise direction, 6 overlap grid points were specified.

Table 2.3. Grid sizing for each case.

Grid	N_1	N_2	N_3	N	L_1/δ_0	L_2/δ_0	L_3/δ_0	$\Delta y_0/\delta_0$	r
Smooth Wall	8026	276	626	1.387×10^9	100	6	6	4.5×10^{-4}	1.023
Case R1	8026	276	626	1.387×10^9	100	6	6	2.0×10^{-4}	1.027
Case R2	8026	276	626	1.387×10^9	100	6	6	2.0×10^{-4}	1.027

For the rough cases, the roughness elements were chosen to be represented by a sinusoidal surface. The equation which bound the height of the rough surfaces is

$$y = k \sin\left(2.0\pi \frac{x - x_0}{x_r}\right) \sin\left(2.0\pi \frac{z - z_0}{z_r}\right). \tag{2.1}$$

Here k is the amplitude of the roughness elements (though not necessarily the height of the roughness elements if defined peak to trough), x_0 is the x location where the elements start, x_r represents the wavelength of the elements in the streamwise direction, and the respective definitions also apply to the z variables with the same subscripts. The values are: $x_0/\delta_0 = 5.0$, $z_0/\delta_0 = 3.0$, $x_r/\delta_0 = 2.5$, $z_r/\delta_0 = 0.5$. The result is a wall with features similar to an egg carton. The value of k for Case R1 is 0.05 and the value of k for Case R2 is 0.035. The value of k is the only difference between the grids. Equation 2.1 yields periodic locations where the height is $y = 0$ across the span of the domain. These locations are useful for logging statistics where spanwise averaging is desired.

Visualization of the grid from Case R1 is seen in Figure 2.1. Figure 2.1a shows an isometric view of the grid and the associated size in terms of δ_0 as well as the flow direction. Magnified views of the roughness elements are also shown with shaded views 2.1b and contours of y 2.1c.

To aid in a quantifiable description of the surface, a selection of the parameters from Table 1.2 are calculated for the surfaces of Case R1 and Case R2. The values can be seen in Table 2.4. The experimental process for measuring these variables involves sampling data over a certain length and calculating values from the measured data. Since these parameters are calculated with a sample that is a line, and not an area (with the exception of the effective slope ES), the values were calculated over a line of one roughness wavelength in the streamwise direction. The streamwise variations in roughness seem to be an important consideration in literature [7], so this is assumed to be appropriate.

Table 2.4. Geometric descriptions of roughness elements

Parameter	Case R1	Case R2
ES	0.0509	0.0357
R_q	0.0354	0.0247
R_a	0.0318	0.0223
R_z	0.10	0.070
s_k	0.0	0.0
k_u	1.5	1.5

The value of the effective slope (ES) is small in these cases compared to the value which is typically considered rough. The threshold to be considered a rough surface is cited as $ES > 0.35$ [30] [31]. Surfaces with an ES of less than 0.35 are considered wavy surfaces and the roughness function (Δu^+) does not scale with the roughness height [26]. It is worth mentioning that the ES is purely a geometric quantity and the threshold has been based on incompressible flow studies, and perhaps high-speed applications can still see roughness effects from wavy surfaces. The value of the skewness is equivalent to a Gaussian surface. The kurtosis shows that there are relatively few high peaks and low valleys. For the remainder of this study, the cases with near wall disturbances will continued to be referred to as rough

wall flows, though they would be classified as wavy walls with current definitions used in roughness studies.

2.3 Simulation Configuration

In the setup of the simulations, the no slip condition was set at on the lowest y surface for each grid. The sides of the domain used periodic boundary conditions. The top of the domain and outlet used extrapolation conditions with sponge layers. The inlet boundary condition was specified with a similarity solution of the compressible, laminar boundary layer equations [42]. The flow was imposed with no pressure gradients.

To induce turbulence into the solution, an artificial body force trip method [43] was used with the force maximal at the wall and centered at $x/\delta_0 = 2.5$. The body force added momentum and energy to the corresponding equations. The form of the body force is the same as seen in the study by Poggie et al. [41]. The magnitude of the body force was set by the equation

$$f = \frac{2D_c}{\pi l_1 l_2 l_3} \sin^2\left(\pi \frac{z - z_s}{l_3}\right) \exp\left[-\left(\frac{x - x_s}{l_1}\right)^2 - \left(\frac{y - y_s}{l_2}\right)^2\right]. \tag{2.2}$$

According to Poggie et. al [41] the smooth variation in the form of the trip function made the need for grid clustering around the trip unnecessary. The components of the force were set to

$$\begin{aligned} f_1 &= f\cos\theta \\ f_2 &= f\sin\theta \\ f_3 &= 0. \end{aligned} \tag{2.3}$$

The value of the parameters chosen were $x_s/\delta_0 = 2.5$, $y_s/\delta_0 = 0$, $z_s/\delta_0 = 0$, $l_1/\delta_0 = 0.17$, $l_2/\delta_0 = 0.01$, $l_3/\delta_0 = -1.0$, $\theta = 179.0^o$, and $D_c = 4.0 \times 10^{-3}$. The given value of D_c is nondimensional. It is nondimensionalized by dividing a dimensional value of D_c by $\rho_\infty u_\infty^2 \delta_0^2$.

The calculations were run with nondimensional time steps $u_\infty \Delta t/\delta_0 = 5 \times 10^{-3}$. The values of inner scaled time step (Δt^+) were 0.300 for the smooth wall case, 0.312 for Case R1, and 0.311 for Case R2. For DNS simulations a nondimensional time step of $\Delta t^+ < 1$ is needed for accuracy [44].

To reach a statistically steady state, the flow was allowed to develop for a minimum of three flow-through times ($u_\infty T/\delta_0 = 300$). For these simulations that resulted in a minimum of 60,000 iterations.

Statistics were logged in three planes and two lines. For each case, the three plane locations were identical. A plane containing pressure, heat flux, and shear stress data was collected along the length of the domain at j = 1 and $y/\delta_0 = 0$ (where the index is in parenthesis). A plane was collected along the length of the domain in the x-y plane at $k = 1$ and $z/\delta_0 = 0$ (this was a location where the roughness elements were flat along the streamwise location). The final plane was a y-z plane at i = 7901 or $x/\delta_0 = 98.75$, where the height of the roughness was zero across the span (useful for spanwise averaging of statistics). This location was chosen as opposed to the outlet plane at $x/\delta_0 = 100.0$ because previous simulations showed that noise was present in the exit plane most likely from the presence of the sponge layer following $x/\delta_0 = 100.0$. Two lines across the span were collected for each case for the use of calculating spectra. A flux-line was collected for each case at ($x/\delta_0 = 98.75$, $y/\delta_0 = 0$). Statistics were also collected along a line at ($x/\delta_0 = 98.75$, $y/\delta = 0.5$). The value of δ for each case was slightly different as well as the wall-normal grid spacing. The locations which roughly corresponded to $\delta/2$ for each case are j = 177 or $y/\delta_0 = 1.07$ for the smooth wall case and j = 188 or $y/\delta_0 = 1.09$ for Case R1 and Case R2. Statistics were collected and averaged through time and space for the spanwise lines and plane.

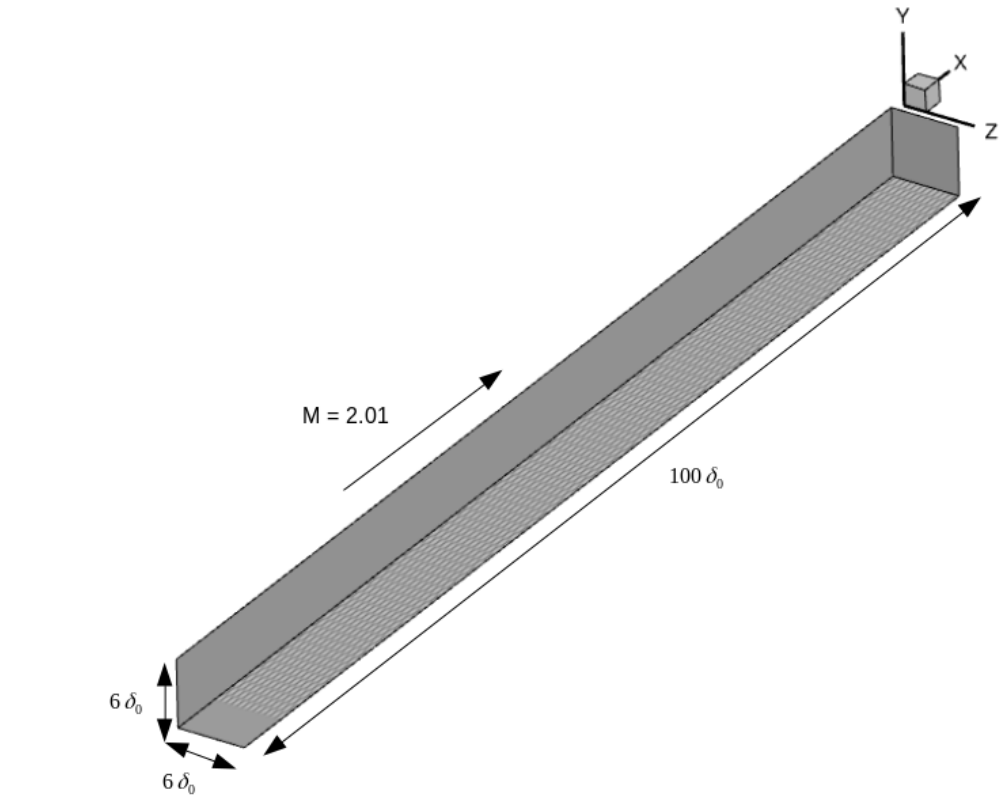

(a)

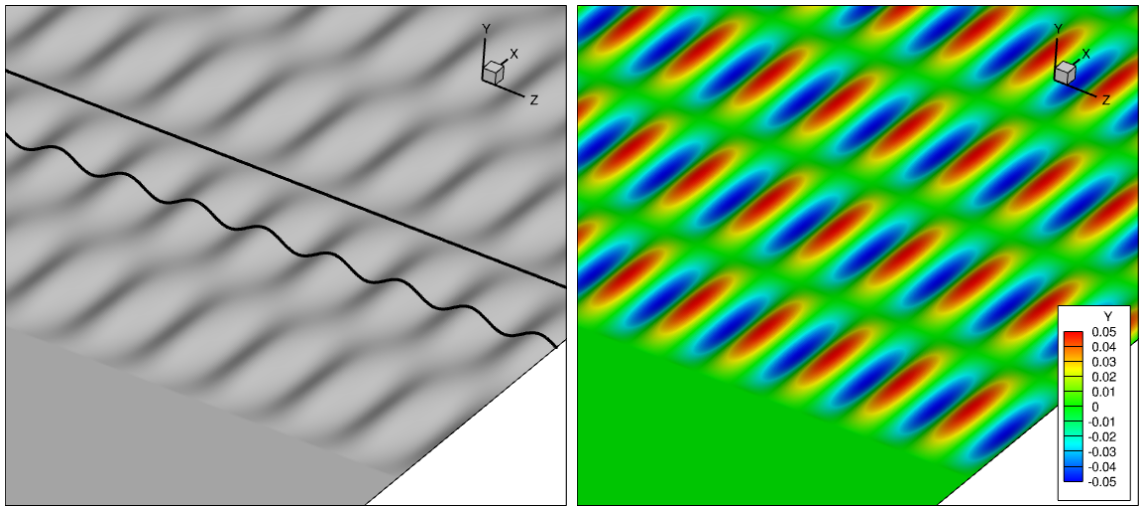

(b) (c)

Figure 2.1. (a) Isometric view of Case R1 grid. The inlet, top, and nearest spanwise slices are removed for visualization of the roughness elements. (b) Magnified view of the roughness elements, shaded with two spanwise lines to aid in visualization of flat and wavy regions across the span. (c) Magnified view of the roughness elements, contour of y to aid in visualization.

2.3.1 WABASH

The computational software used for the simulations was the in-house code WABASH (formerly known as HOPS). A brief summary of the numerical methods is provided by Gaskins et al. [19] and is reviewed here. For more developed descriptions of the numerical methods see the study from Poggie et al. [41].

WABASH is a higher-order direct solver of the Navier-Stokes equations. WABASH uses the Navier-Stokes equations for an ideal compressible gas to represent the physics of the flow. The variables from the conservation equations are transformed from physical coordinates x_i to grid coordinates ξ_i. The resulting form of the equations is

$$\frac{\partial \bar{U}}{\partial t} + \frac{\partial \bar{E}_\mathrm{j}}{\partial \xi_\mathrm{j}} = \frac{\partial \bar{E}^\nu_\mathrm{j}}{\partial \xi_\mathrm{j}} + \bar{S}. \tag{2.4}$$

In this form U is a solution vector represented as

$$U = [\rho, \rho u_1, \rho u_2, \rho u_3, \varepsilon]^T. \tag{2.5}$$

E_j is the inviscid flux vector. The viscous flux vector is E^ν_j. $\bar{U}$, $\bar{E}_\mathrm{j}$, and $\bar{E}^\nu_\mathrm{j}$ are transformed solution and flux vectors defined as

$$\bar{U} = \frac{U}{J} \tag{2.6}$$

$$\bar{E}^\nu_\mathrm{i} = \frac{\partial \xi_\mathrm{i}}{\partial x_\mathrm{j}} \frac{E_\mathrm{j}}{J}, \tag{2.7}$$

where J is the grid transformation Jacobian. A spatial compact differencing scheme is used to solve these equations. The scheme is sixth-order at interior points and fourth-order at boundaries. For temporal discretization, second-order time accuracy is achieved by using an implicit method similar to the Beam-Warming Scheme [45]. Numerical instabilities which grow in the solution can be a consequence of the use of higher-order methods. To mitigate these instabilities, a low-pass, non-dispersive filter is used after each subiteration.

2.4 Computational Resources

For the computations, the Department of Defense's (DoD) High Performance Computing Modernization Program's (HPCMP) resources were used. Initial calculations were carried out on the army's Engineer Research and Development Center (ERDC) cluster named Onyx. Final calculations were performed on the navy's DoD Supercomputing Resource Center (DSRC) cluster named Narwhal. A brief explanation of the calculations on Narwhal is provided here.

The benefit of large computing systems is the ability to parallelize computations by splitting work between compute nodes. On Narwhal each compute node has 128 cores available for computations. The computational domain (grid) has to be broken into subdomains, each handled by one MPI rank. The number of ranks should be an integer multiple of the number of cores per node. A general rule of thumb for splitting the domain into subdomains is to have somewhere between 70-120 cells per direction in the subdomain [46]. For the current study's domain, the number of grid points in the (x, y, z) directions is (8026, 276, 626). The subdomains were split to be sized (128,3,6) with the typical amount of cells per subdomain in each direction being (62,92,104).

The subdomains will be given to compute nodes for calculations. The number of subdomains per node is equal to the number of message passing interface (MPI) processes (ranks). The MPI processes are further split by the number of threads, which is an integer value per process. The number of threads multiplied by the number of MPI processes per node should equal the number of cores per compute node. This results in only a certain integer number of choices between the number of MPI processes and the number of threads. To select the number of nodes needed for the calculation, divide the number of ranks by the number of MPI processes. Intuitively, that leads to more compute nodes required for fewer MPI processes. Generally more compute nodes will result in faster computations (to the limit where the cost of communication outweighs the benefits of more computational resources). Practically, the number of compute nodes is chosen from a parametric study investigating how iteration times decrease as the number of threads is increased (and number of MPI processes are decreased). The selection of the number of nodes is chosen by seeing at what

point the return on computation time compared to computational resources needed becomes diminishing. For these computations a selection of 16 MPI processes and 8 threads was chosen which resulted in 144 nodes (18,432 cores per case). For scale, a typical laptop may have a 4 core processor, compared to the 128 cores per node on Narwhal.

Cost of computations is reported in core-hours. Core-hours is the amount of cores used multiplied with the hours ran. For this study, 24 hours of run-time on one case results in a computational cost of 442,368 core-hours. Three cases run simultaneously for 24 hours results in a cost of 1.3 million core-hours. The cost for one case to reach a statistically steady state from three flow-through times and an additional three-flow times for collection of statistics is approximately 1.1 million core-hours.

3. RESULTS

In this chapter, the results of the simulations will be discussed. These simulations give a plethora of data, and choosing what to analyze can be challenging. To be methodical in the approach to processing the data, the analysis has been broken into two main sections. The first section will deal with visual analysis of the flowfield. After a visual analysis, the flow will be examined with statistical methods.

3.1 Overall Flow Structure

This section will explore visualizations of the flowfield. In an effort to organize the results, there will first be a subsection showing the visualizations of the smooth wall case. This will set a baseline for comparison to the rough wall cases. This may also prove useful in future investigations into coherent structures in a compressible turbulent boundary layer.

3.1.1 Smooth Wall

To start, an illustration of the flow will be useful to understand the domain of the computation. Figure 3.1a shows the start of the computational domain for the smooth wall case. At $x/\delta_0 = 2.5$, the body force used as a trip in the flow can be seen. There is a shock at the location of the trip which extends outwards in the flow (a planar view can be seen in Figure 3.1b). After this bypass transition mechanism, a turbulent boundary layer can be seen developing. The turbulent boundary layer is allowed to continue to develop further downstream to $x/\delta_0 = 100$.

Figure 3.2 shows a block taken from the end of the computational domain with contours of normalized density. Figure 3.3 shows magnified views of the slices from the isometric view. The axes of the figures are in terms of δ_0 since that is how the geometry of the computation was defined. From the figures it can be seen that at the end of the computational domain, the value of the boundary layer thickness (δ) is approximately $2\delta_0$.

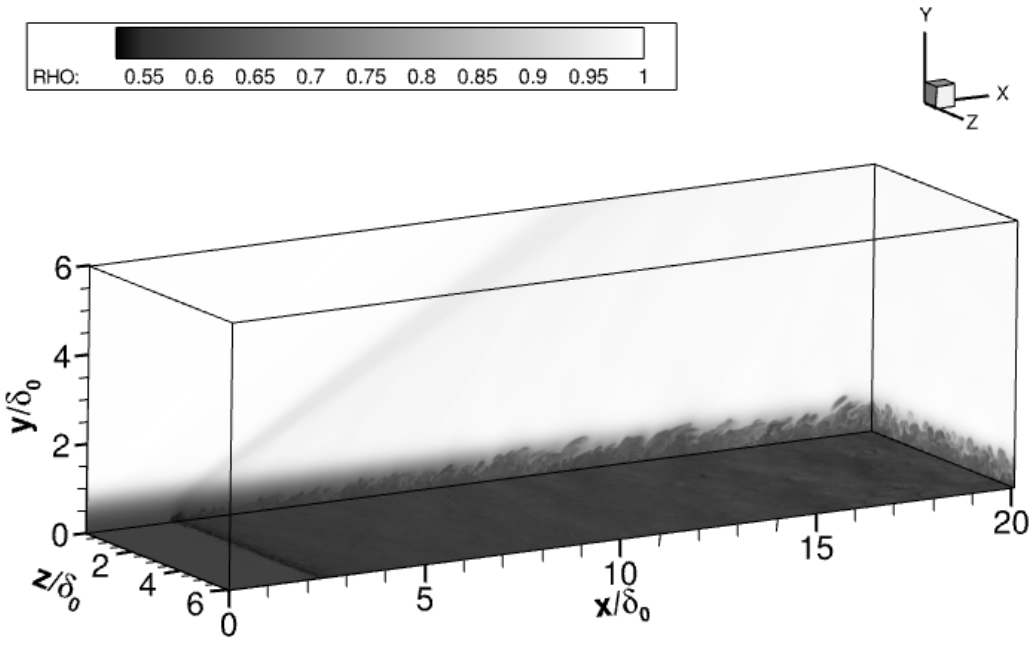

(a)

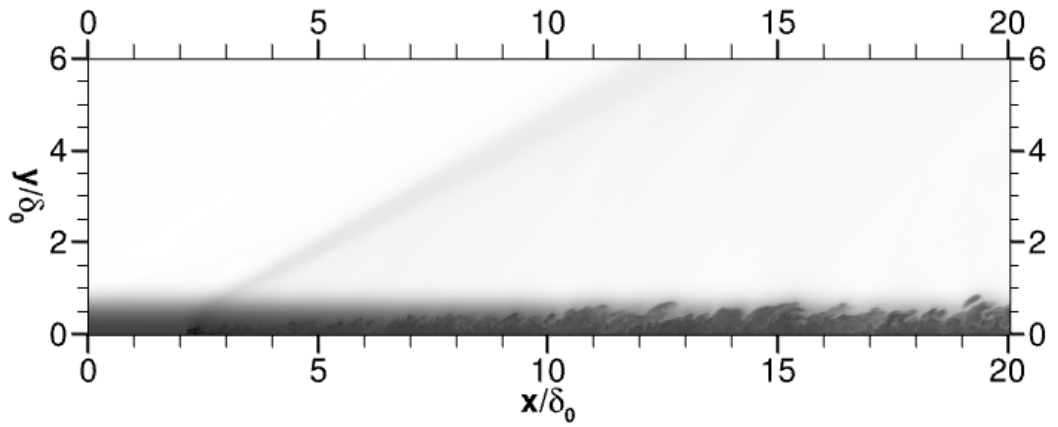

(b)

Figure 3.1. (a) Isometric view of a block at the start of the computational domain of the smooth wall case with a contour of normalized density.(b) Planar (xy) view at the start of the computational domain of the smooth wall case with a contour of normalized density.

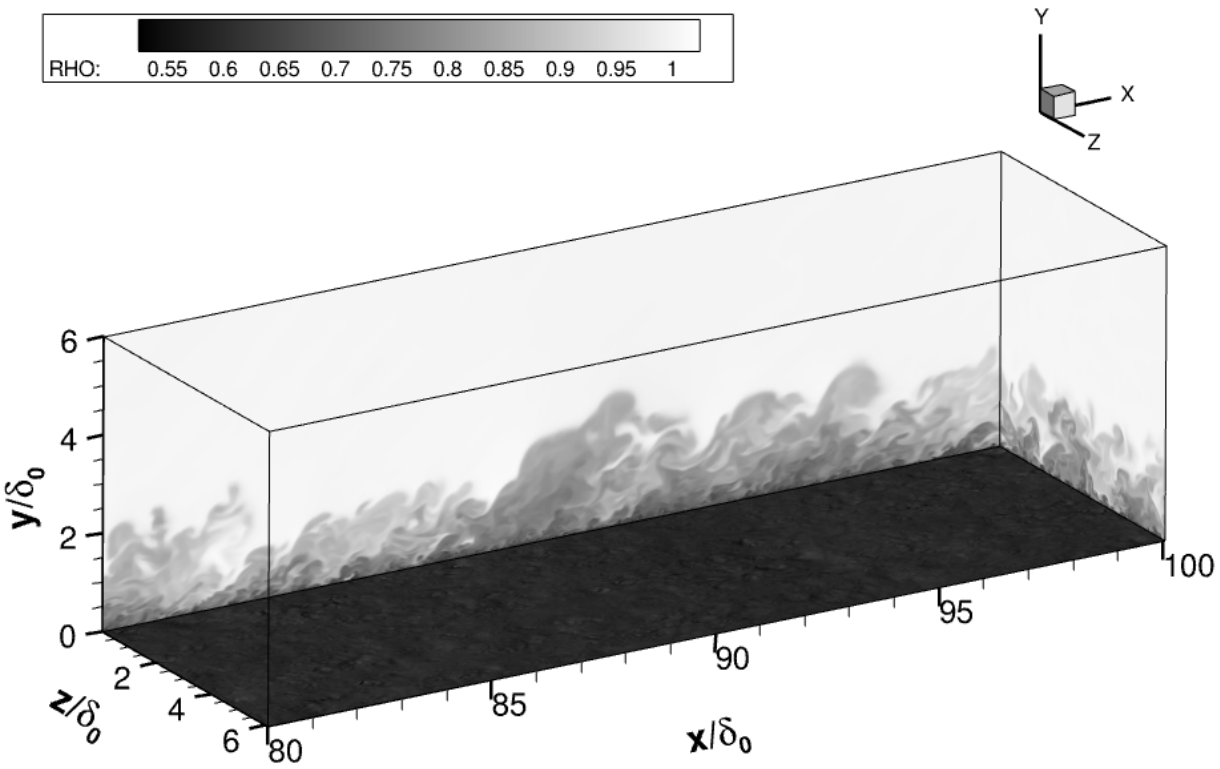

Figure 3.2. Isometric view of a block at the end of the computational with a contour of normalized density.

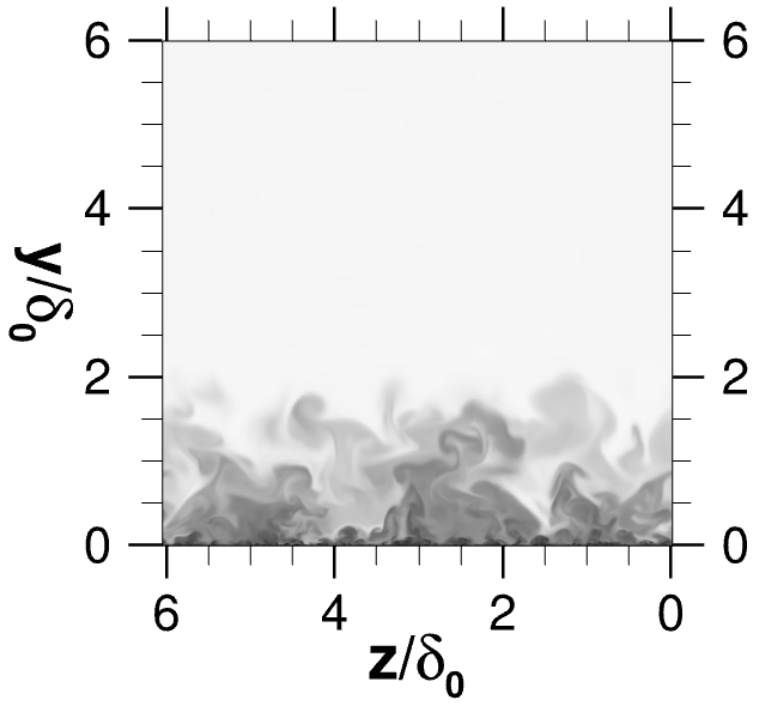

(a)

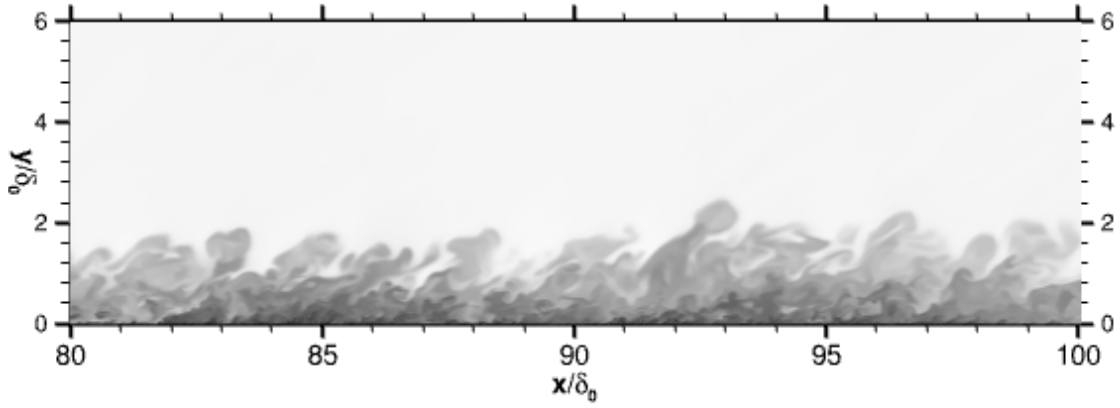

(b)

Figure 3.3. (a) A y-z planar view looking downstream of the flow with a contour of normalized density.(b) An x-y planar view of the end of the computational domain.

In Figure 3.3b typical structures observed in turbulent boundary layers are seen. Sweeps of high speed fluid toward the wall can be seen following the large turbulent structures. These are seen from the light colored fluid reaching into the the boundary layer. The sweeps seem to follow structures which could be ejections of low-speed fluid, though it may be difficult to classify the structures as ejections without an animated flowfield or correlations between u' and v'. The upstream side of the δ-scale turbulent structures which are in direct contact with the freestream fluid is called a back, and the opposing side is a front. Between the large scale structures are valleys. The structures also show a tendency to be inclined approximately 45°. Figure 3.3a also shows similar structures with the exception of the inclination angle due to the point of view being streamwise oriented.

In addition to the slices taken of an x-y plane and a y-z plane, slices taken in the x-z plane at various heights (y, though y will be described in terms of nondimensional quantities) are useful for visualizing coherent structures in the flow. Pirozzoli and Bernardini [47] inspected slices at various heights from the wall in a supersonic boundary layer and witnessed commonly seen streaks in the flow of low and high-speed fluid. Figure 3.4 shows normalized density contours (using the freestream density as the normalization factor) for slices of various wall-normal distances.

Figure 3.4a shows streaks in the region very close to the wall with a y^+ location associated with the buffer region. The value $y^+ = 18$ was chosen due to it being the location of peak streamwise Reynolds stress ($\overline{u'u'}$) and a similar method was used by Pirozzoli and Bernardini [48]. These streaks have been shown to be associated with quasi-streamwise vortices [18]. To investigate the presence of vortices which are associated with the streaks, isosurfaces of q-criterion were used. Figure 3.5a shows a magnified view of the near wall streaks. Figure 3.5b shows the same image with superimposed isosurfaces of q-criterion. There is a clear correlation between the vortices and the low-speed streaks. The patterns of high and low-speed fluid in this layer have been suggested to be remnants of sweep and ejection events [47]. Some hypotheses have stated that these streaks can grow to become large scale structures of the turbulent boundary layer as they are lifted up. Jiménez [3] has hypothesized that disruption of the buffer-layer viscous cycle which generates a significant fraction of the turbulent energy (also the location of the streaks) can subsequently affect

the large scale structures of the turbulent boundary layer and thus violate the idea of wall-similarity for rough surfaces. The presence of this pattern of fluid has also been observed in DNS studies by Duan et al. [49] [50]. The spanwise spacing of the streaks has been shown to be Reynolds number dependent, with larger Reynolds numbers showing finer scale structures [47]. There also appears to be secondary scales associated with the streaks, where fine scale streaks gather to form a larger clustered pattern. This is also consistent with findings from Pirozzoli and Bernardini [47]. The characteristic length scale of the width of the low-speed (dark) streaks is approximately $y^+ = 50$. For the higher speed streaks, the characteristic length scale of the width is approximately $y^+ = 250$ (about 5 times the width of the narrow streaks).

Figures 3.4b and 3.4c show the development of the streaks as the slice of the flow in view moves upwards in the boundary layer. The high-speed streaks begin to grow in the spanwise direction and show sharp features reaching in the spanwise direction. There still seems to be the presence of multiple length scales which the streaks seem to be bound by. There is the width of individual streaks and a width of a cluster of streaks. The dark low speed fluid seems to lose coherence as the value of y^+ increases.

Figure 3.4d shows a slice of the flow at $y/\delta = 0.3$. Here the streaking pattern seems lost, though there are still regions clearly associated with higher and lower speed fluid. At a location of $x/\delta_0 = 93$ and $z/\delta_0 = 2$ there appears to be a structure similar in shape to a mushroom. This could possibly be the presence of a horseshoe or hairpin vortex. Pirozzoli and Bernardini [47] still witnessed streaking patterns at this location with different contours of fluctuating streamwise velocity. Perhaps a different contour could show more coherence.

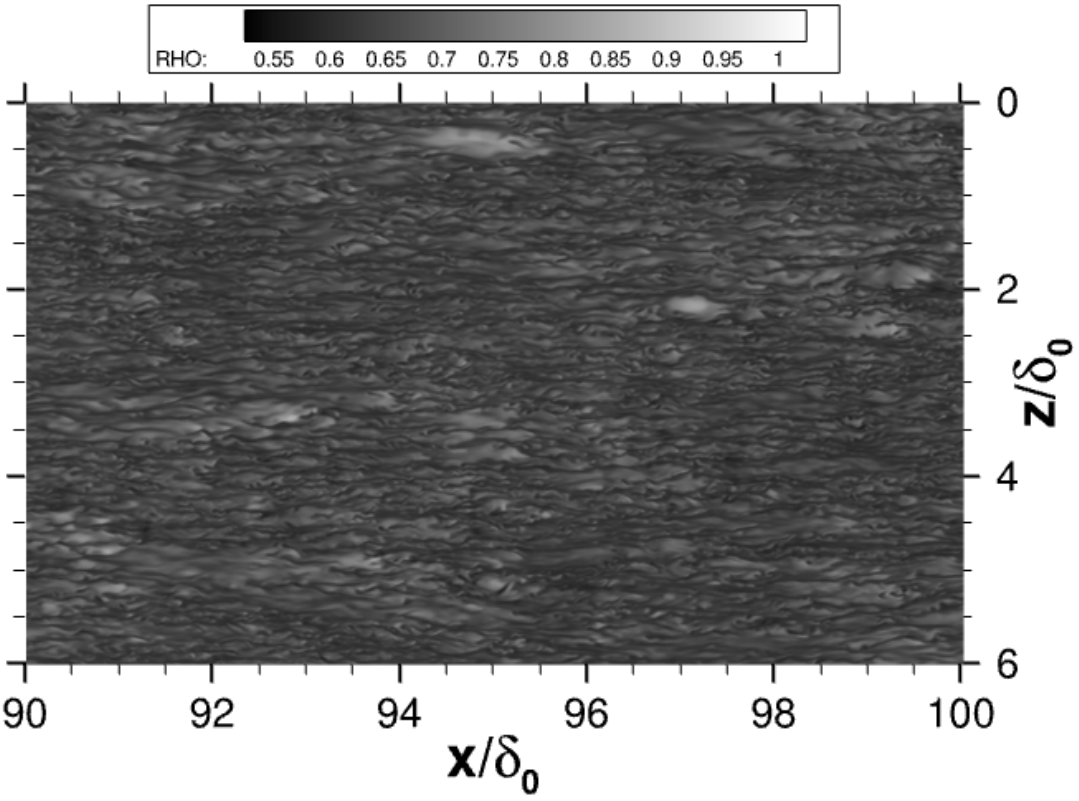

(a) $y^+ = 18$, $y/\delta = 0.005$

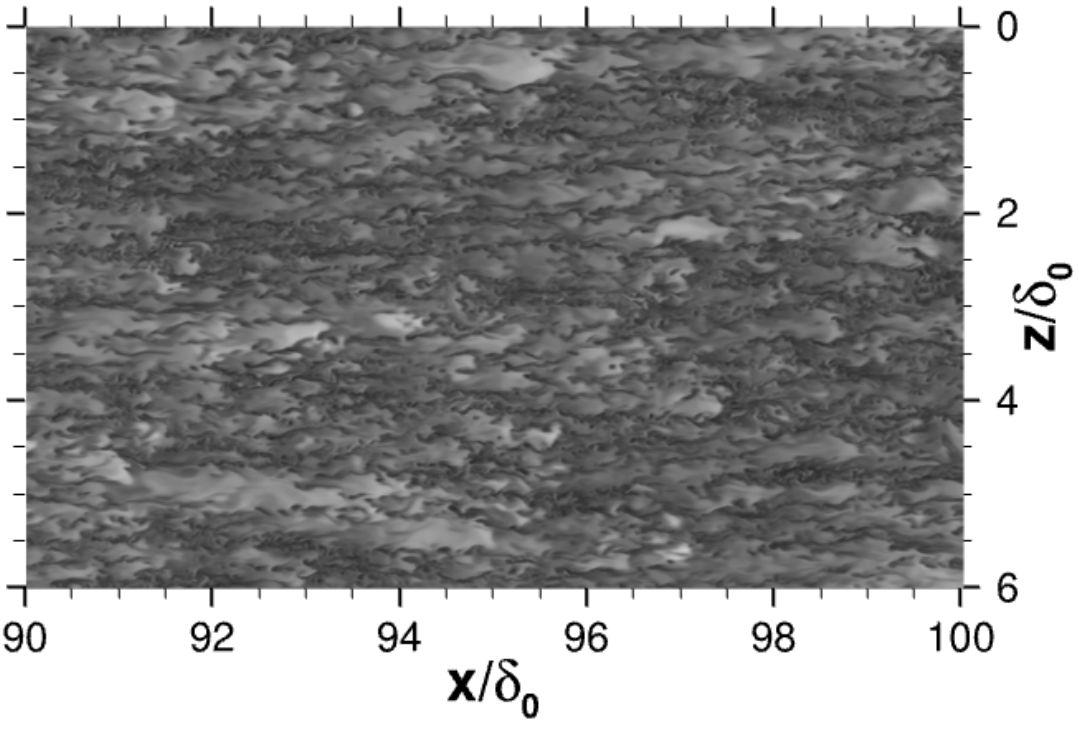

(b) $y^+ = 55$, $y/\delta = 0.015$

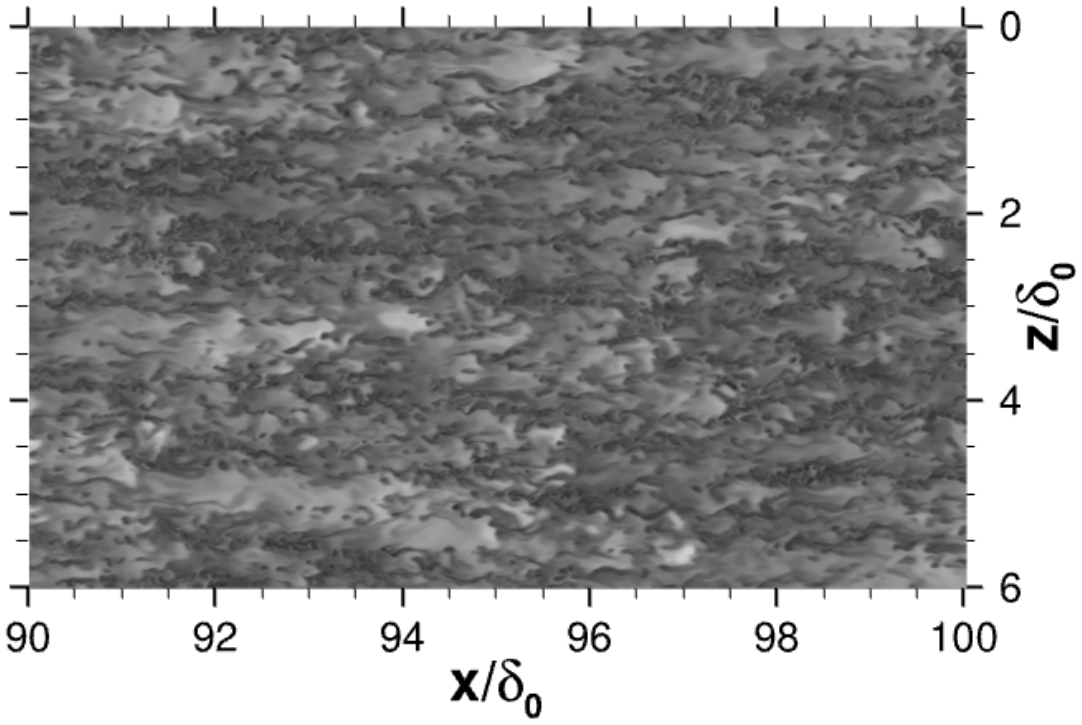

(c) $y^+ = 80$, $y/\delta = 0.021$

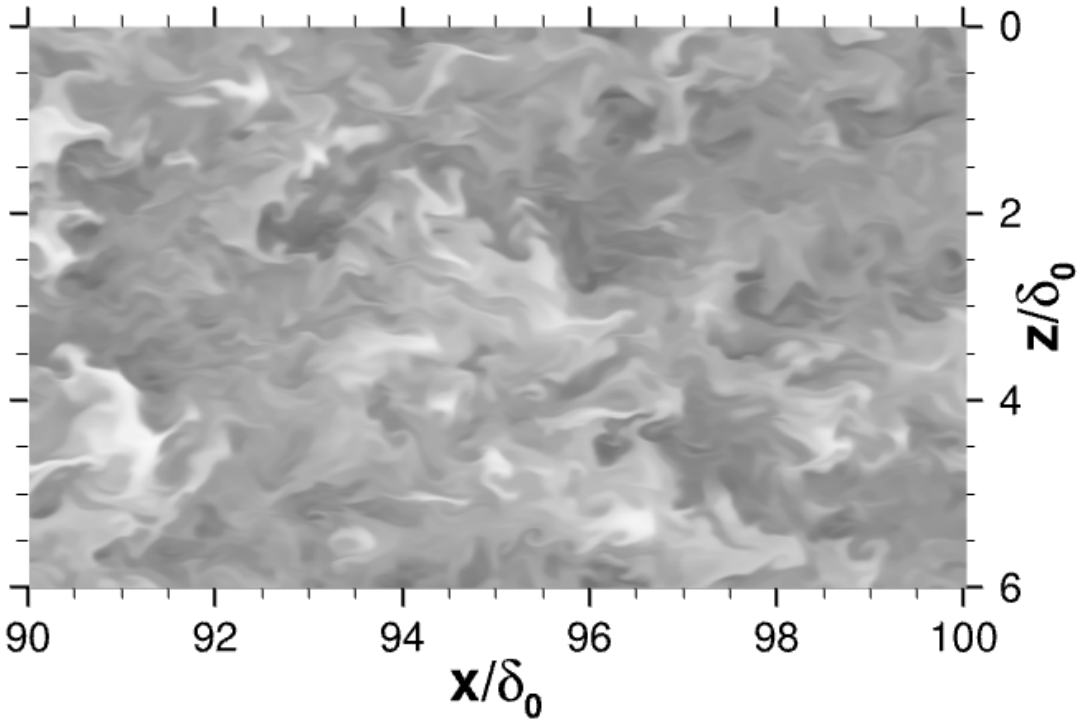

(d) $y^+ = 1100$, $y/\delta = 0.3$

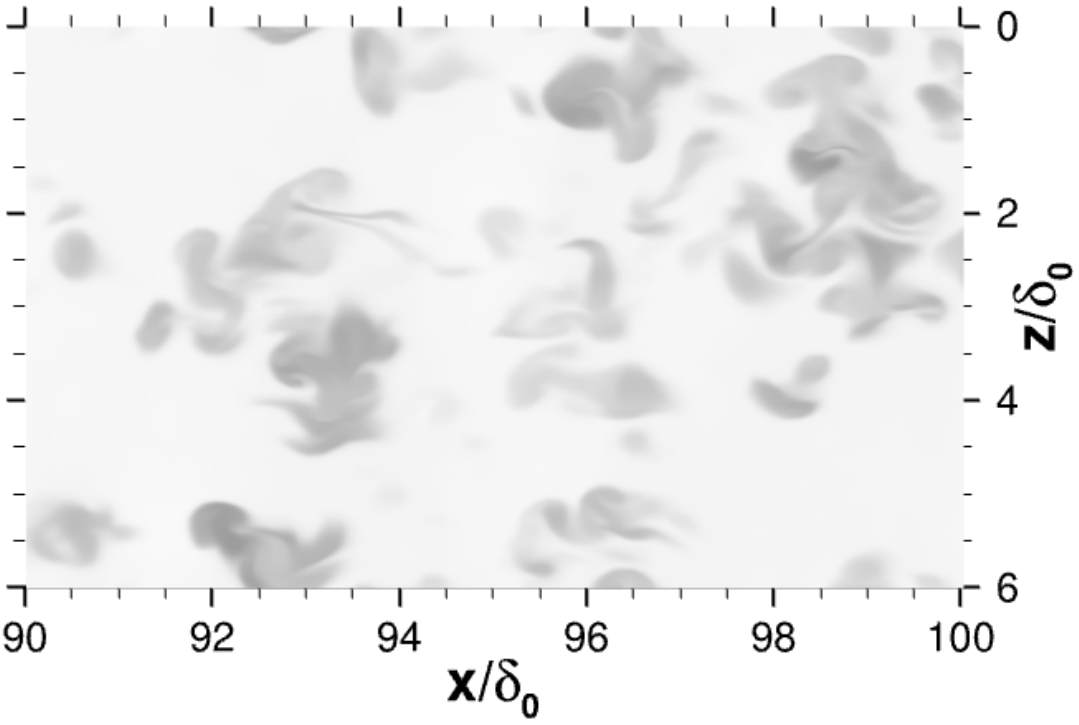

(e) $y^+ = 3480$, $y/\delta = 0.95$

Figure 3.4. Slices at various wall-normal locations with the location described in inner unit [(a),(b),(c)] and outer units [(d),(e)]. Contours of density normalized by freestream density.

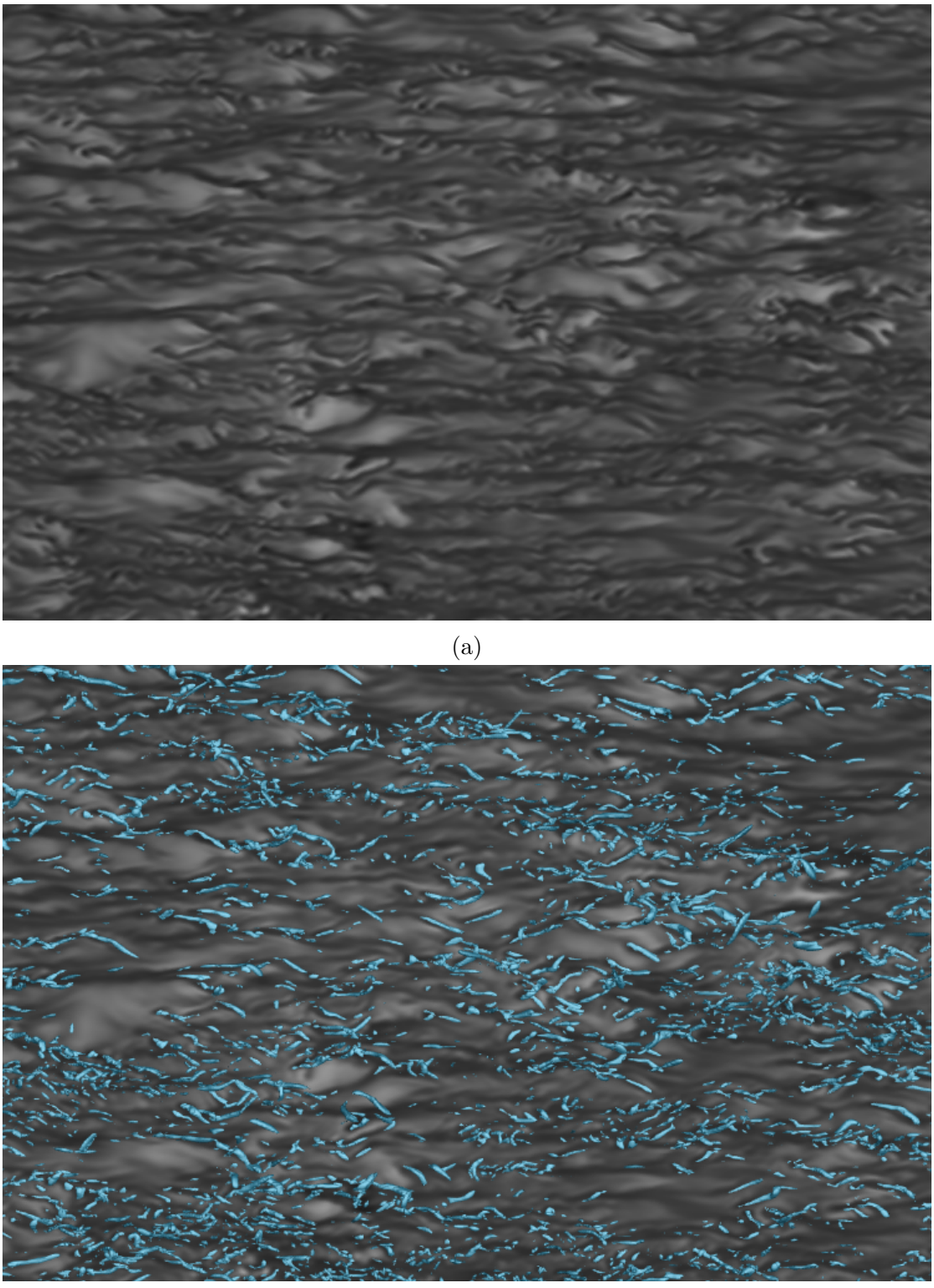

(a)

(b)

Figure 3.5. (a) Magnified view of the streaks in Figure 3.4a.(b) The streaks seen in (a) with isosurfaces of q-criterion = 100.

Figure 3.4e shows a plane at $y/\delta = 0.95$. Here the turbulence is isolated to specific regions mixed between freestream fluid. The interface between black and white in this image is approximately the location of the viscous superlayer, the interface between rotational and irrotational flow. The dark regions are slices through the bulges seen in side-view images of the boundary layer. The shape observed in Figure 3.4d seems to develop into a shape similar to a jellyfish at the edge of the boundary layer. The pattern of the shape can be seen in various locations of the slice. To investigate if these patterns could be slices through the top of a horseshoe vortex, the y vorticity was plotted of the same frame. Here the y vorticity would be coming out of the page and a very narrow contour range was set to see if there were regions of opposite sign vorticity. The y-vorticity can be seen in Figure 3.6 with a side by side comparison to the density contour. There appears to be association between counter rotating pairs, suggesting that they could be connected by an overarching horseshoe structure.

Though planar views of the flow can be very insightful into structures of the flow, a benefit of the computational approach of this study is the fact that three-dimensional structures can be visualized. The Q-criterion is a method that has been used to try and demonstrate the presence of coherent vortical structures (and was used in Figure 3.5b to show the presence of quasi-streamwise mostly planar vortices). To investigate the flow for coherent 3-D structures the Q-criterion of a block at the end of the computational domain was calculated and shown as an isosurface in Figure 3.7. Upon first investigation, there seems to be the presence of many horseshoe vortices in the outer layer and other associated structures such as arches. At this delta scale view of the flow, these are the only clear structures seen. Figure 3.8 shows a magnified view of a horseshoe vortex for reference. These figures further encourage the hypothesis that the structures from Figure 3.4e and 3.6 are indeed slices of the tops of horseshoe vortices.

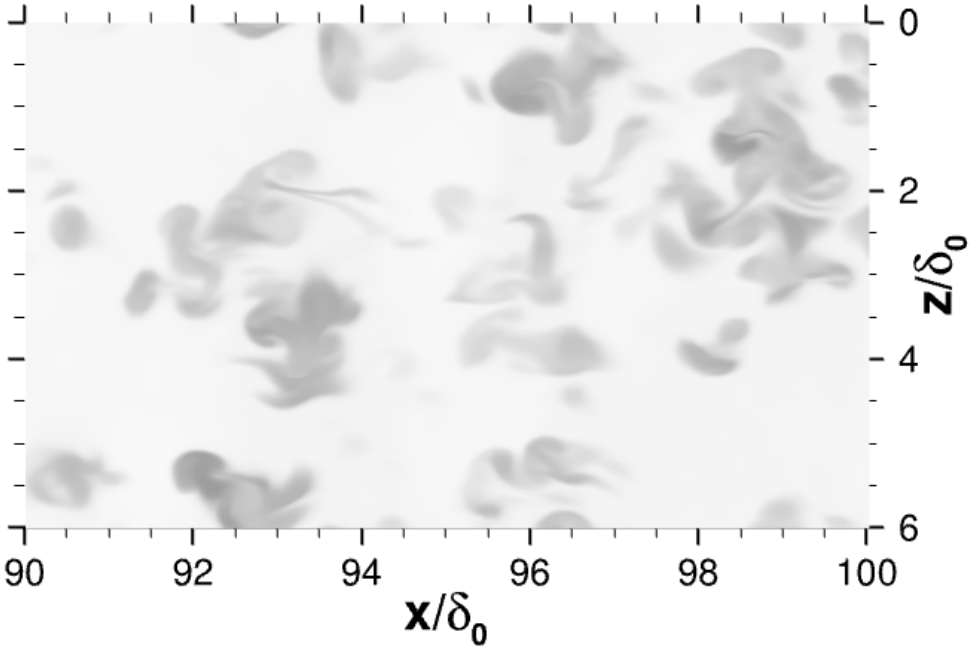

(a)

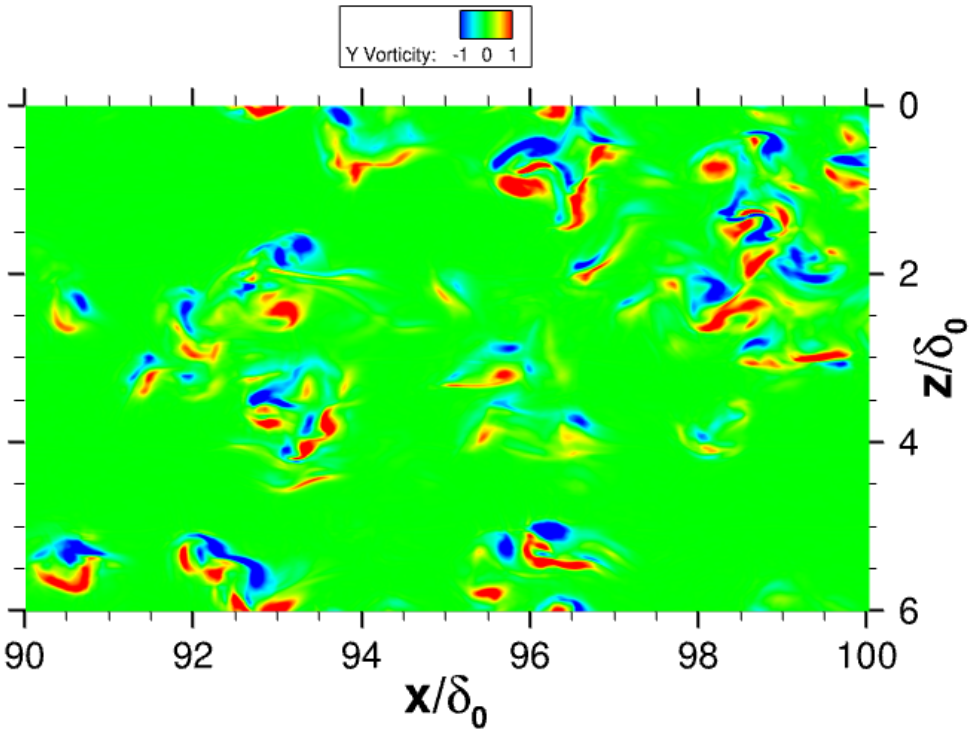

(b)

Figure 3.6. (a) An x-z planar view of the flow with a contour of density. (b) An x-z planar view of the flow with a contour of y-vorticity. There is an association between counter rotating pairs in some locations.

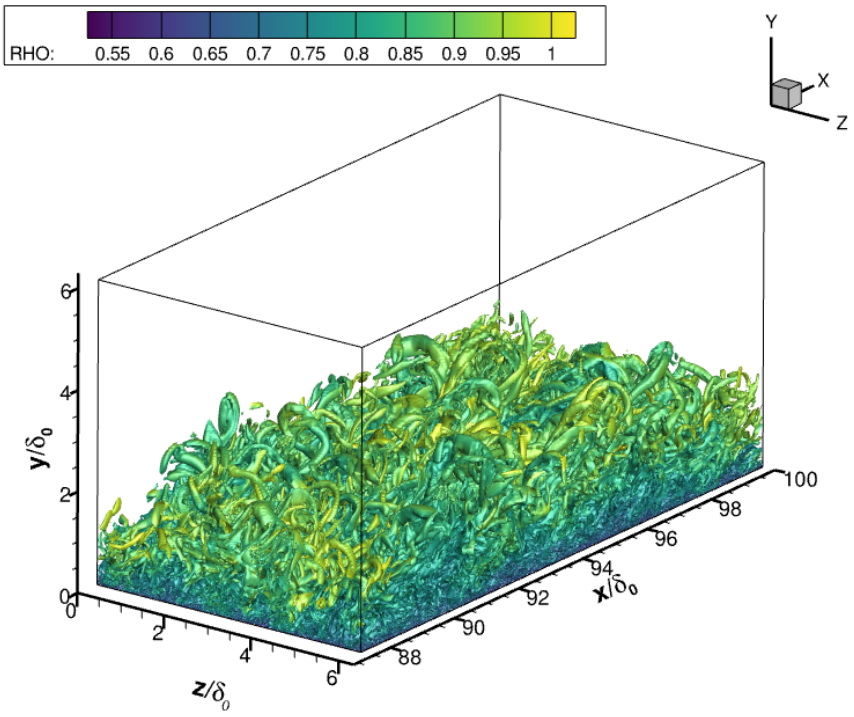

Figure 3.7. Isometric view of a block at the domain with isosurfaces of q-criterion = 0.15 and contours of density.

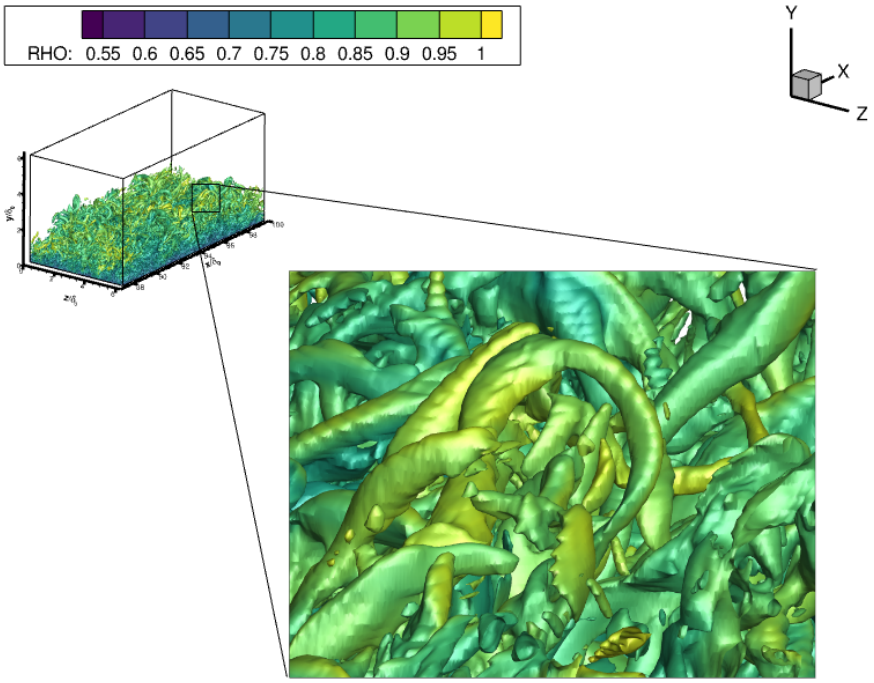

Figure 3.8. Magnified view of a horseshoe vortex with an isosurface of q-criterion isosurface = 0.15 and contour of density.

3.1.2 Rough Wall Cases

The previous section dealt with different methods of visualizing the flow of an ideal flat wall boundary layer. This section will visualize the flow for the medium roughness (Case R1) and the small roughness (Case R2) cases in the same manner as the smooth wall case in an attempt to identify any visual differences.

Case R1

The structure of the boundary layer will first be investigated with a slice in the x-y plane. Figure 3.9 shows a slice of the boundary layer with a contour of density normalized by freestream density. The slice was taken at a location where the roughness elements had their maximum difference between peak and trough. For comparison, the smooth wall case is also given in the figure. Upon inspection of the structures sized on the order of δ, there seems to be some differences between the size of the boundary layer and the intermittency of the structures. Case R1 seems to have more uniform sizing of the structures and perhaps greater intermittency. Bowersox and Latin [34] [35] found that roughness elements in the fully rough regime protrude into the supersonic region of the boundary layer, causing shock waves and expansion fans around the elements. This behavior is not observed here.

The near wall region has a different range of length scales and is also investigated visually. Figure 3.10 shows magnified views of the flow in the R1 and smooth wall case. The valleys of the roughness elements seem to show clusters of small structures that are not seen in the smooth wall case. Videos of the flow show that the valleys seem to be active regions of turbulence where there is much more turbulent motion as compared to the near wall region of the smooth wall case.

An area of particular interest to roughness studies is how the near wall streaks of low and high speed fluid as seen in Figure 3.4a are effected by the presence of roughness elements. Similar to the smooth wall case, the R1 case is visualized with slices at constant y locations (though varying wall-normal distance due to the waviness of the surface) in the x-z plane. These slices can be seen in Figure 3.11. Figure 3.11a shows a slice through the plane of peak streamwise Reynolds stress ($\overline{u'u'}$). The white ovals are cuts through the roughness elements

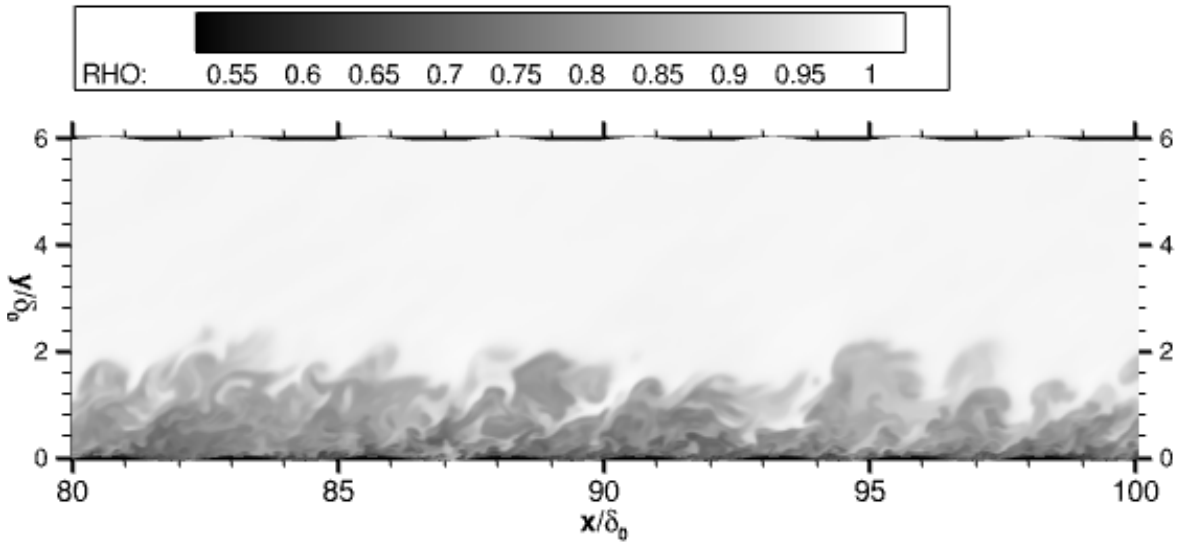

(a) Case R1

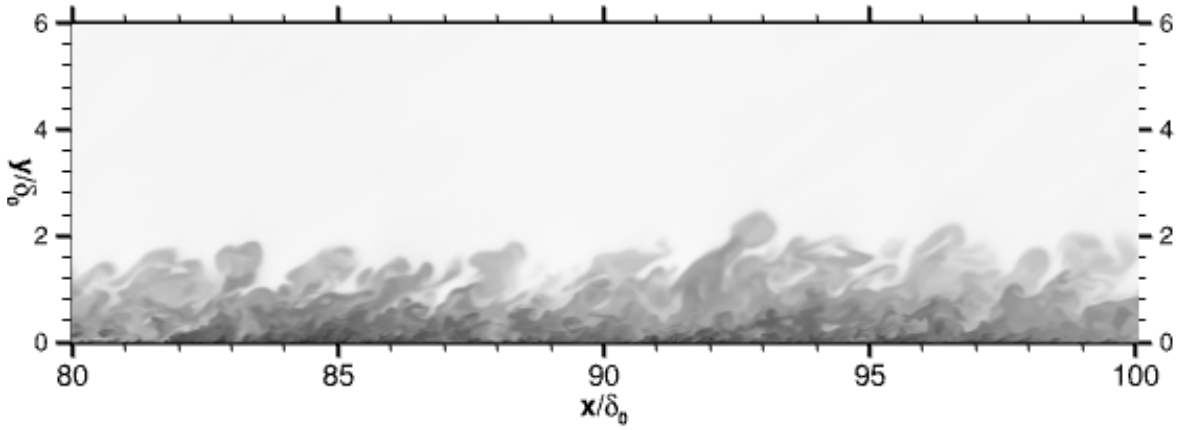

(b) Smooth Wall

Figure 3.9. Comparison of the delta scale structures of the R1 (a) and smooth wall (b) cases. Contours are of density normalized by the freestream density.

with the flow between them. Here we can see that in comparison to the smooth wall case, there is no clear streak pattern apparent in this plane. Since the surface may be considered wavy, it may be useful plotting a plane with a constant wall-normal distance in the rough cases. Plotting in this manner may show if the streaks seems to follow the wavy surface, moving smoothly up and down along the surface instead of being completely disrupted by the roughness elements. These planes are also shown in Figure 3.11 and are labeled as "wavy planes". Some of the streaking pattern is recovered when the plane is plotted this way as seen in Figure 3.11b. The low-density streaks also seem to group into larger streaks, most likely related to the presence of the roughness elements forcing the streaks to navigate through similar paths. Since the streaks are associated with quasi-streamwise vortices, it is worth investigating for the presence of vortices.

Figure 3.12 shows a magnified view of the plane where $y^+ = 18$ with isosurfaces of Q-criterion. Though the streak pattern is difficult to see, an isometric view of the 3-D Q-criterion sheds some light on what could possibly be occurring in the flow. The vortices seem to have more three dimensionality. They cluster together between the roughness elements and stack vertically. This intuitively makes sense as the three dimensional nature of the surface would introduce more three dimensional behavior to the flow. This is also consistent with what was shown in Figure 3.11b, where the streaks are seen clustering into larger streaks which seem to navigate around the roughness elements. The smooth wall case showed the vortices mostly remaining quasi-planar.

Figure 3.11c shows some similar behavior as compared to the smooth wall case. Some of the streak pattern is recovered but with more organized structure as a consequence of the presence of roughness elements. The wavy plane shows more similarity to the smooth wall case with a bit more organization of the streaks as a consequence of the roughness elements. In Figure 3.11e the location of the slice was selected due to a secondary peak in the Reynolds stress profile at this location ($y^+ = 80$). Here some of the streak pattern is similar to smooth wall case. A notable difference is how the roughness elements act as as sources of low-density, low-speed fluid into the flow. This creates trails behind the elements with thin streaks of low-speed fluid similar to the low-speed streaks seen at $y^+ = 18$ in the smooth wall case (see Figure 3.4a). The low-speed fluid trailing behind the roughness elements introduces mean

velocity gradients not seen in the smooth wall case. Since turbulence generation is related to mean velocity gradients and Reynolds shear stresses, there could be increased production of turbulent kinetic energy around the elements. The wavy plane in Figure 3.11f shows much more similarity between the smooth wall and rough case, suggesting the patterns in the flow are following the surface geometry.

The slice in Figure 3.11g is very similar to the smooth wall case with no discernible difference between the two. Once again some structures are visible (see $x/\delta_0 = 93$, $z/\delta_0 = 5$). Figure 3.11h shows the jellyfish-like structures in the very edge of the boundary layer which were previously shown to be associated with horseshoe vortices. Figure 3.13 shows a comparison between the density contour and a plot showing the direction of y-vorticity. The same pattern as before is seen where counter rotating vortices are paired.

To investigate the three dimensional structure of the boundary layer, the Q-criterion was plotted as isosurfaces with contours of density for case R1. An isometric view can be seen in Figure 3.14. The horseshoe vortices are still seen and are magnified in Figure 3.15. At this scale of the flow there appears to be no discernible difference between Case R1 and the smooth wall case.

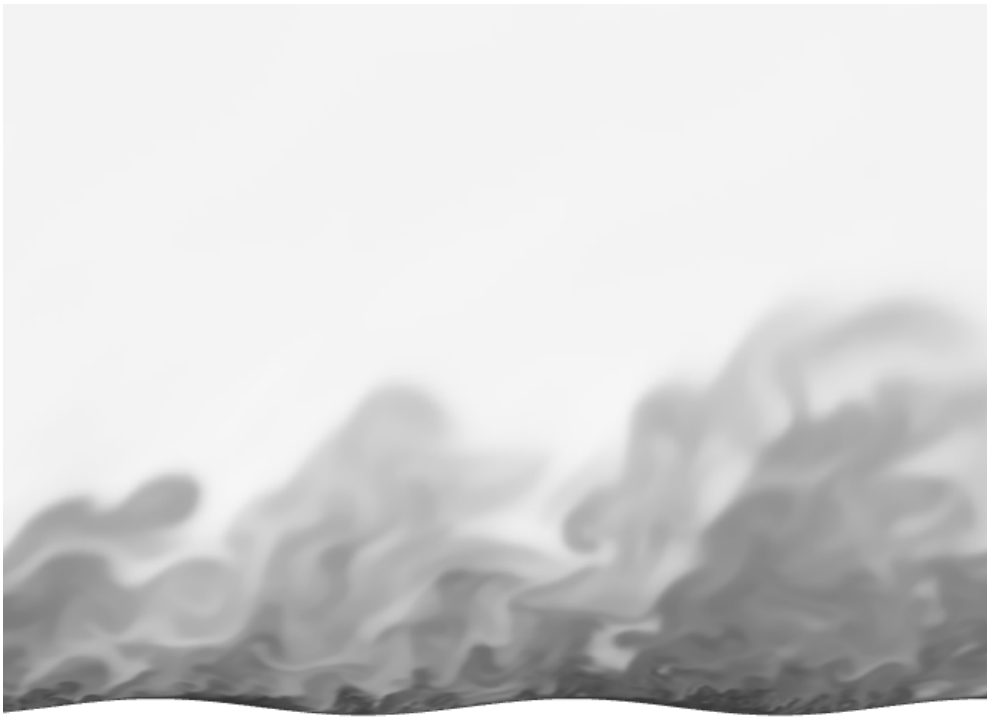

(a)

(b)

Figure 3.10. Comparison of the near wall structures for the R1 (a) and smooth wall (b) cases. Contours are of density normalized by the freestream density.

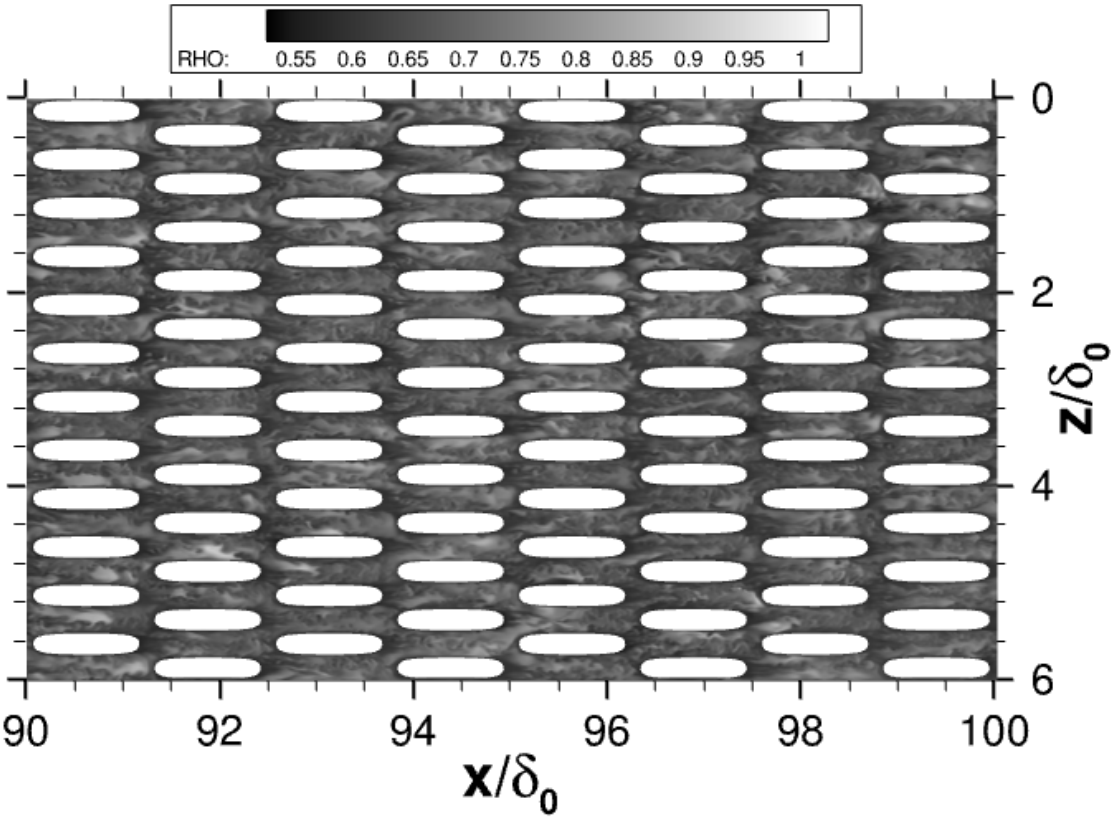

(a) $y^+ = 18$, $y/\delta = 0.005$

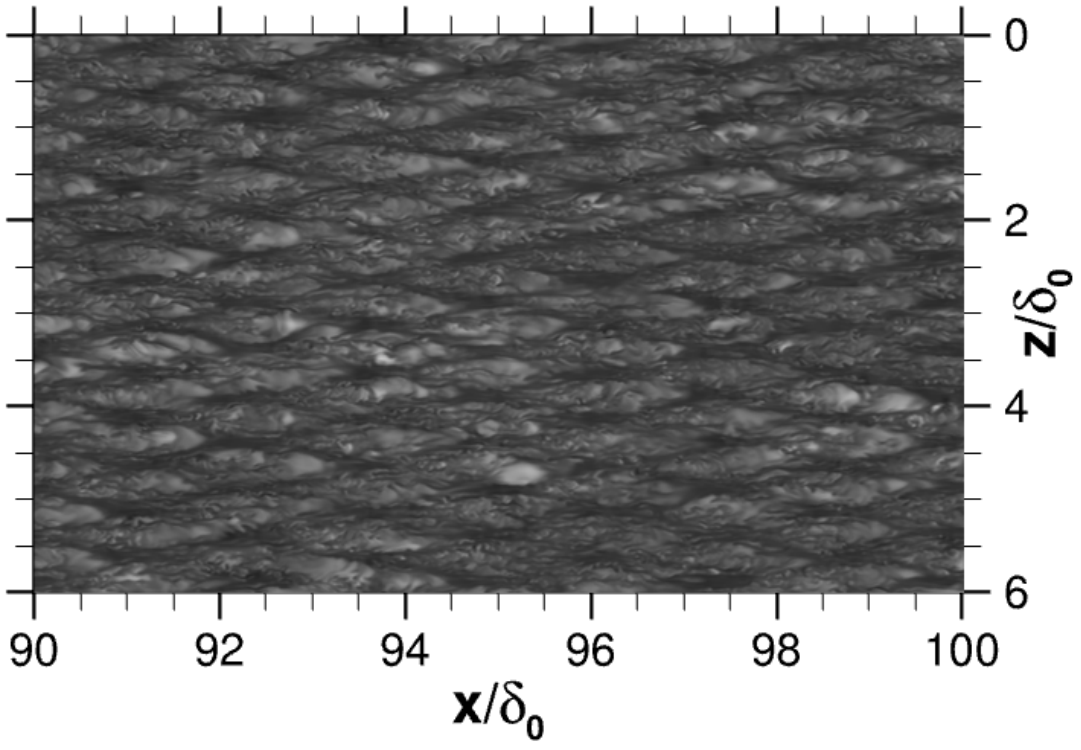

(b) Wavy Plane $y^+ = 18$, $y/\delta = 0.005$

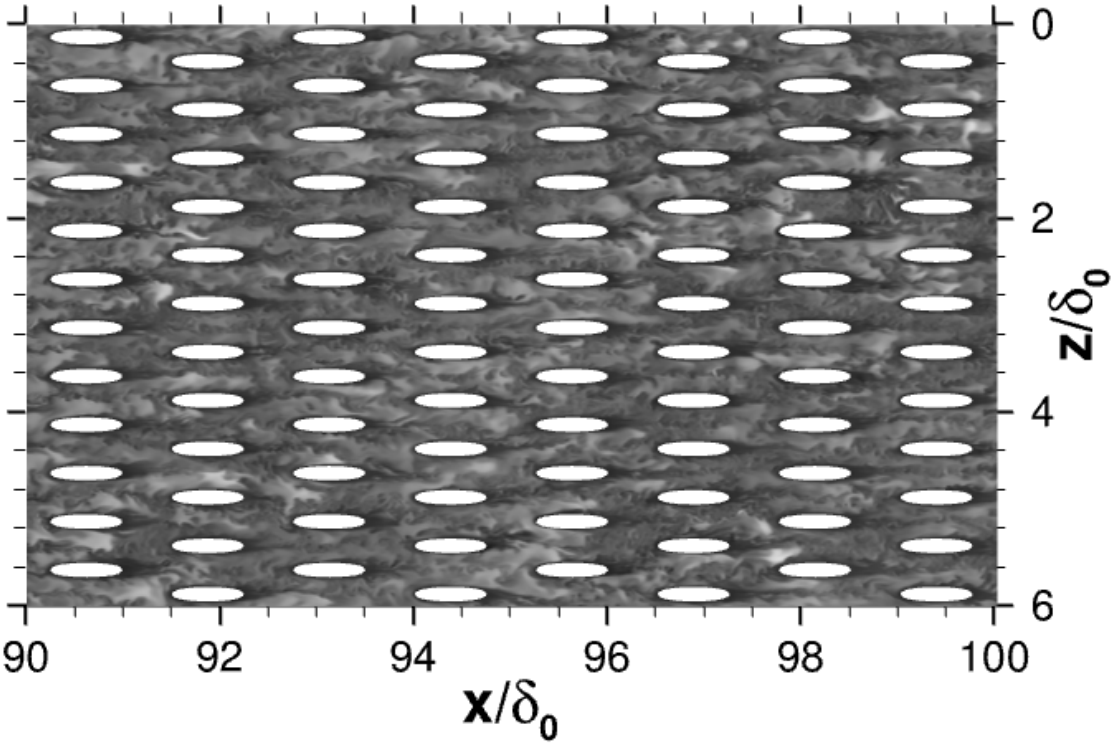

(c) $y^+ = 55$, $y/\delta = 0.015$

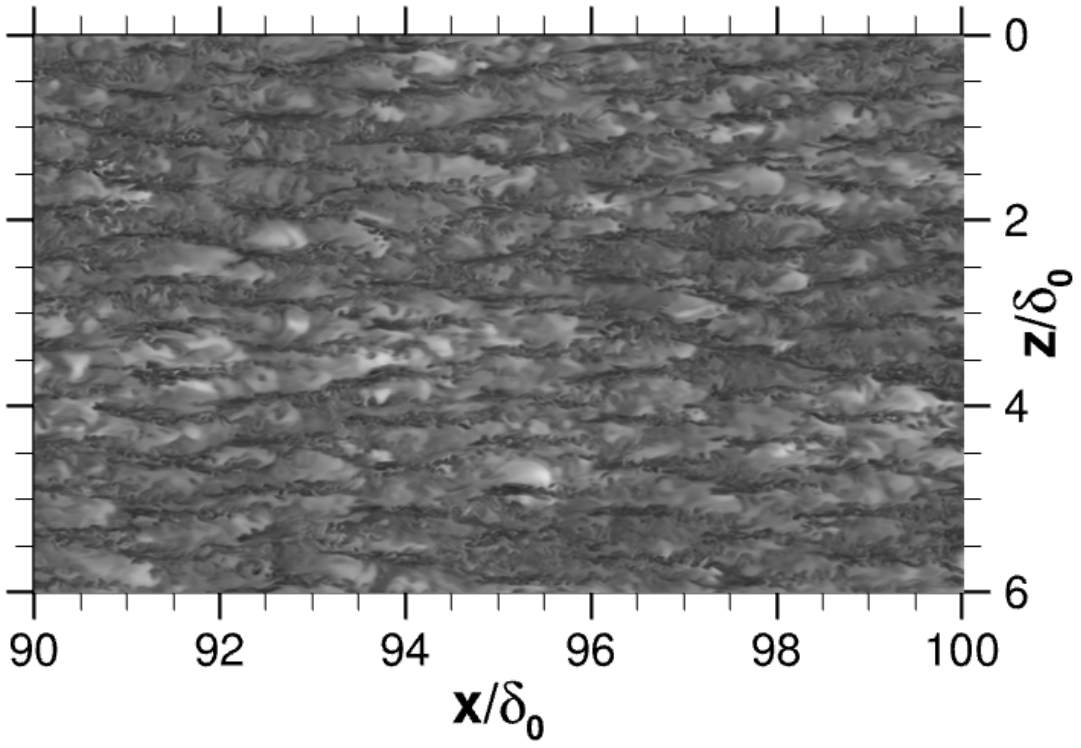

(d) Wavy Plane $y^+ = 55$, $y/\delta = 0.015$

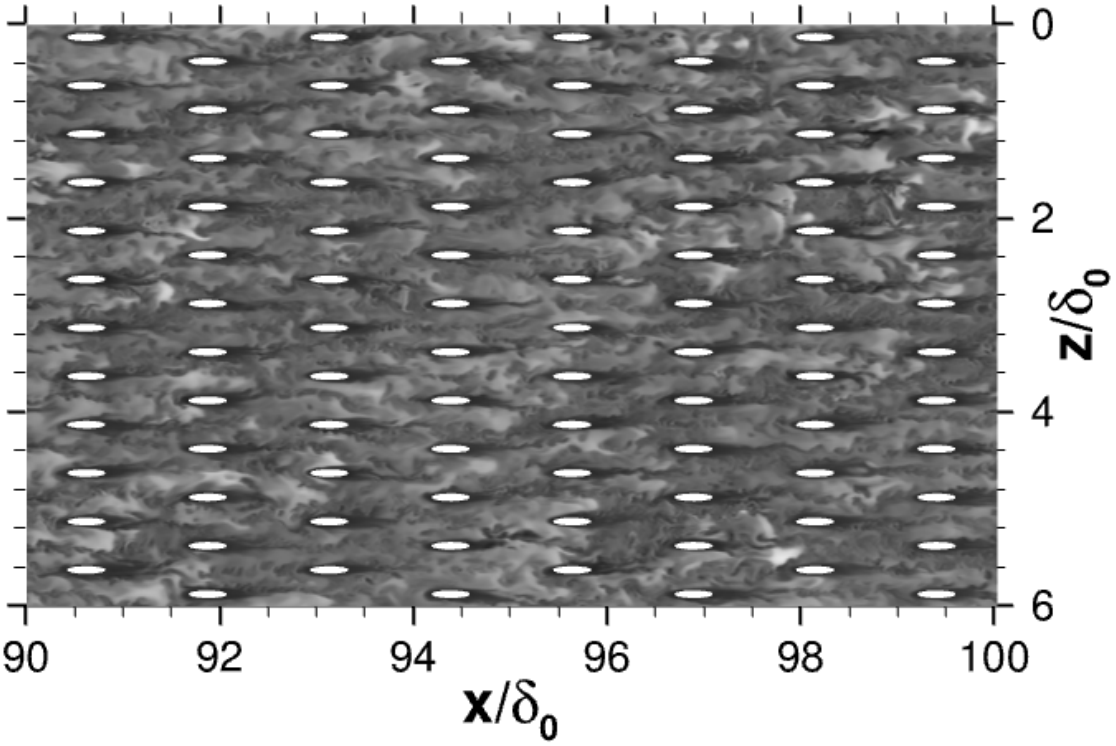

(e) $y^+ = 80$, $y/\delta = 0.021$

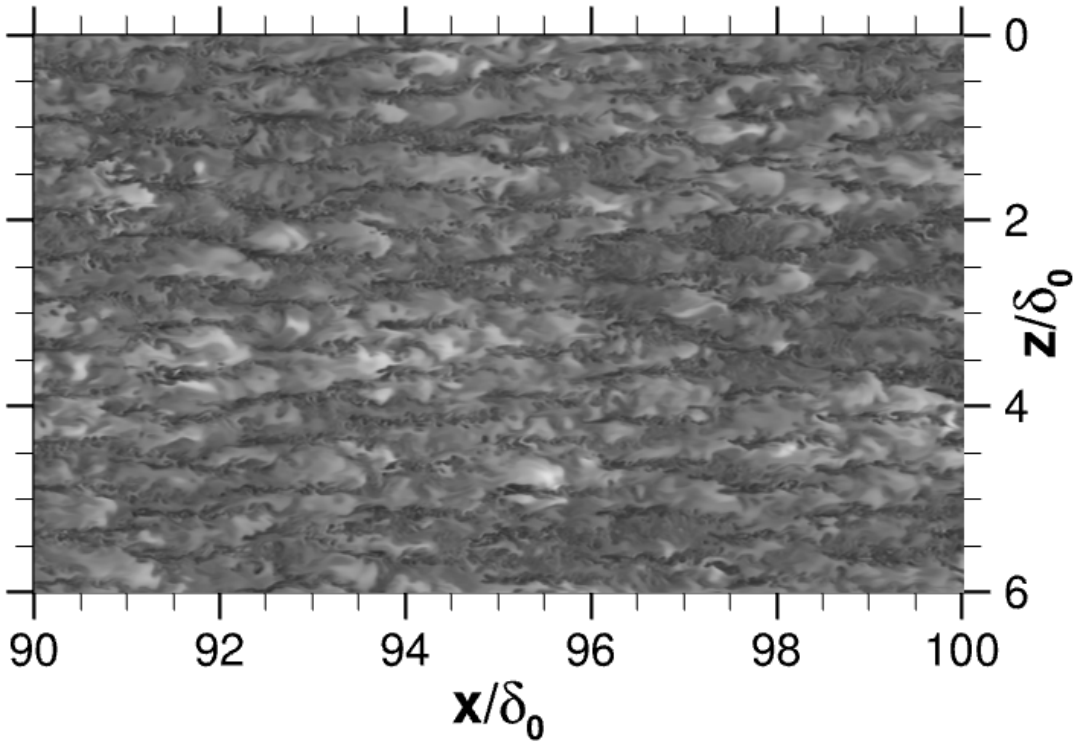

(f) Wavy Plane $y^+ = 80$, $y/\delta = 0.021$

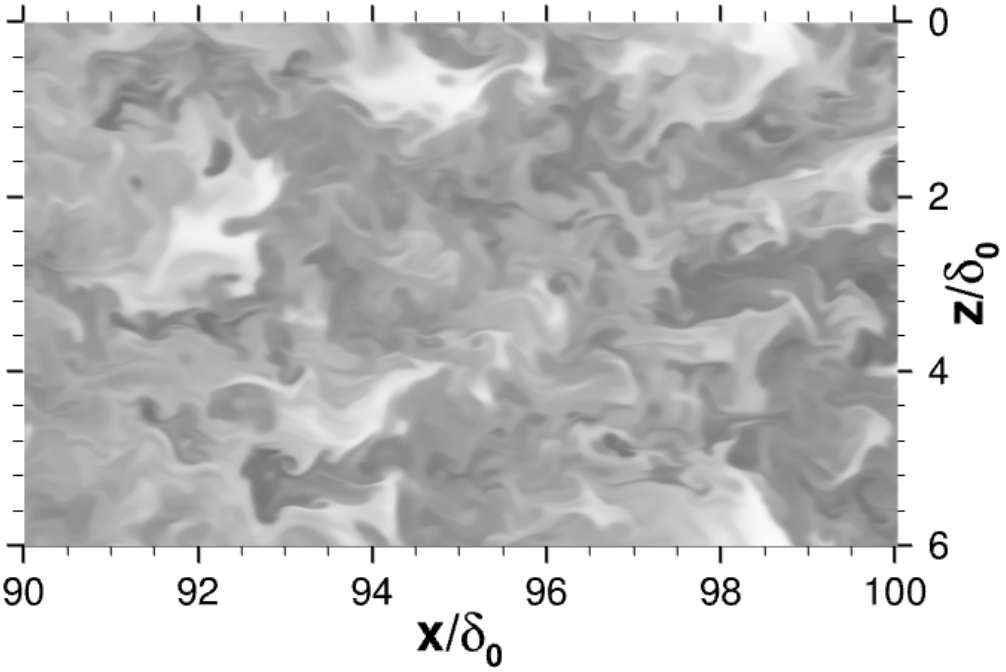

(g) $y^+ = 1100$, $y/\delta = 0.3$

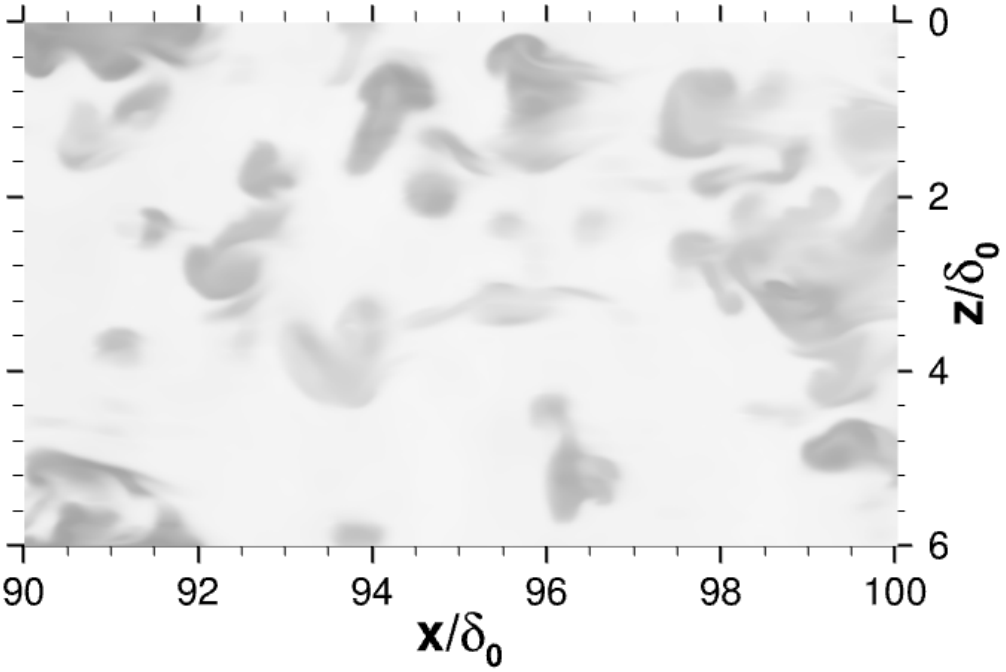

(h) $y^+ = 3480$, $y/\delta = 0.95$

Figure 3.11. Slices at various wall-normal locations of case R1, with the location described in inner unit [(a),(b),(c)] and outer units [(d),(e)]. Contours are of density normalized by freestream density.

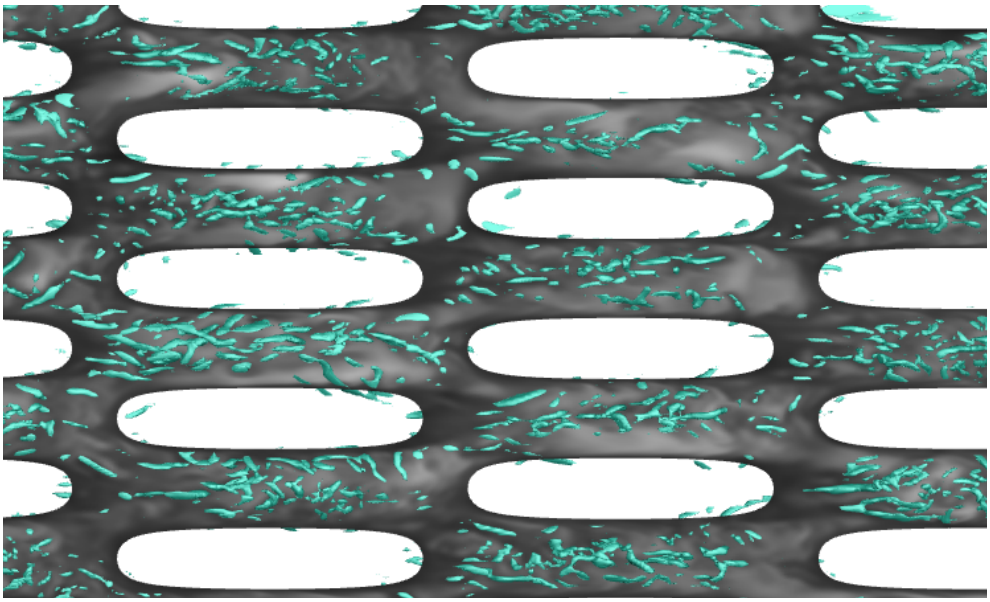

(a)

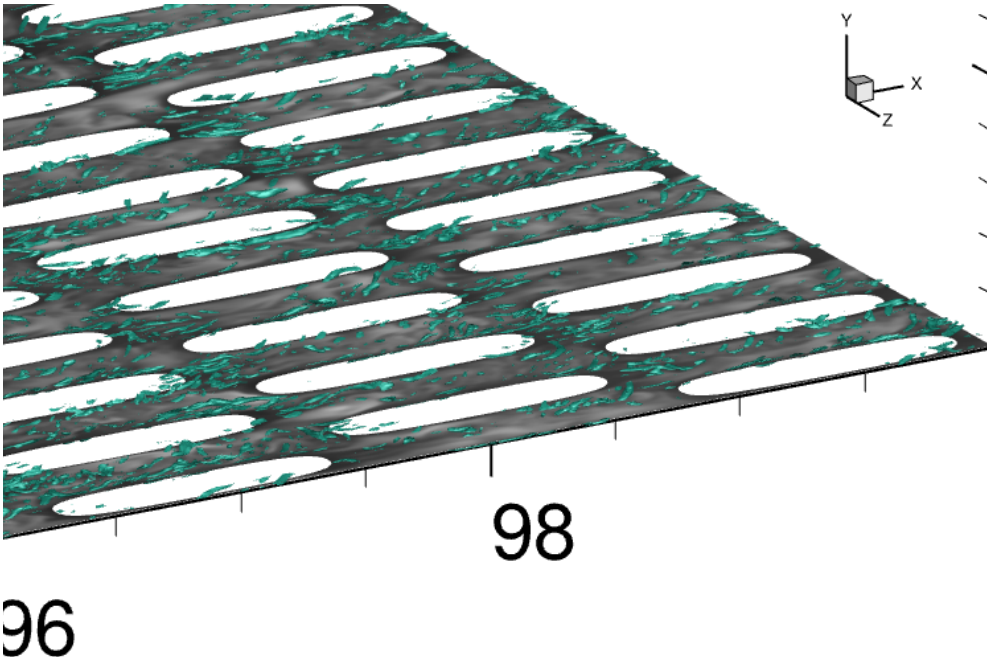

(b)

Figure 3.12. Two views of density contours at $y^+ = 18$ with isosurfaces of q-criterion = 100.

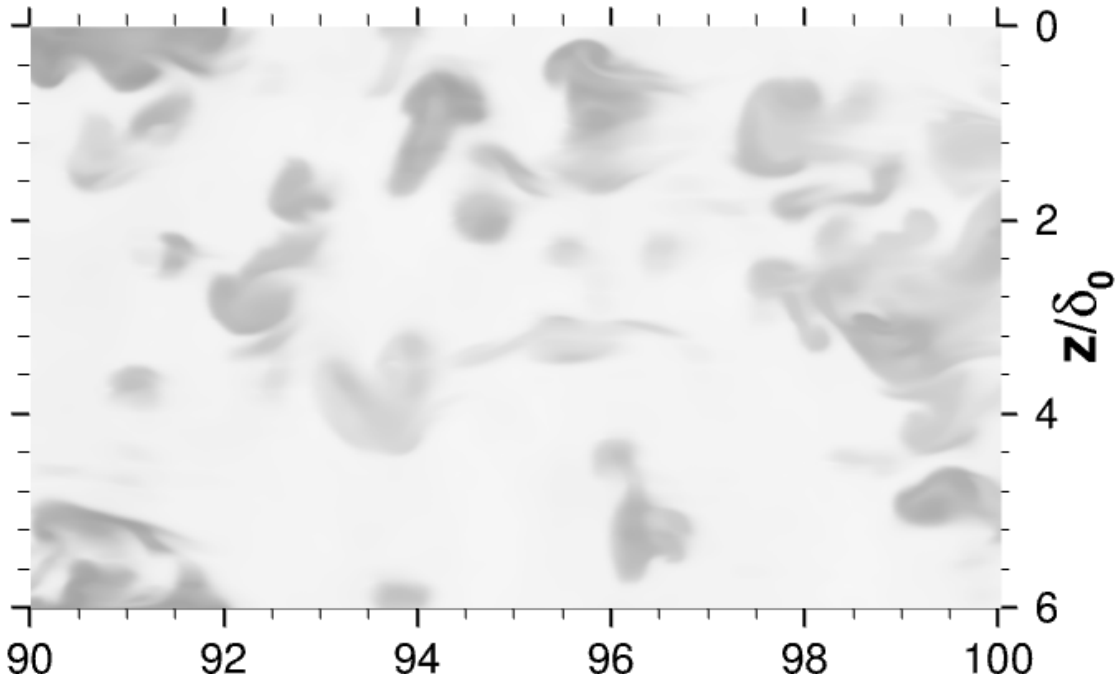

(a)

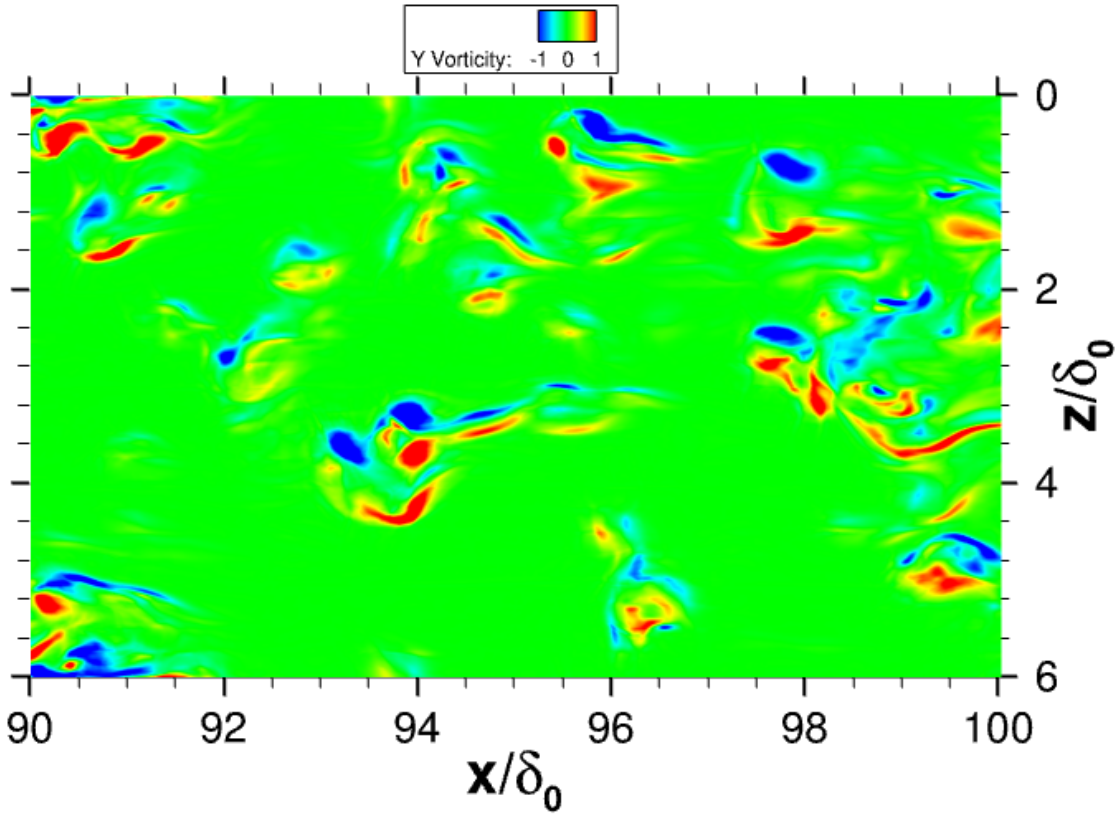

(b)

Figure 3.13. Slices taken at $y/\delta_0 = 0.95$ with a contour of density (a) and y-vorticity (b).

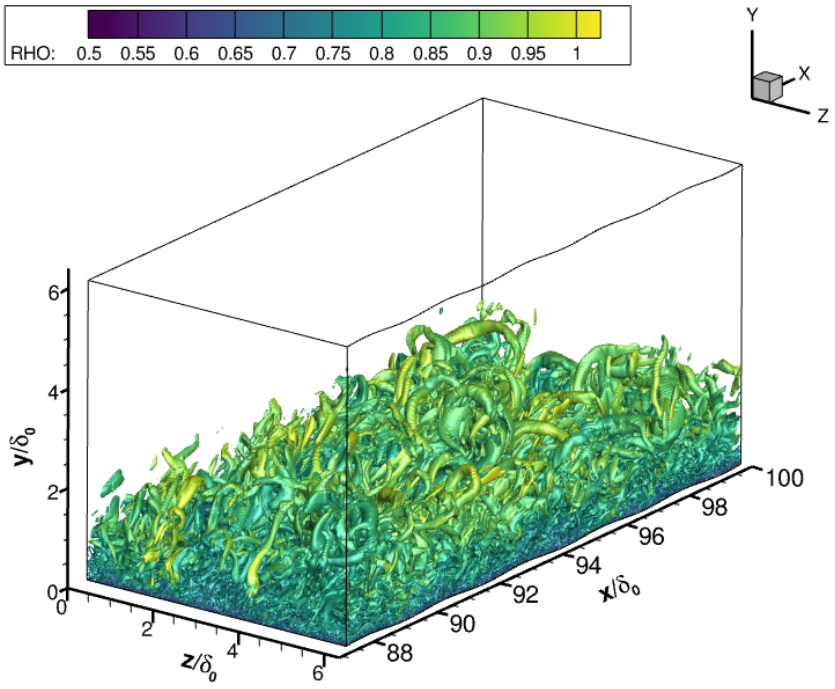

Figure 3.14. Isometric view of a block at the domain with isosurfaces of q-criterion = 0.15 and contours of density for case R1.

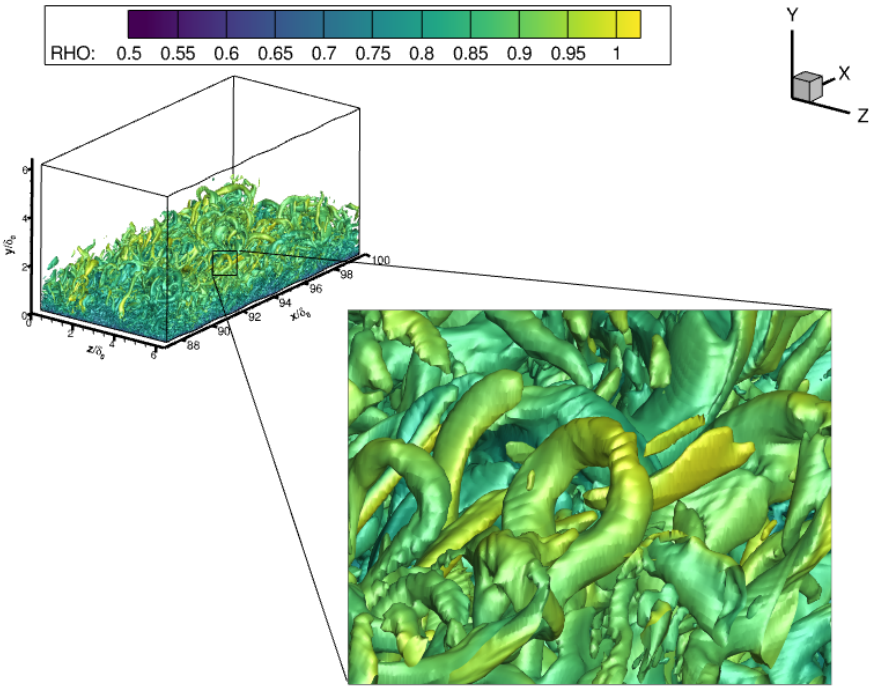

Figure 3.15. Magnified view of a horseshoe vortex seen in case R1. Isosurfaces of q-criterion = 0.15 and contours of density.

Case R2

This subsection will investigate the smaller roughness case (Case R2) in the same visual manner as the last two cases.

Figure 3.16 shows a comparison of the x-y plane between Case R2 and the smooth wall case. There is no clear discernible difference between the delta scale structures of the flows. Case R2 may show more uniform thickness of the boundary layer, but it is difficult to draw any conclusions based on one snapshot in time.

Figure 3.17 shows a magnified view of the two boundary layers for better comparison of the smaller structures. As seen with Case R1, there is a clustering of small structures in the valleys of the roughness elements.

Slices taken at y locations for Case R2 are presented in Figure 3.18. At $y^+ = 18$ a streaking pattern is seen and streaks of higher density fluid about as wide as the gap between the roughness elements can be seen. The narrow streaks of low density fluid seen in the smooth wall case are not seen in the plane cutting through the roughness elements, but are seen better in the wavy plane in Figure 3.18b. The streaks show a bit more coherence as they are arranged by the presence of the roughness elements. As in Case R1, an attempt to view the vortices typically associated with the low speed streaks is made using isosurfaces of Q-criterion. These surfaces can be seen in Figure 3.19. In Figure 3.19a the vortices seem to show some coherence with the streaks of dark low-speed fluid. This is more easily seen than Case R1 in Figure 3.12a. An isometric view of the vortices in Figure 3.12b show that the vortices have less vertical components than Case R1. This is expected since the roughness elements in Case R2 are lower in amplitude than Case R1.

The slice seen in Figure 3.18c shows the location of a secondary peak of streamwise Reynolds stress for Case R2. Here a pattern of streaks can be seen of wide high-speed streaks on the order of the width of the gap between the roughness elements. The roughness elements also act as sources of low-speed fluid in this mixing process. The wavy plane shows pattern similar to the smooth wall case. This is similar to what was seen in Case R1. Figure 3.18e shows a slice at $y^+ = 80$. There appears to be return to behavior of the baseline smooth case, but upon closer inspection, some effects of the presence of the roughness is

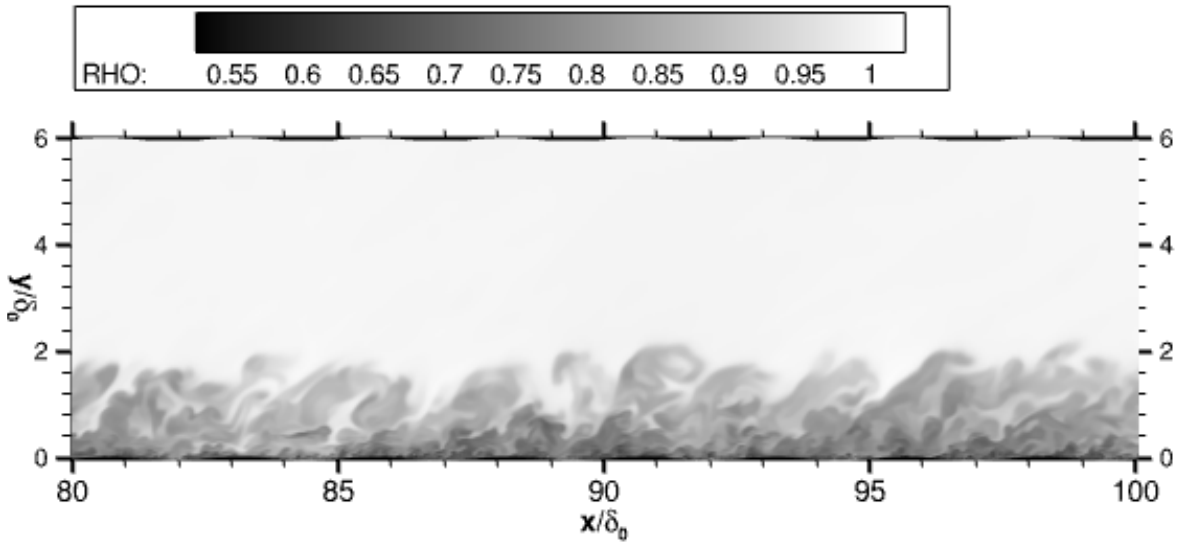

(a) Case R2

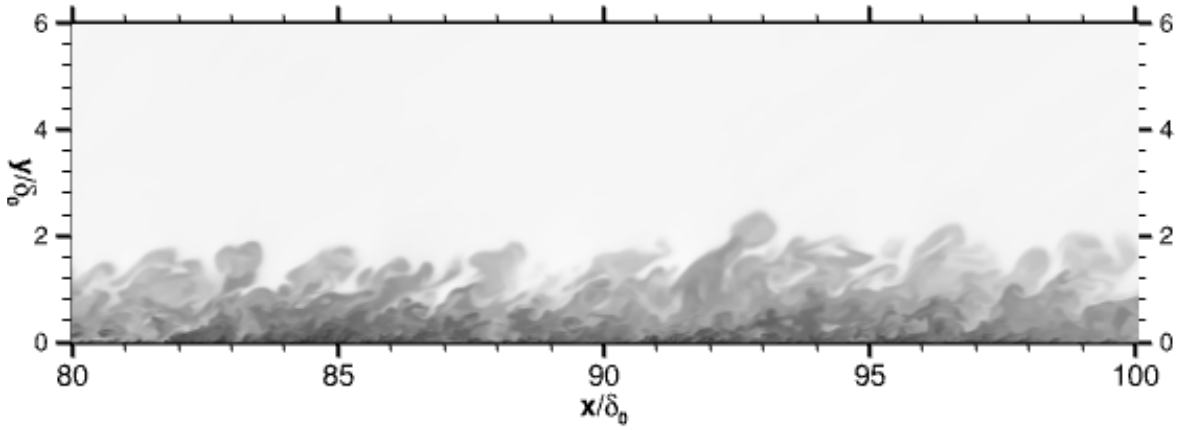

(b) Smooth Wall

Figure 3.16. Comparison of the delta scale structures of the R2 (a) and smooth wall (b) cases. Contours are of density normalized by the freestream density.

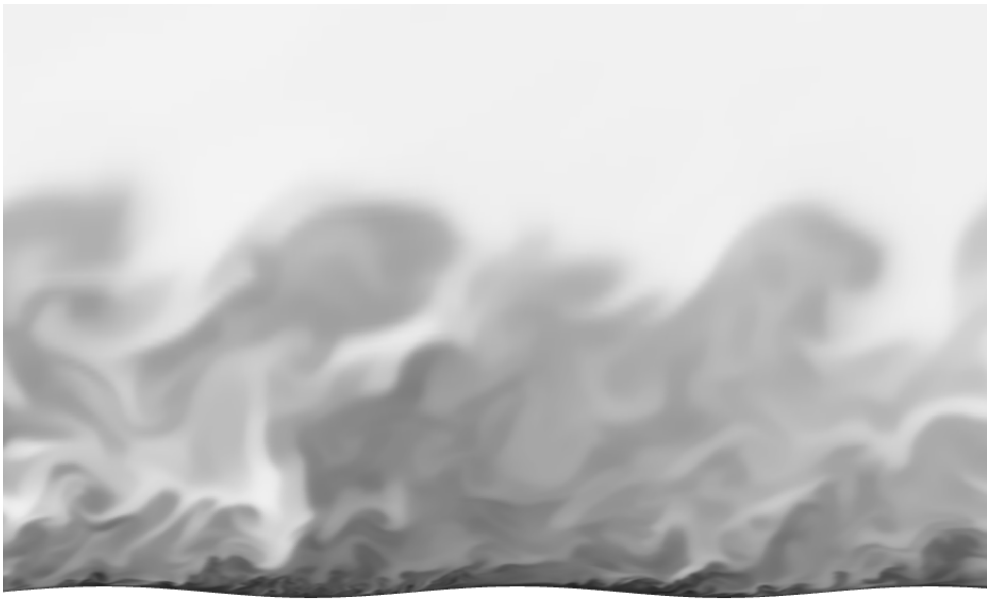

(a) Case R2

(b) Smooth Wall

Figure 3.17. Comparison of the near wall structures for the R2 (a) and smooth wall (b) cases. Contours are of density normalized by the freestream density.

still seen. Low-speed streaks can be seen spaced in an organized manner identical to how the roughness elements are spaced. The wavy plane in Figure 3.11f shows less disturbance from the roughness elements. Further up in the boundary layer of Case R2 at $y/\delta = 0.3$, there seems to be no distinction between the other cases. Some of the similar mushroom structures can be seen (see $x/\delta_0 = 98.5$,$z/\delta_0 = 0.75$). At the edge of the boundary layer at $y/\delta = 0.95$ in Figure 3.18h, there is no apparent distinction between Case R2 and the other cases. Some similar structures are seen between the cases.

To inspect the edge of the boundary layer in a manner similar to the other cases, the y-vorticity is plotted as a contour in comparison to the density contour. The comparison can be seen in Figure 3.20. Again, there appears to be pairing of opposite sign vortices. As stated for the previous cases, these are most likely slices through horseshoe or hairpin vortices.

To investigate the three-dimensional structure of the boundary layer, isosurfaces of q-criterion are shown for a block at the end of the domain in Figure 3.21. For the 3-D δ-scale structures of the boundary layer, there is no clear distinction between the cases. There are still many horseshoe vortices in this flow. A magnified view of a horseshoe vortex is seen in Figure 3.22.

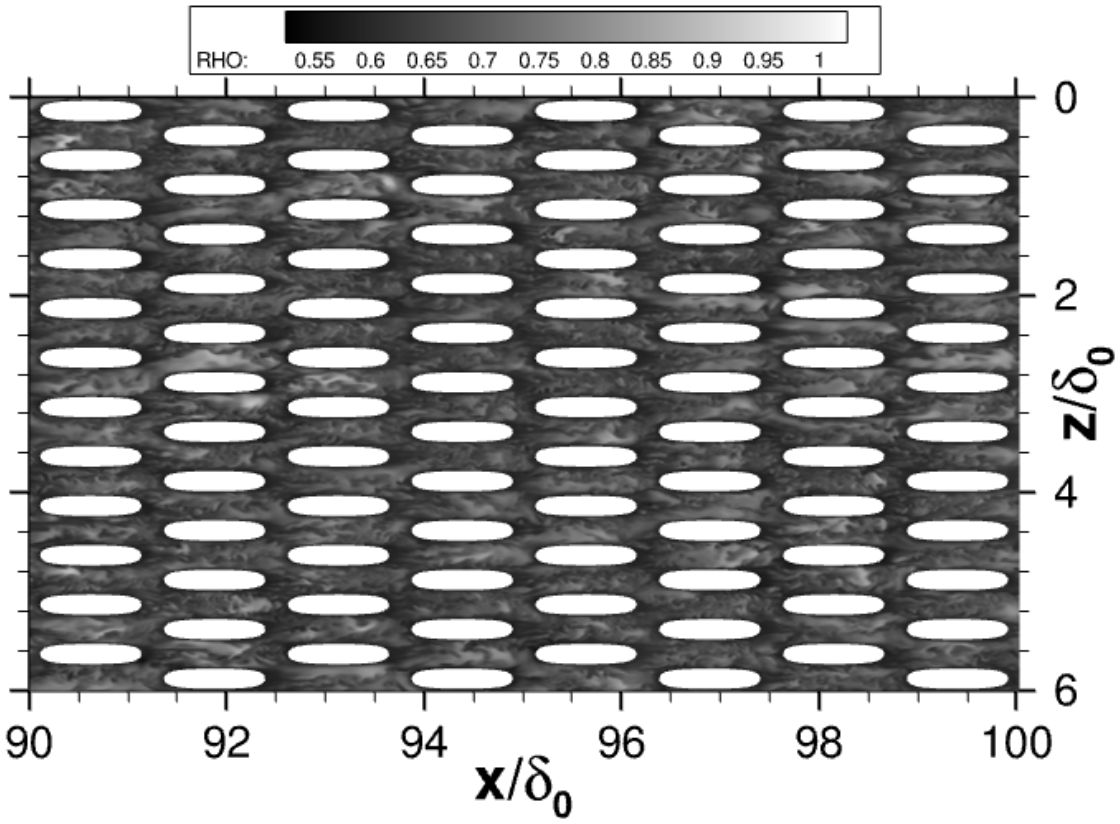

(a) $y^+ = 18$, $y/\delta = 0.005$

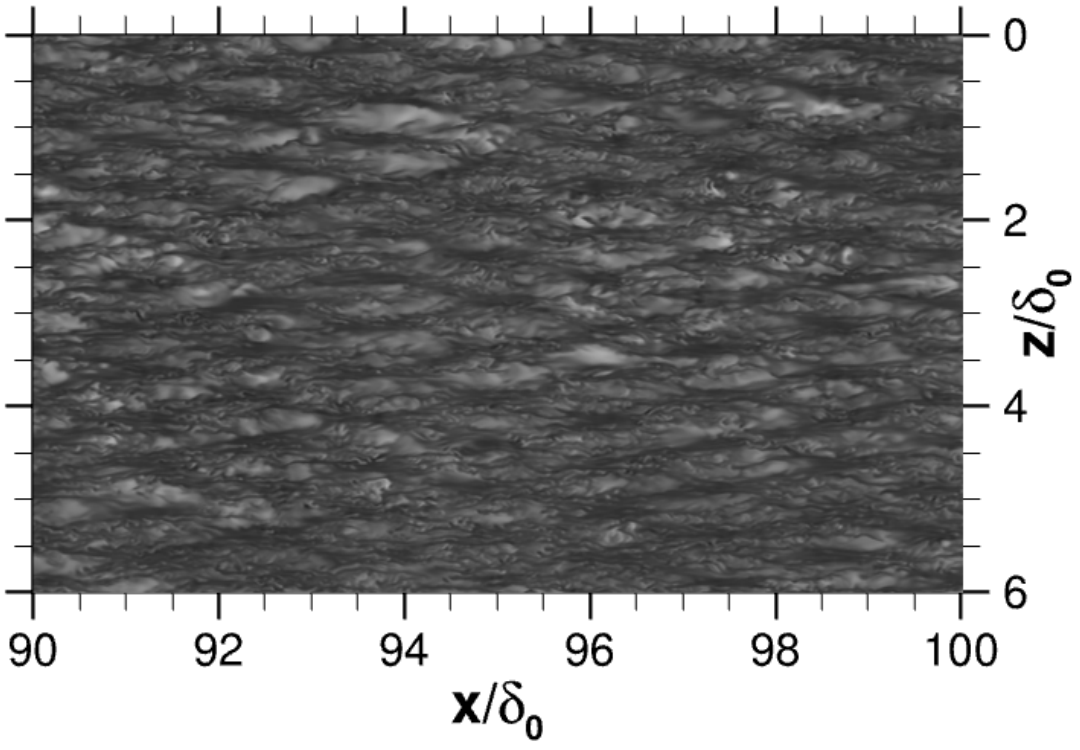

(b) Wavy Plane $y^+ = 18$, $y/\delta = 0.005$

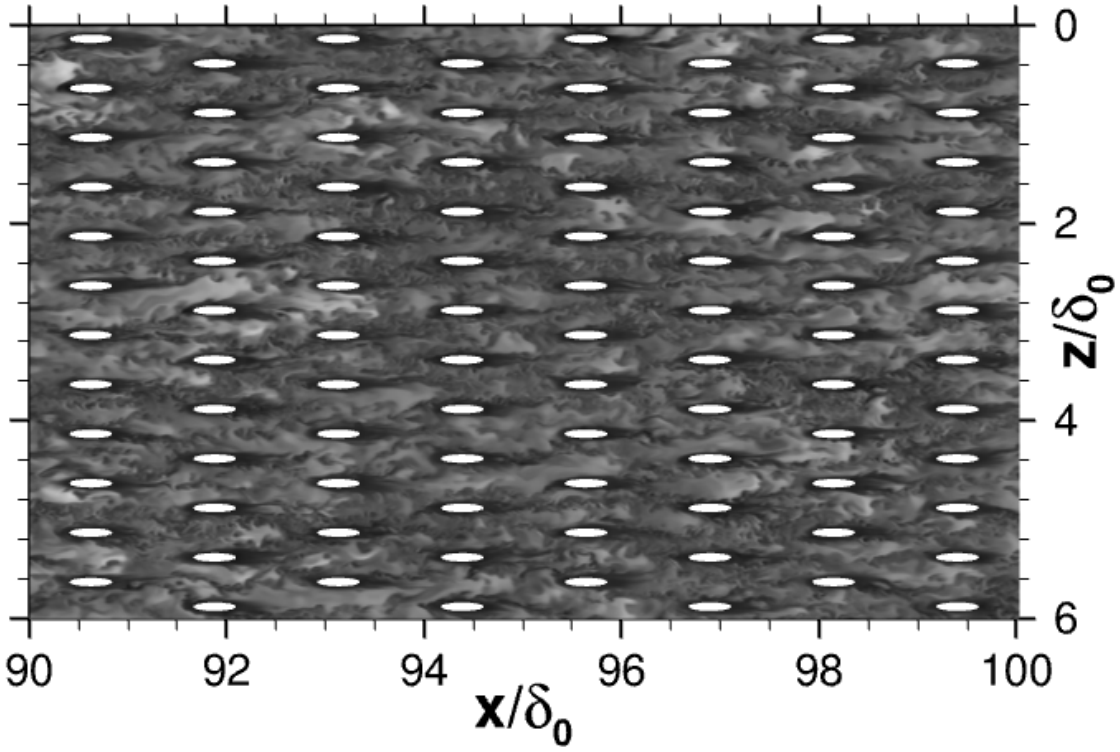

(c) $y^+ = 55$, $y/\delta = 0.015$

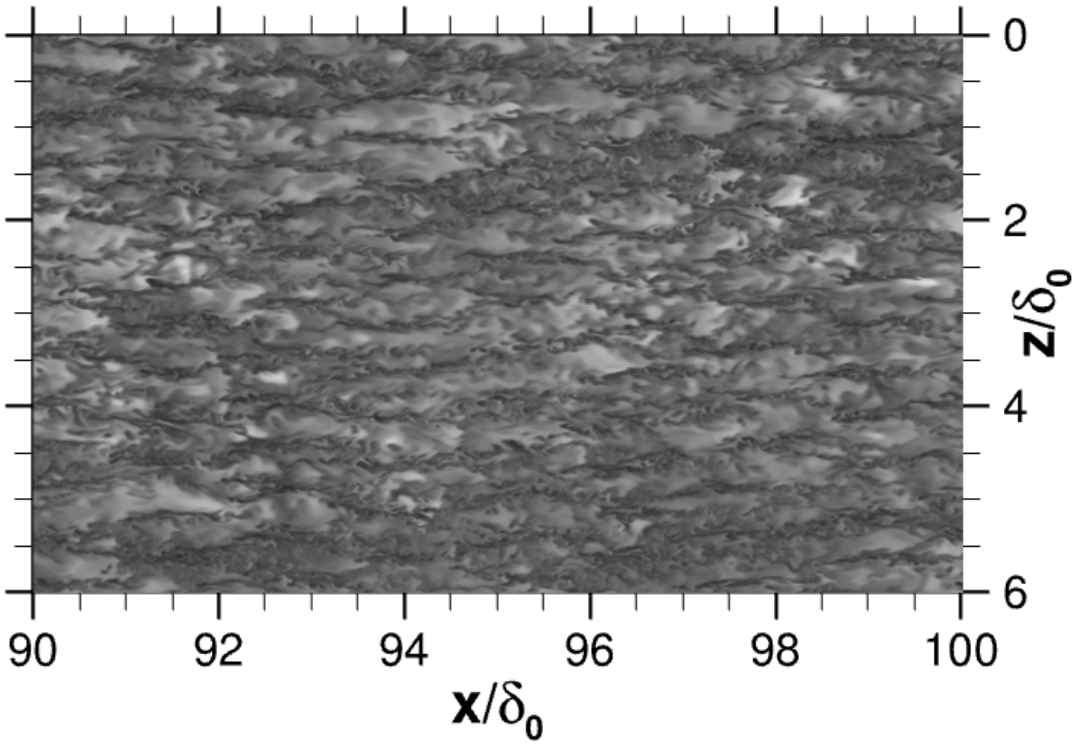

(d) Wavy Plane $y^+ = 55$, $y/\delta = 0.015$

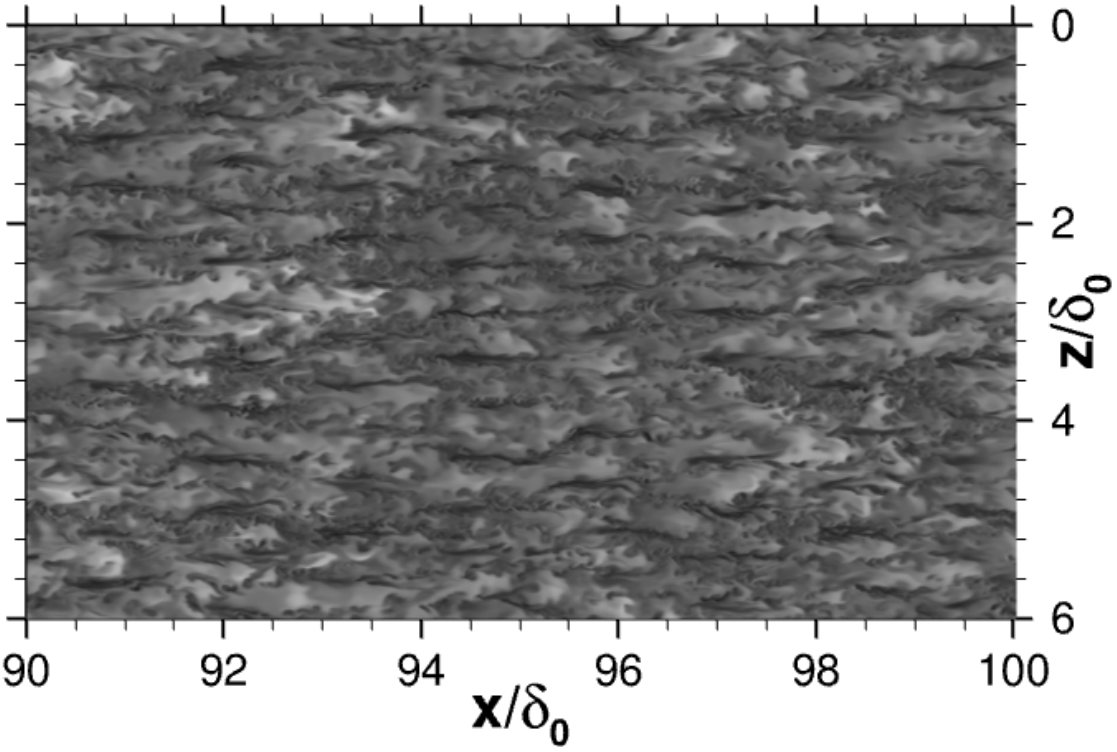

(e) $y^+ = 80$, $y/\delta = 0.021$

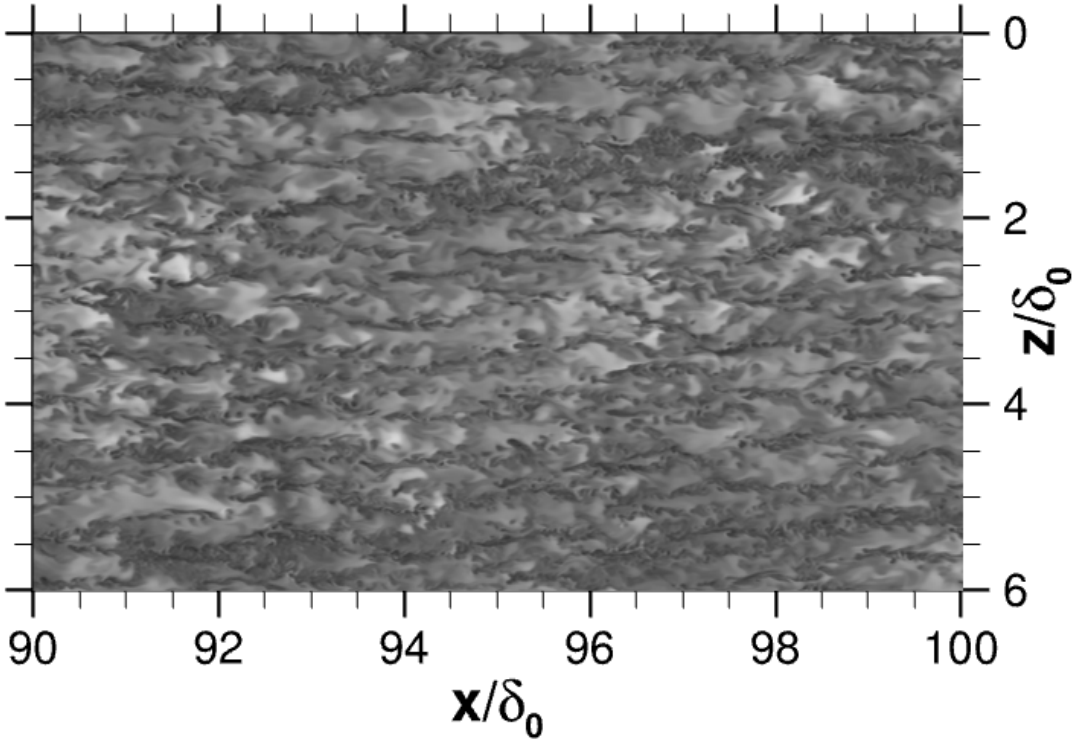

(f) Wavy Plane $y^+ = 80$, $y/\delta = 0.021$

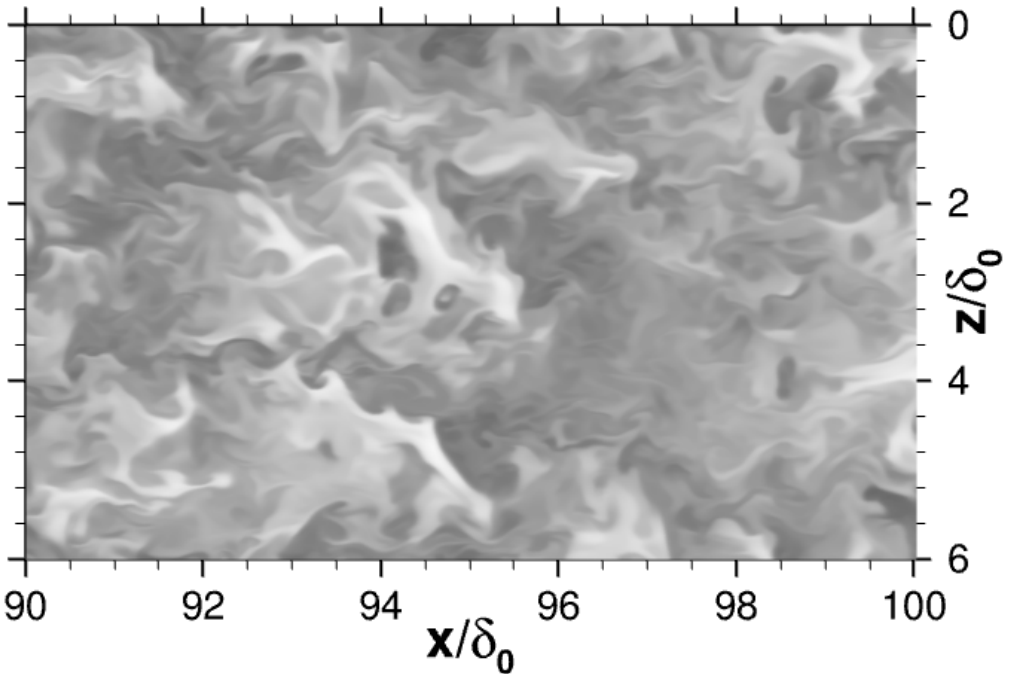

(g) $y^+ = 1100$, $y/\delta = 0.3$

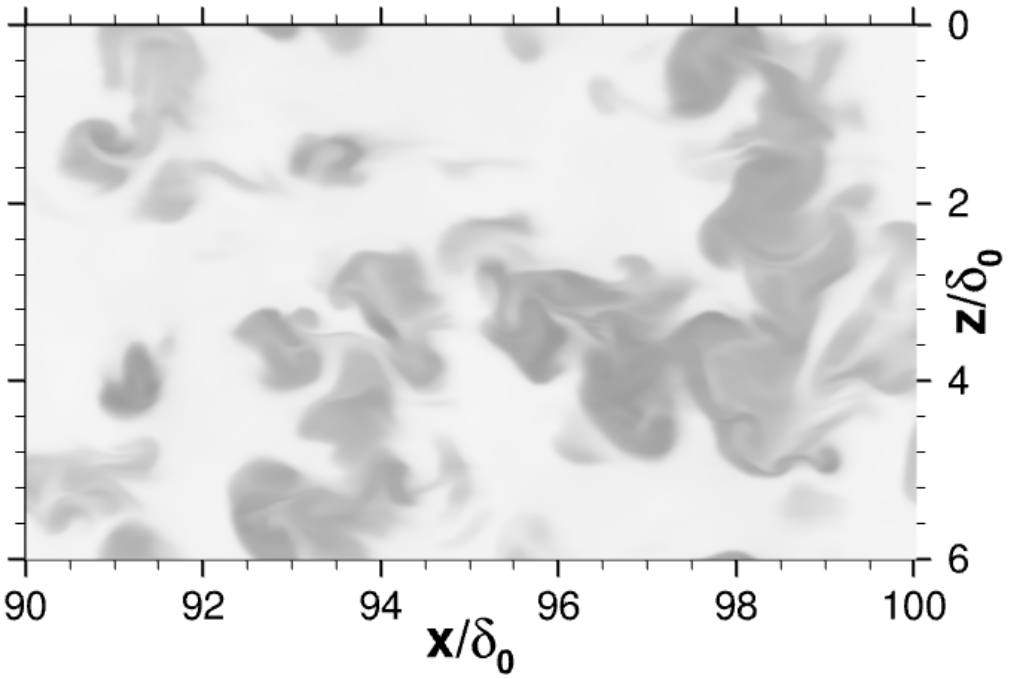

(h) $y^+ = 3480$, $y/\delta = 0.95$

Figure 3.18. Slices at various wall-normal locations of case R2, with the location described in inner unit [(a),(b),(c)] and outer units[(d),(e)]. Contours are of density normalized by freestream density.

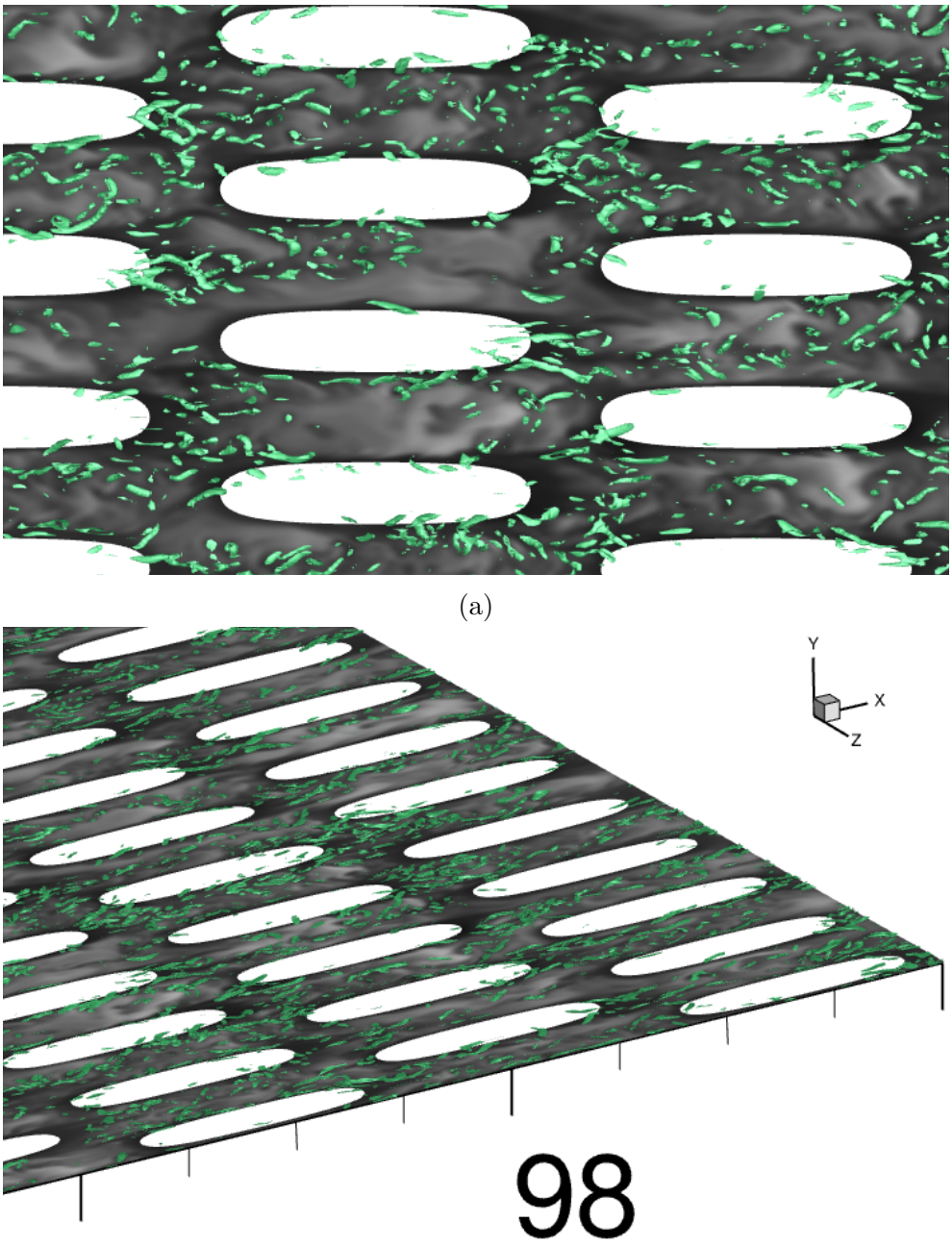

(a)

(b)

Figure 3.19. Two views of density contours at $y^+ = 18$ with isosurfaces of q-criterion = 100 for Case R2.

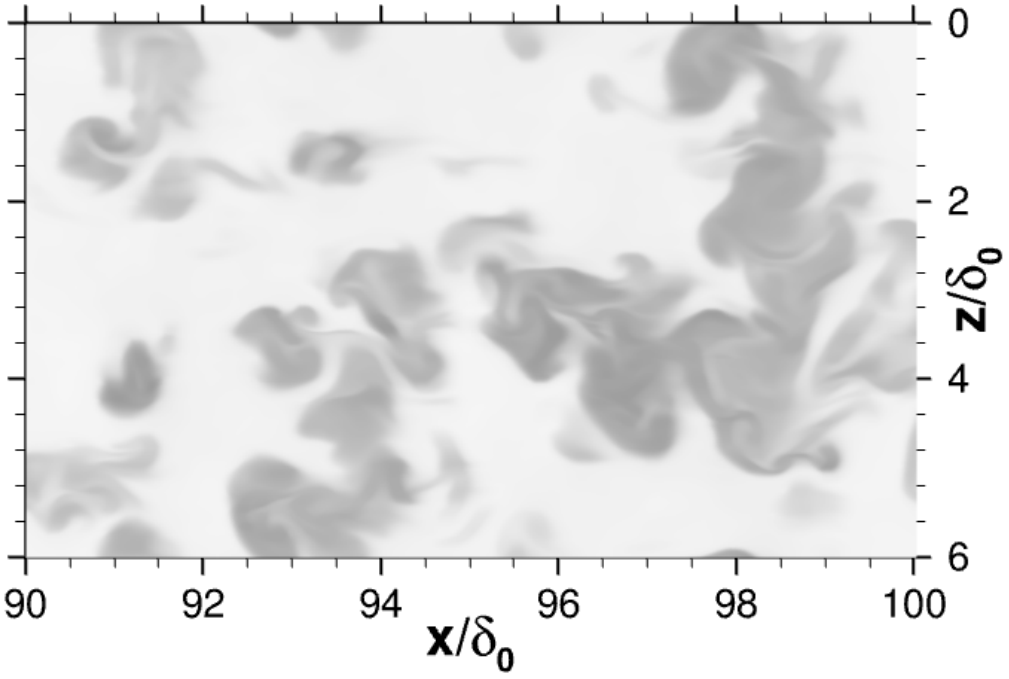

(a)

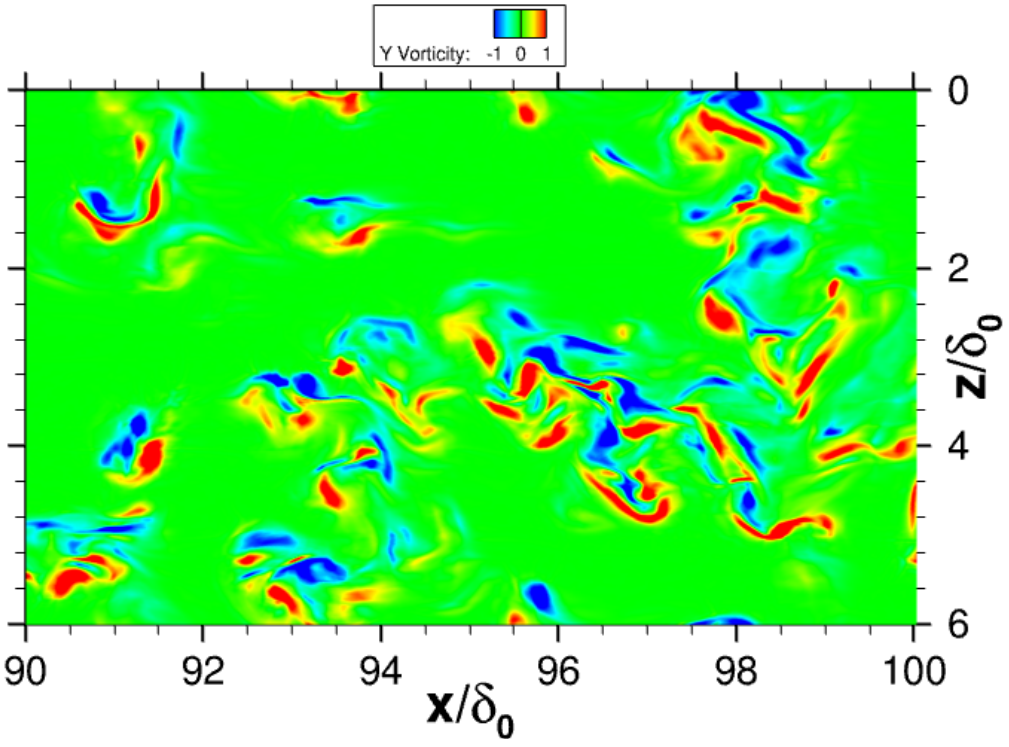

(b)

Figure 3.20. Slices taken at $y/\delta_0 = 0.95$ with a contour of density (a) and y-vorticity (b) in Case R2.

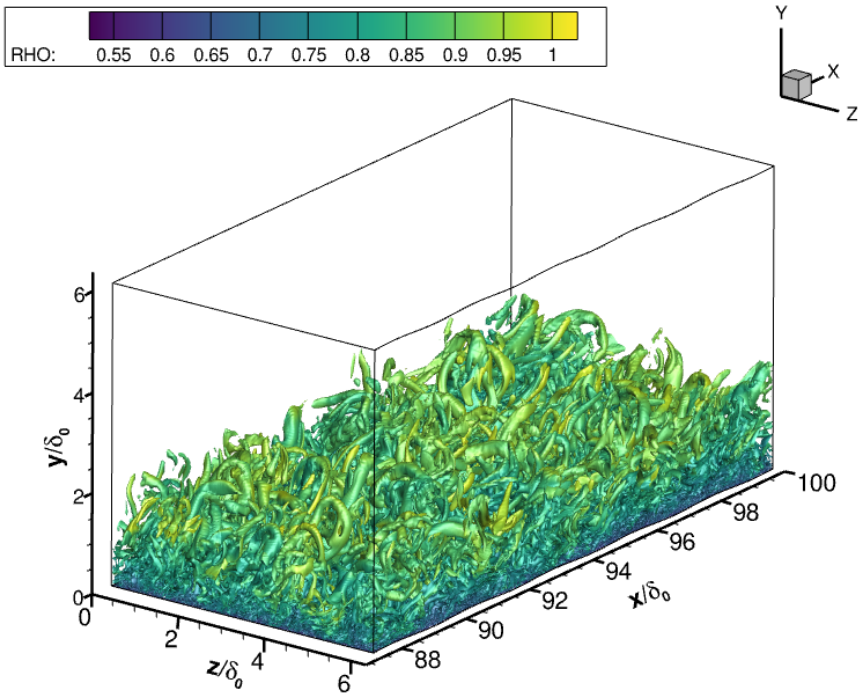

Figure 3.21. Isometric view of a block at the domain with isosurfaces of q-criterion = 0.15 and contours of density for Case R2.

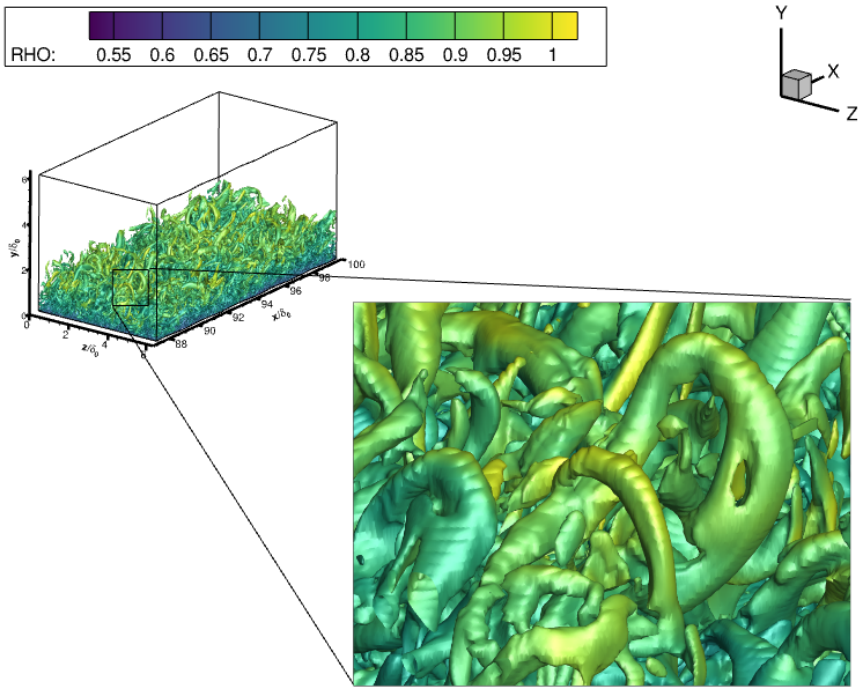

Figure 3.22. Magnified view of a horseshoe vortex seen in Case R2. Isosurfaces of q-criterion = 0.15 and contours of density.

3.2 Statistical Descriptions of Flow

The prior section dealt with analyzing the flowfields visually and discerning any differences between the cases. While this is useful for witnessing coherent structures in the flow (thus bringing some order to the apparent randomness of turbulence), statistics are a way to describe flowfields in a quantitative way. Statistics are helpful in the development of turbulence models. Statistical approaches may also aid in understanding the phenomena witnessed in visualization of the flow.

This section will first investigate the use of the Morkovin's scaling [51] for compressible flows so that its use in this study can be substantiated. Also relevant to scaling are the values of the skin friction coefficient (C_f), and the method used to calculate the skin friction is discussed. After discussions regarding the scaling, the grid resolution will be reported along with different inner scaled quantities of interest. The mean profiles of velocity and Reynolds stresses will be analyzed, followed by discussions of turbulent kinetic energy (TKE). To complement the visualized planes of the previous section, probability density functions (PDF) of density are calculated for the same wall-normal planes investigated earlier. Finally, heat transfer will be briefly discussed.

3.2.1 Scaling of Compressible Turbulent Boundary Layers

The scaling of incompressible boundary layers is done with the assumption that density does not vary significantly in the flow (by definition of incompressible). For compressible boundary layers, the scaling typically needs to account for variable density in the flow. For the mean velocity in inner coordinates, the Van Driest transformation [52] is typically used and will be used for this study. The Van Driest transformation is given by

$$u^+_{VD} = \int_0^{u^+} (\bar{\rho}/\rho_w)^{1/2}\, du^+. \tag{3.1}$$

For the Reynolds stresses and other statistics, the Morkovin [51] scaling is used which is defined by a modified friction velocity. Morkovin's hypothesis was that compressibility effects on turbulence fluctuations are only important for high Mach number flows (M>5) and

that compressible boundary layer data can be scaled by using a modified friction velocity. The modified value is defined by

$$\left(\frac{\overline{\rho_w}}{\bar{\rho}}\right)^{1/2} u_\tau. \tag{3.2}$$

To account for density variations, an alternative approach to Reynolds averaging is Favre or mass-weighted averaging. As discussed in section 1.1, Reynolds averaging is a way to decompose fluctuating and mean values of quantities of interest. The approach to Reynolds averaging typically involves assuming density does not vary. Favre-Averaging does not make this assumption. A Favre decomposition of some quantity is

$$f = \tilde{f} + f'' \tag{3.3}$$

where f is an instantaneous quantity, $\tilde{f}$ is the Favre average $(\overline{\rho f}/\overline{\rho})$, and f'' is the fluctuating component. The fluctuating component is related to the fluctuating component of the Reynolds decomposed fluctuating component by $f'' = f' - \overline{\rho f'}/\overline{\rho}$. To investigate the use of Morkovin scaled Reynolds stresses in place of the Favre-averaged Reynolds stresses, the values of the Reynolds stress $(\overline{u'u'}/u_\tau^2)$, the Morkovin scaled Reynolds stress $(\overline{\rho}(\overline{u'^2})/(\overline{\rho_w}u_\tau^2))$, and the Favre-averaged Reynolds stress $(\overline{\rho u''u''}/(\overline{\rho_w}u_\tau^2))$ were calculated from the smooth wall case and plotted in Figure 3.23.

There is a clear difference between the Reynolds Stress and the Favre averaged Reynolds stress, indicating that there are compressible effects that need to be accounted for. The Morkovin scaling shows a nice collapse of the Reynolds stress onto the Favre averaged stress. Moving forward it is assumed that Morkovin scaling to account for compressibility effects is appropriate. This is generally assumed to be acceptable for low turbulent Mach numbers defined as

$$M_t = \sqrt{2\overline{k}}/\sqrt{\gamma R\overline{T}} \tag{3.4}$$

where $\overline{k}$ is the turbulent kinetic energy, γ is the ratio of specific heats ($\gamma = 1.4$), R is the specific gas constant ($287\frac{J}{kgK}$), and $\overline{T}$ is the mean temperature. This can be thought of as the

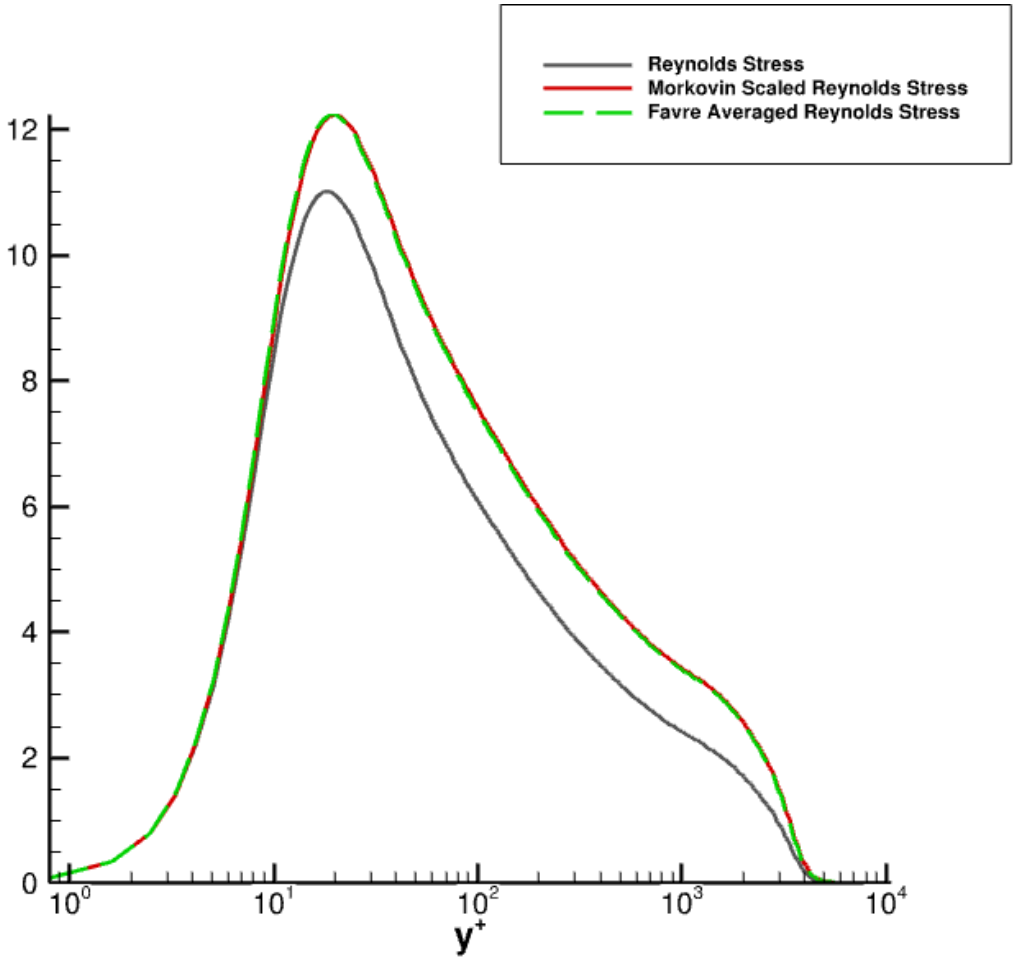

Figure 3.23. Comparison of Reynolds stress, Morkovin scaled Reynolds stress, and Favre averaged Reynolds stress. The component of the stress chosen was streamwise.

root mean square speed of turbulent fluctuations compared to the speed of sound (thus the name turbulent Mach number). High Mach number flows will typically have high turbulent Mach number values as well if the flow is turbulent, and if the turbulent Mach number is high then there will be complex compressibility effects involving the turbulent fluctuations. Shocks will form from the turbulent fluctuations which are near or exceeding the local speed of sound. Since the mean temperature and turbulent kinetic energy is variable through the boundary layer, the value of M_t was calculated as a profile and is shown in Figure 3.24. The peak value of M_t is located at $y^+ = 20$ which could be expected since this is typically described as the buffer region with active turbulent fluctuations. The peak value

is approximately 0.21, which shows the turbulent fluctuations are not a significant enough fraction of the local speed of sound to see large compressibility effects in the turbulent fluctuations. This is consistent with what is seen in Figure 3.23 since a large turbulent Mach number would likely show differences between the Favre-averaged Reynolds stress and the Morkovin scaled Reynolds stress. The turbulent Mach number should be equal to zero on the surface of the no-slip condition, since the fluctuations are zero. The plot does not show this behavior on the semi-log scale. Plotted in a linear axis, the turbulent Mach number goes to zero.

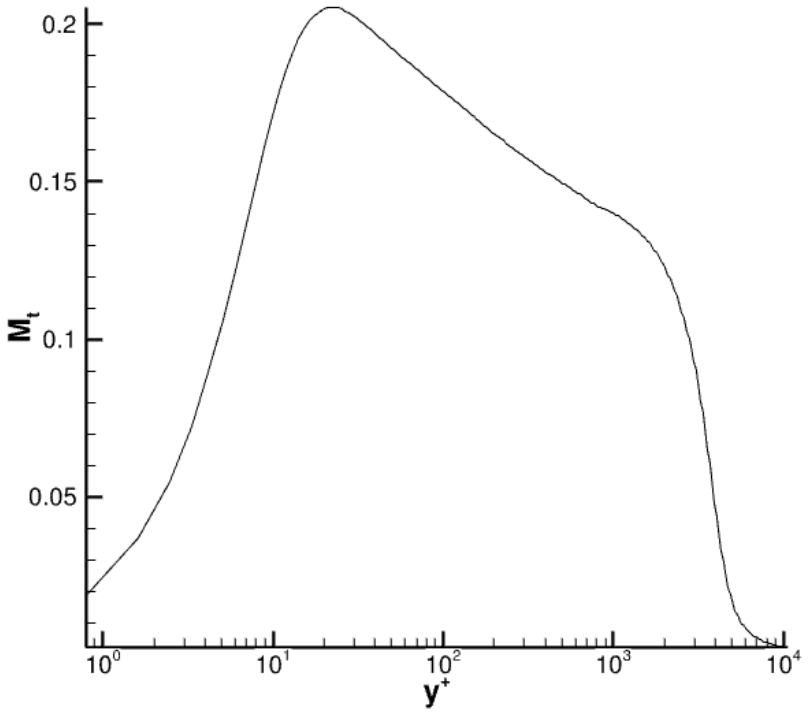

Figure 3.24. The value of the turbulent Mach number (M_t) throughout the boundary layer. Peak value is approximately $M_t = 0.21$.

To investigate how the Morkovin scaling can affect the friction velocity through the boundary layer, the friction velocity unscaled and Morkovin scaled are plotted and shown together in Figure 3.25. The scaling causes the value of the friction velocity to change about 22% from the wall to the boundary layer edge. This is a significant deviation. Differences

between the two plots near the wall is most likely due to the difference between the calculated average wall temperature, and the nominal wall temperature calculated using the ideal gas law, the surface pressure, and temperature.

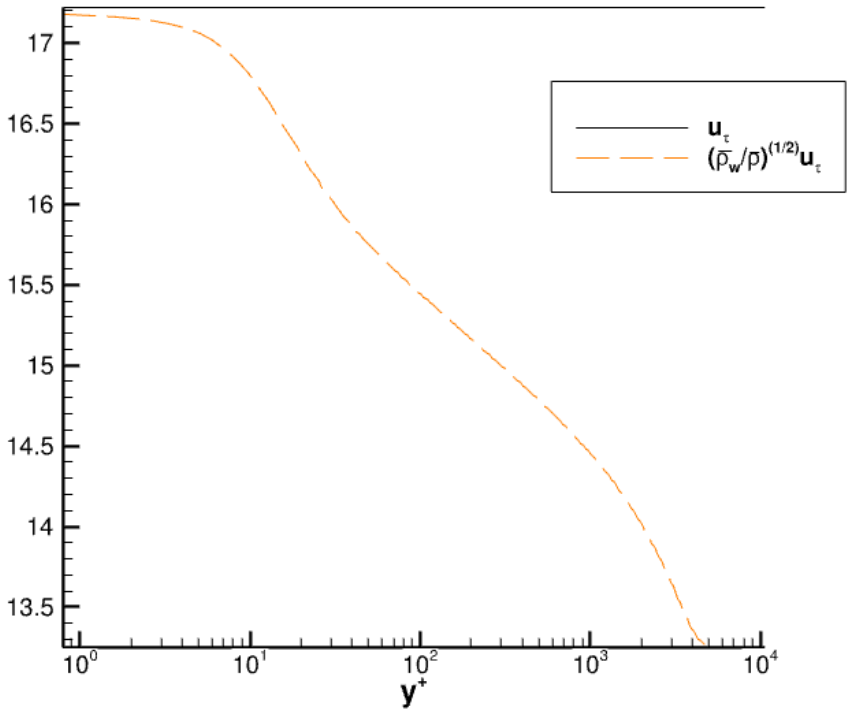

Figure 3.25. The value of the friction velocity (u_τ) unscaled and Morkovin scaled. The percent difference between the wall and the edge of the boundary layer is approximately 22%.

3.2.2 The Value of Skin Friction

Now that the scaling of the friction velocity has been determined, another question is how exactly to determine the friction velocity. The friction velocity is determined by

$$\left(\frac{\tau_w}{\rho_w}\right)^{\left(\frac{1}{2}\right)}. \tag{3.5}$$

The density (ρ_w) can be determined directly from calculations and is usually easily determined in experiments as well. The wall shear stress (τ_w) is more difficult to determine. A

commonly used method to determine the friction velocity is the Clauser chart method [53]. This method assumes a universal logarithmic region in the mean velocity profile represented in Equation 1.15. Multiplying the log law equation by u_τ/u_∞ results in

$$\frac{u(y)}{u_\infty} = \frac{1}{\kappa}\frac{u_\tau}{u_\infty} ln\left(\frac{yu_\infty}{\nu}\right) + \frac{1}{\kappa}\frac{u_\tau}{u_\infty} ln\left(\frac{u_\tau}{u_\infty}\right) + B\frac{u_\tau}{u_\infty}. \tag{3.6}$$

The coefficient of friction is equivalent to

$$C_f = 2(u_\tau/u_\infty)^2. \tag{3.7}$$

This allows equation 3.6 to be rewritten as

$$\frac{u(y)}{u_\infty} = \frac{1}{\kappa}\sqrt{\frac{C_f}{2}} ln\left(\frac{yu_\infty}{\nu}\right) + \frac{1}{\kappa}\sqrt{\frac{C_f}{2}} ln\left(\sqrt{\frac{C_f}{2}}\right) + B\sqrt{\frac{C_f}{2}}. \tag{3.8}$$

Equation 3.8 represents a family of lines that can determine C_f by plotting the values of $u(y)/u_\infty$ and seeing which values of C_f best approximates the collected data [54]. Compressible studies use a similar method that begins with the Van Driest II correction of the mean velocity profile [55]. The method used exactly was derived by Ekoto et al. [38]. Peltier et al. [39] estimate that the error associated with this method may be as high as 10%.

For numerical simulations, much more data is available to attempt to directly calculate the wall shear stress. For the smooth wall case, the calculations are simple since the only drag is from viscous forces. The wall shear stress can be calculated using

$$\tau_w = \mu\frac{\partial u}{\partial y}. \tag{3.9}$$

For the rough wall cases, it was found that using equation 3.9 was not sufficient because it did not account for the form drag of the roughness elements. It is worth noting that the programs used to calculate the viscous shear stress of the wall also account for the variation of the surface in the rough cases, so equation 3.9 does not represent those scenarios. Grid metrics are used to compute the components of stress on the surface. To account for the extra terms from form drag, the surface traction vectors were integrated to give a total force per unit area of the rough wall cases. The average viscous force per unit area of the wall as

well as the form drag force per unit area were added to give the total C_f. This is a useful approach because the calculations for viscous and form drag are calculated separately, and allows investigations into the primary drag forces on the wall. The C_f from viscous and form drag components, as well as the total C_f are shown in Table 3.1. It can be seen that drag from the roughness elements is on an order of magnitude less than the viscous drag on the surface. This suggests that the rough flows cannot be classified as the fully rough regime, since the viscous sublayer is still present and contributing a majority of the drag forces on the surface. This flow should be classified as transitionally rough. Transitionally rough surfaces can have a wide range of effects on the flow depending on the surface geometry.

Table 3.1. Coefficient of friction for each case and the associated components of visous and form drag.

Case	C_f viscous	C_f form	C_f total
Smooth Wall	1.376×10^{-3}	0.0	1.376×10^{-3}
R1	1.356×10^{-3}	1.047×10^{-4}	1.461×10^{-3}
R2	1.371×10^{-3}	4.924×10^{-5}	1.420×10^{-3}

3.2.3 Grid Resolution

For simulations which solve the Navier-Stokes equations directly via direct numerical simulation (DNS) or implicit large-eddy simulation (ILES), the resolution of the grid used in the calculations can be analyzed by scaling the distance between points (Δ) in inner units. Inner units are used since the smallest scales of the flow which need to be resolved are typically near the wall, where inner units are the commonly used scaling. Since the values of C_f can be used to determine u_τ, we can analyze the resolution of the grid in inner units.

Georgiadis et al. [56] recommends a range of values for ILES and DNS and can be seen in Table 3.2. Poggie et al. [41] performed another series of computational experiments and found that for DNS the recommendation is for $\Delta y_w^+ < 1$ and $\Delta x^+, \Delta z^+ \leq 10$ for convergence of statistics characterizing large-scale flow features. The recommended resolution for the nondimensional time step (Δt^+) is less than 1.0.

Table 3.2. Recommended resolution by Georgiadis et al. [56]

ILES	$50 \leq \Delta x^+ \leq 150$	$\Delta y_w^+ < 1$	$15 \leq \Delta z^+ \leq 40$
DNS	$10 \leq \Delta x^+ \leq 20$	$\Delta y_w^+ < 1$	$5 \leq \Delta z^+ \leq 10$

The grid resolution for each case was calculated. The values are shown in Table 3.3. The subscript "e" represents the value at the edge of the boundary layer. There is less literature on a sufficient value of resolution at the edge of the boundary layer. Small values in inner units may be desired to capture the effects of the viscous superlayer, the region where irrotational freestream fluid meets rotational boundary layer fluid. The comparison of the largest cell spacing to the boundary layer thickness may also be an effective way to measure the resolution. The resolution of each case in Table 3.3 shows that the cases can most likely be categorized as an ILES on the more resolved side of the scale. The values in inner units are close to the maximum recommendations from Georgiadis et al. for DNS. They are roughly half the resolution recommended by Poggie et al. for DNS.

Table 3.3. Grid resolution of each case

Case	Δx^+	Δy_w^+	Δz^+	Δy_e^+	$\Delta y_e/\delta$	Δt^+
Smooth Wall	22.1	0.797	17.1	90.2	2.4 %	0.300
R1	22.8	0.365	17.7	111.0	2.8%	0.312
R2	22.5	0.360	17.4	109.0	2.8 %	0.311

3.2.4 Reynolds numbers and Characterizing Roughness

When describing the height of roughness elements, its often useful to report the value of the roughness height in inner units (k^+) also known as the roughness Reynolds number. Here the height of the roughness used is the peak to trough values (R_z in Table 2.4). It should be noted that k^+ should not be confused with k_s^+ which is the inner scaled equivalent sand grain roughness height. Some studies have used the two interchangeably which could be misleading since the equivalent sand grain roughness height is not necessarily comparable to the roughness height. The value of the Reynolds number δ^+ defines the separation of scales between the flow and is also of interest. The ratio of the roughness height to the boundary

layer thickness is a practical value as well since it defines how much of the boundary layer is blocked by the roughness elements. The values of these parameters are seen in Table 3.4.

Table 3.4. Reynolds numbers , δ/δ_0, k/δ

Case	k^+	δ^+	$Re_{\theta i}$	δ/δ_0	k/δ
Smooth Wall	0	3800	14,900	2.147	0.0
R1	182.5	3974	15,600	2.177	0.046
R2	126.0	3902	15,200	2.168	0.032

The experiment from Kocher et al. [36] used k^+ and δ^+ to discern if the flow was in the fully rough regime. The guidelines they state is if $k^+ > 70$ and $\delta^+ > 3000$, then the flow is in the fully rough regime. The roughness from the current study meets these criterion, however the flow is not in the fully rough regime. The flow is not in the fully rough regime because the viscous drag is the primary drag on the surface as opposed to form drag from the roughness elements. The fully rough regime is defined as a regime of flow where the roughness destroys the viscous sublayer and the friction factor becomes independent of the Reynolds number. It may be worth mentioning again that the value of k^+ may be used a bit erroneously as it is typically k_s^+ that defines a fully rough regime.

Table 3.4 also shows the value of the nondimensional boundary layer thickness (δ/δ_0). There are slight differences in the boundary layer thickness caused by the presence of the roughness elements. Case R2 has slightly shorter roughness elements and a smaller value of δ.

Shown in Table 3.4 is the value of the incompressible momentum thickness Reynolds number ($Re_{\theta i}$). The incompressible transformation [48] for the momentum thickness Reynolds number is given by

$$Re_{\theta i} = (\mu_\infty/\overline{\mu}_w)Re_\theta. \tag{3.10}$$

The value of Re_θ is calculated with freestream values of viscosity and density and is approximately $23,500$ in this study. The values are seen to be fairly high for DNS and ILES simulations at the time of writing.

Since the flow of the simulations is not in the fully rough regime, it is not possible to derive the equivalent sand grain roughness using conventional means of hydrodynamic tests,

since being in the fully rough regime is a requirement to determine the equivalent sand grain roughness. However, for the sake of curiosity, the equivalent sand grain roughness will be calculated using Equation 1.19. Equation 1.19 relates geometric properties of the surface to k_s. The calculated values for Case R1 and Case R2 are respectively 0.157 and 0.109. These values are on the order of the roughness height measured peak to trough (0.100 and 0.070 respectively). This could be expected since the type of roughness could be classified as "k-type" roughness where the elements are spaced far enough apart that there is no recirculation between the elements. K-type rough surfaces have equivalent sand grain roughness heights roughly equivalent to the dimensional height of the roughness elements [3]. These values of k_s in inner units (k_s^+) are 286.5 for Case R1, and 196.2 for Case R2. Using Equation 1.20, the value of C_f can be determined for flow in the fully rough regime. Here the values calculated for Case R1 and R2 are 9.4×10^{-3} and 8.4×10^{-3} respectively. These values are about an order of magnitude off from the actual calculated values of the study. This could be expected since equation 1.20 was deduced using data from fully rough flows, and the simulations are transitionally rough.

3.2.5 Mean Profiles

The mean profiles of the flow are now investigated. In rough wall flows, the inner-scaled mean velocity profile is of particular interest due to the roughness function (Δu^+) being a way to categorize a rough surface. A comparison between the cases and values collected from the UTSI experiment [36] are shown in Figure 3.26. Each roughness case sees a downward shift in the mean velocity profile which is categorized by the roughness function (Δu^+). There is a clear difference between the mean profiles of the simulations compared to the experiments. This could be due to several factors. A primary factor is that the simulated boundary layer could still be developing significantly and would need a longer computational domain to develop further. Inner scaled velocity profiles which lie well above the log-law region are indicative of a turbulent flow which is not fully developed. The additive constants seen in Table 3.5 are higher than values typically expected, which suggests the profiles are shifted up from the log-law region. The UTSI experiment also scaled using a friction velocity

determined using the clauser chart method of the Van Driest transformed velocities. The simulations directly calculated the friction velocity and plotted the Van Driest transformed velocities scaled with the Morkovin scaled friction velocity. There is possibly a difference in scaling. The experiments also show greater values of the roughness functions, which could be due to the nature of the roughness topology causing the flow to be in the fully rough regime. Kocher et al. [36] also found that the value of Δu^+ continued to increase (leading to a greater downward shift of the profiles) with streamwise development of the boundary layer. In the simulations the value of Δu^+ is 1.44 and 0.62 for Case R1 and Case R2 respectively. The expected behavior of a wavy wall is that the roughness function does not scale with the roughness heights. However, there is a clear impact of the roughness height on the roughness function in this case. This may suggest that the surface can be considered rough.

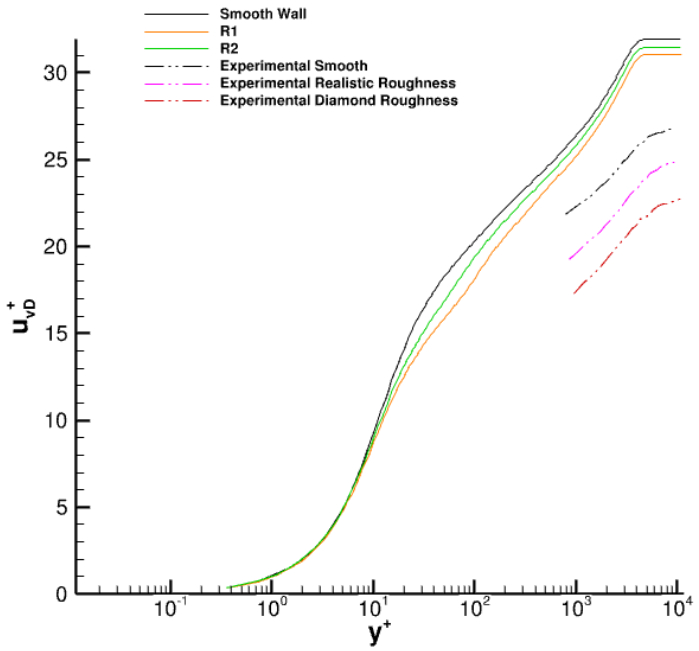

Figure 3.26. Van Driest transformed inner scaled mean velocity profiles. The downward shift in rough cases is called the roughness function Δu^+.

To investigate if there is a presence of a logarithmic region of the simulations, the diagnostic function as defined by Pirozzoli and Bernardini [48] is plotted as a function of y^+ in Figure 3.27. The diagnostic function is defined as

$$\Xi = y^+(\frac{\partial u^+_{VD}}{\partial y^+}). \tag{3.11}$$

A region of constant value would be indicative of a logarithmic behavior. For each case, there is region where logarithmic behavior can generally be claimed. There are secondary peaks in the rough cases which are associated with regions slightly above the tips of the roughness elements. For Case R1 the secondary peak is at $y^+ = 108$ and for Case R2 the secondary peak is at $y^+ = 77$. The peaks of the roughness elements are located at half the value of k^+ from Table 3.4 ($k^+ = 91$ and $k^+ = 63$ for Case R1 and Case R2 respectively). To calculate the constants from the log-law, the logarithmic region is taken to be $150 \leq y^+ \leq 875$ based on the range that appears logarithmic in Figure 3.27. From that range of values the calculated values of constants from the log-law are shown in Table 3.5.

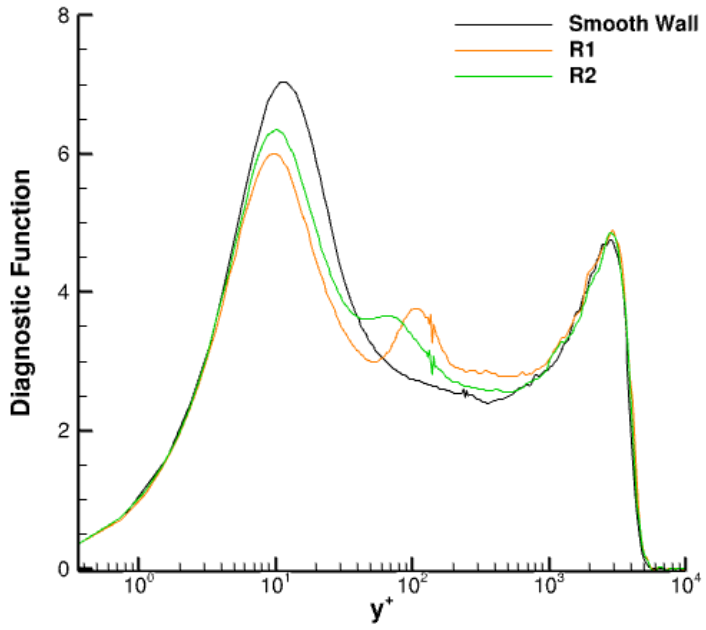

Figure 3.27. The diagnostic function (Ξ) value of each of the cases. A constant region would be indicative of logarithmic behavior.

Table 3.5. Log-law Constants

Case	κ	B
Smooth Wall	0.392	8.64
R1	0.347	5.29
R2	0.377	7.43

The values in Table 3.5 are similar to the universal constant typically used, but there is variation for each case. It is possible that the roughness elements disturb the logarithmic region enough that some of the logarithmic behavior is lost, but the constants for the rough cases do not show complete loss of logarithmic behavior. The additive constant for the smooth wall case is higher than the typical value of approximately 5. This could also suggest that the boundary layer is still undergoing significant growth. Jiménez et al. [3] hypothesized that disruption of the logarithmic region would lead to a loss of wall-similarity between rough and smooth cases. To investigate for the presence of wall similarity, it is useful to plot outer scaled velocity as well as defect velocities ($u_\infty - u$). Figure 3.28 shows the outer scaled velocity profiles as well as the defect velocity scaled in inner coordinates.

In Figure 3.28a, wall-similarity can be observed starting around $y/\delta = 0.6$. This is similar to what was found in the experiment by Kocher et al. [36]. In inner coordinates the defect velocity shows an interesting behavior where the profiles collapse before the logarithmic region and then separate significantly before rejoining around $y^+ = 1000$. This could be due to the presence of the roughness in the logarithmic region and the importance of the logarithmic region in turbulence generation.

The Reynolds stresses ($R_{ij} = \overline{u_i' u_j'}$) of each case are shown in Figure 3.29. There are clear distinctions between the cases in the inner region of the boundary layer where the dynamics are directly affected by the presence of the roughness elements. There appears to be a collapse of the Reynolds stress profiles beyond the logarithmic region ($y^+ > 1000$). However, recent compressible flow studies have found that the Reynolds stresses appear to shift compared to the smooth wall cases ([36] [39] [40]). To investigate if differences can be seen using the same scaling of the variables and axes, the Reynolds stresses were plotted again as a function of y/δ on linear axes to see if there is any apparent shift in the stresses that was concealed by the semi-log axes of Figure 3.29.

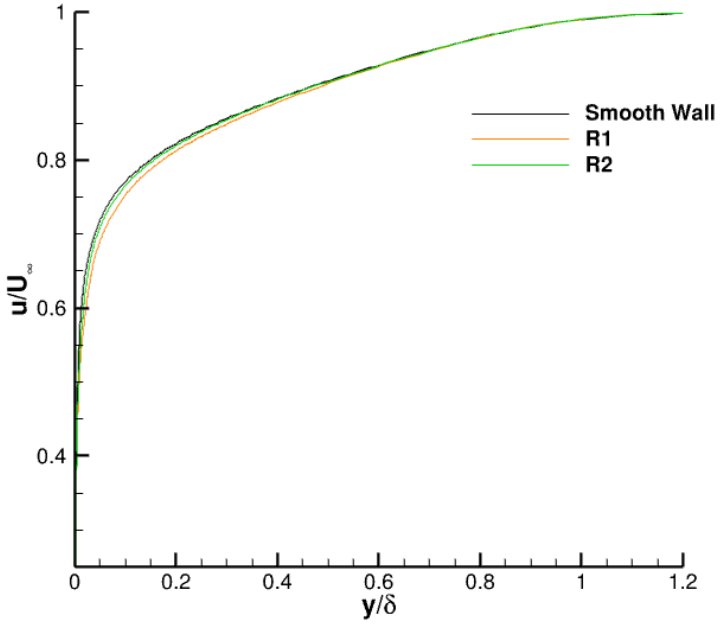

(a)

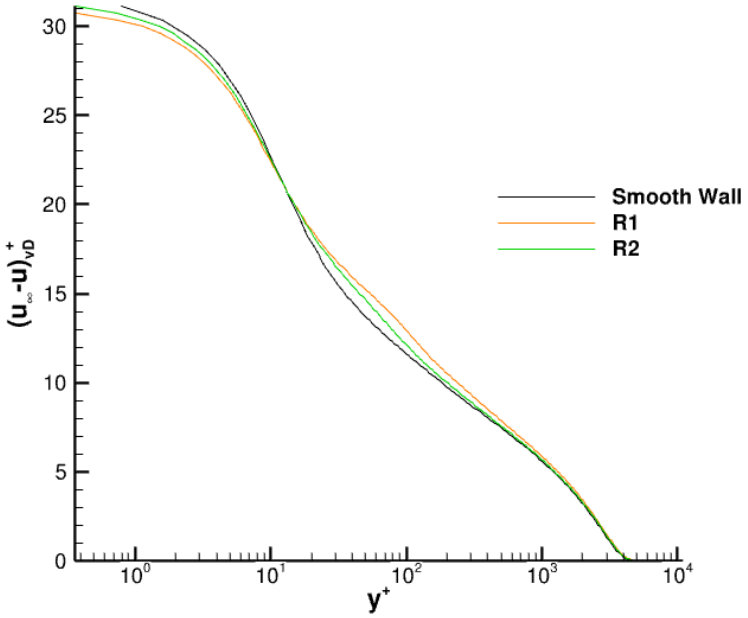

(b)

Figure 3.28. (a) The velocity profiles in outer scaling. (b) The velocity profiles as defect velocities in inner coordinates.

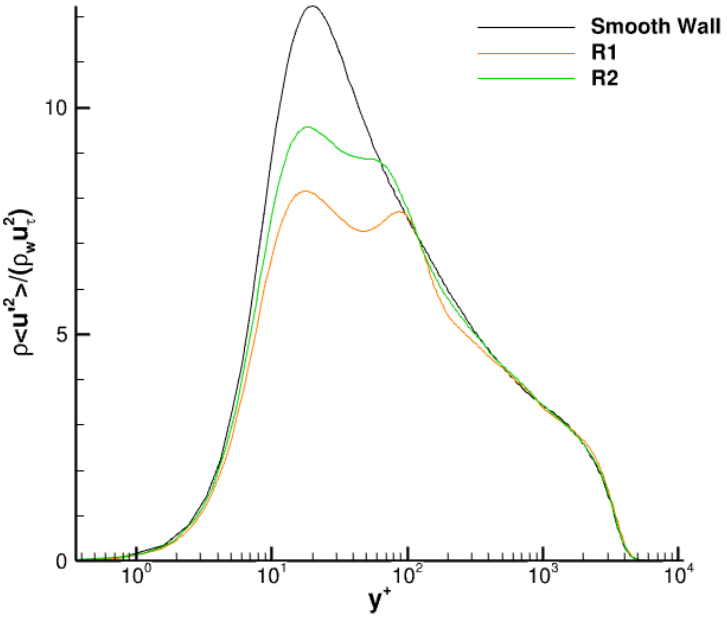

(a)

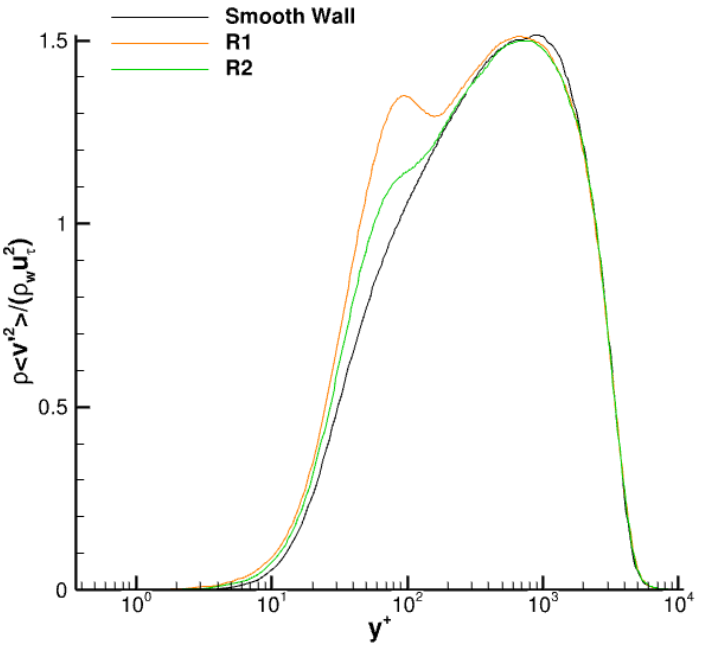

(b)

Figure 3.30 shows the Reynolds stresses in the outer layer. Here there seems to be a shift that was not seen on the semi-log axes. Figure 3.30a and 3.30d does not show the

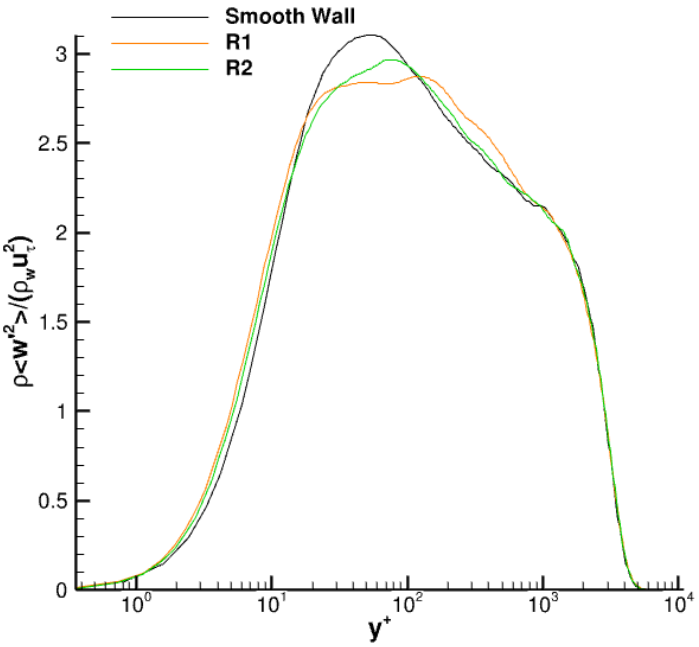

(c)

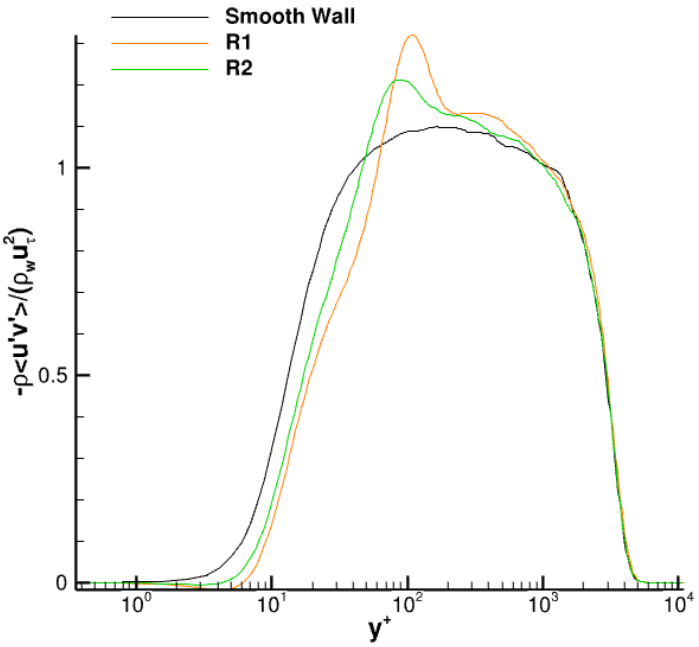

(d)

Figure 3.29. The different components of Reynolds stresses shown in inner units using Morkovin scaling.

entire boundary layer values for the sake of magnifying some of the differences between the cases. The values of $\overline{u'u'}$ do not seem to have major shifts from the smooth wall in the rough wall cases, however there are slight differences. It is in Figure 3.30b that the shift is more clearly seen starting from around $y/\delta = 0.25$. Each Reynolds stress component exhibits a different amount of the shift from the smooth wall case. The implications here could be that wall-similarity is not being observed, despite the collapse of the mean velocity profiles in the outer region. Most likely the Reynolds stresses are directly effected by the presence of the roughness which introduces a perturbation capable of transferring the energy of fluctuations in one direction to another. The fact the differences are observed in the outer region suggests that there may be nonlinear mechanisms which carry the information of the roughness from the small scales near the wall to the large scales in the outer region. The shapes of the profiles are similar though, and the profiles could possibly collapse onto each other if another scaling parameter was introduced which was related to the roughness effects (such as some form of k_s^+).

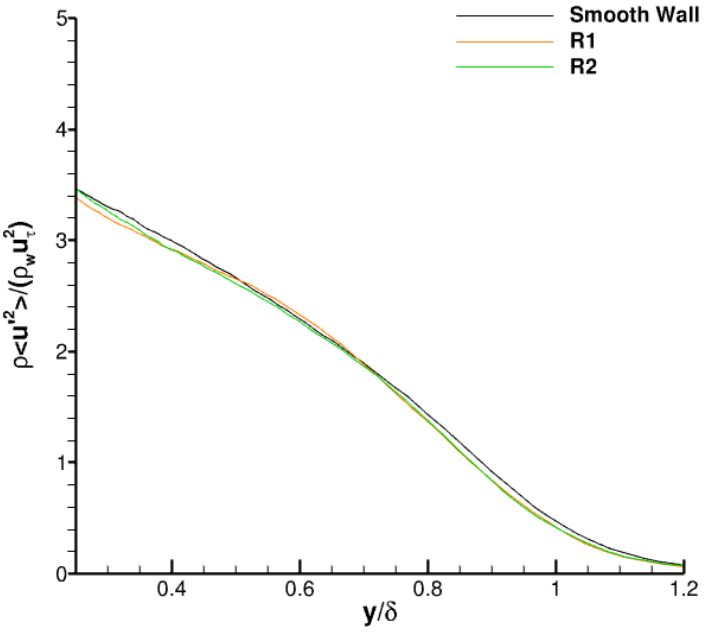
Smooth Wall
R1
R2
ρ<u'^2>/(ρ_w u_τ^2)
y/δ
0
1
2
3
4
5
0.4
0.6
0.8
1
1.2

(a)

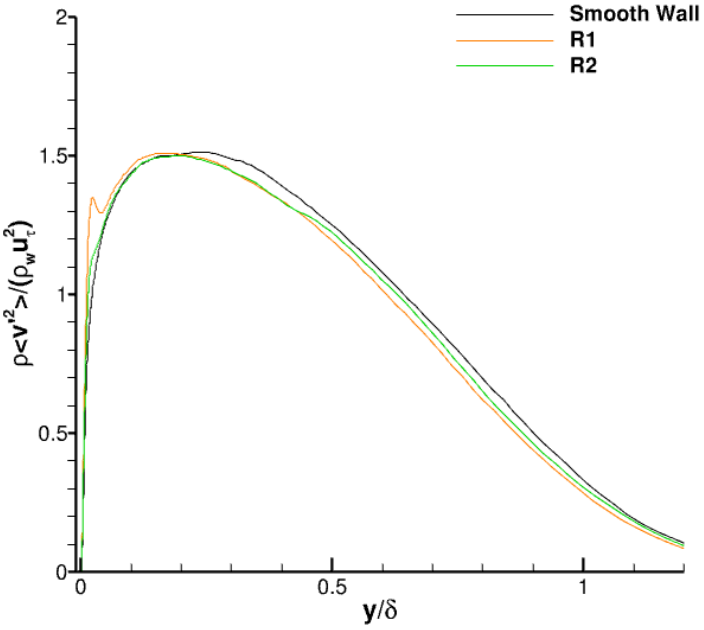
Smooth Wall
R1
R2
ρ<v'^2>/(ρ_w u_τ^2)
y/δ
0
0.5
1
1.5
2
0
0.5
1

(b)

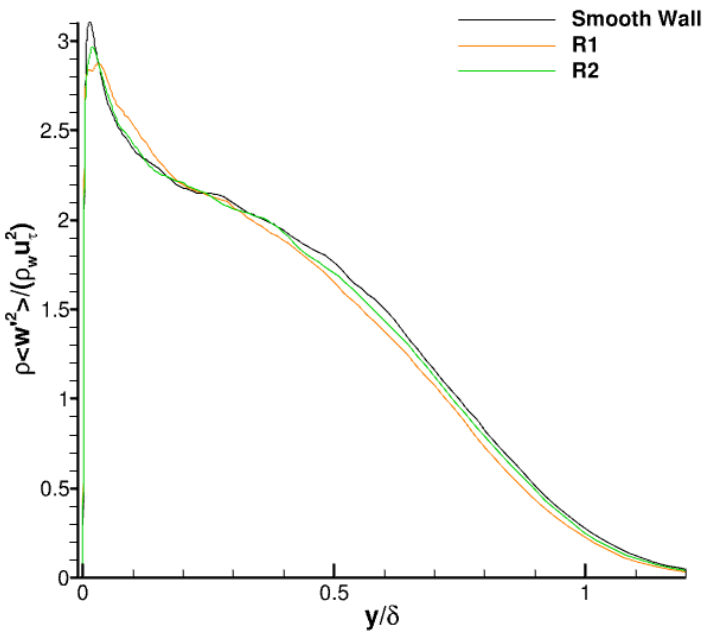

(c)

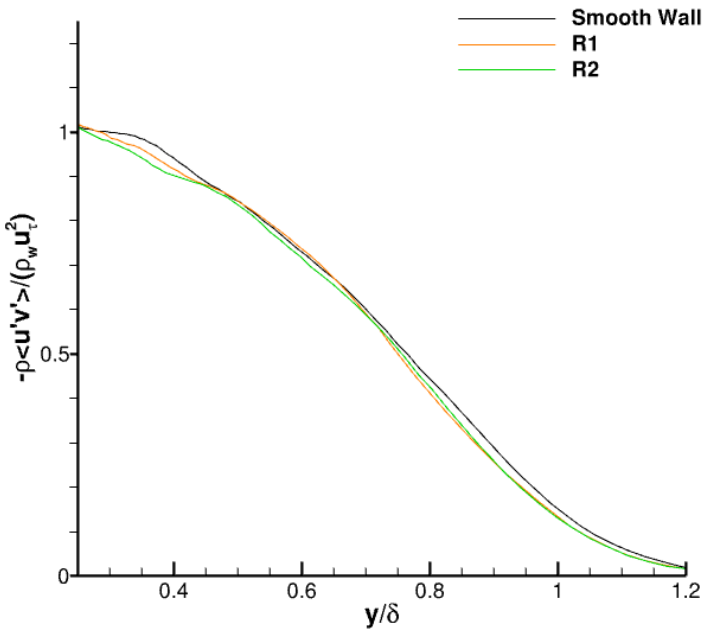

(d)

Figure 3.30. The different components of Reynolds stresses shown in inner units using Morkovin scaling as a function of y/δ.

3.2.6 Turbulent Kinetic Energy

Of particular interest is the distribution and generation of turbulent kinetic energy throughout the boundary layer. The turbulent kinetic energy (TKE) is related to the trace of the Reynolds stress tensor (R_{ij}) by

$$Tr(R_{ij}) = 2k = \overline{u'u'} + \overline{v'v'} + \overline{w'w'}. \tag{3.12}$$

The unscaled turbulent kinetic energy is shown in Figure 3.31. The choice to not scale the values was chosen so that the energy could be compared free of the differences in friction velocity. The distribution of energy shows that the smooth wall has much more turbulent kinetic energy in the buffer and logarithmic regions. This is reasonable since the roughness elements protrude into the logarithmic region and we may expect the turbulent fluctuations to be damped by the presence of the roughness elements. Further out in the boundary layer, the turbulent kinetic energy of the rough cases overtakes the smooth case. This could be a result of the energy of the logarithmic region being redistributed further into the boundary layer. An integration of these curves gives the total kinetic energy of each case. By order of least to most TKE the cases are Smooth Wall, Case R2, Case R1. Case R1 has the largest roughness elements and that seems to contribute more to the production of TKE.

The production of TKE (P) can be determine from

$$P = -R_{ij}\overline{u}_{i,j}. \tag{3.13}$$

In parallel shear flows, the dominant term is $-\overline{u'v'}\frac{\partial \overline{u}}{\partial \overline{y}}$. This dominant term was calculated and is referred to as the production of TKE in Figure 3.32. The value of the production was left unscaled since there seemed to be no change in the relative shapes of the plots when scaled with respective inner units. The location where this calculation was performed is a flat line across the span of the domain. In Figure 3.32 the importance of this production term seems to diminish as the roughness height is increased. The chosen location may bias the results here, since it is a flat location in the roughened domain. The rough walls introduce a 3-dimensionality to the flow that the smooth wall does not have. The presence of the

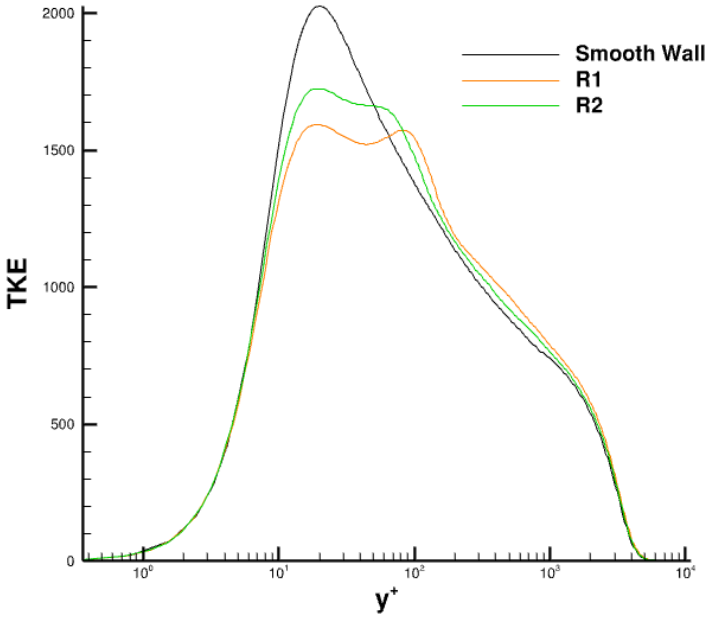

Figure 3.31. Unscaled turbulent kinetic energy of each case.

roughness may cause other production terms from equation 3.13 to be of more importance in some locations. Future work will involve probing locations which are not limited to flat spanwise locations to see how the importance of different production terms varies in relation to position of the roughness elements.

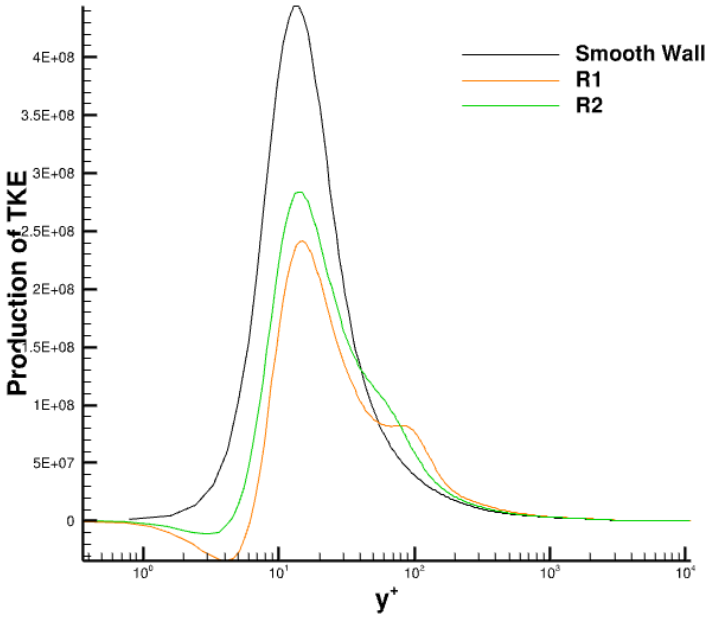

Figure 3.32. Unscaled production of TKE.

3.2.7 Power Spectral Density

In regards to the distribution of energy, not only is the distribution in the wall-normal direction of interest, but also the time-scales which hold energy are of interest. Computing a power spectral density is a method which can show how energy is distributed over either frequencies or wavenumbers of the flow. The spectra were calculated both on the surface using wall pressure and at a location of $y/\delta = 0.5$ using velocities. The spectra on the surface of the wall can be seen in Figure 3.33. The spectra are similar in each case with the exception of a deviation of the smooth wall case. This could be due to insufficient grid resolution which causes the energy to appear to gather at certain higher frequencies. However, the magnitudes in difference between the cases is very small, so the deviation of the smooth wall case may not be very significant.

Figure 3.34 shows the spectra taken along a line at $y/\delta = 0.5$. In the velocity spectra there do not appear to be any significant differences between the cases. This suggests that the energy is distributed similarly over different wavenumbers. For the nondimensionalizing

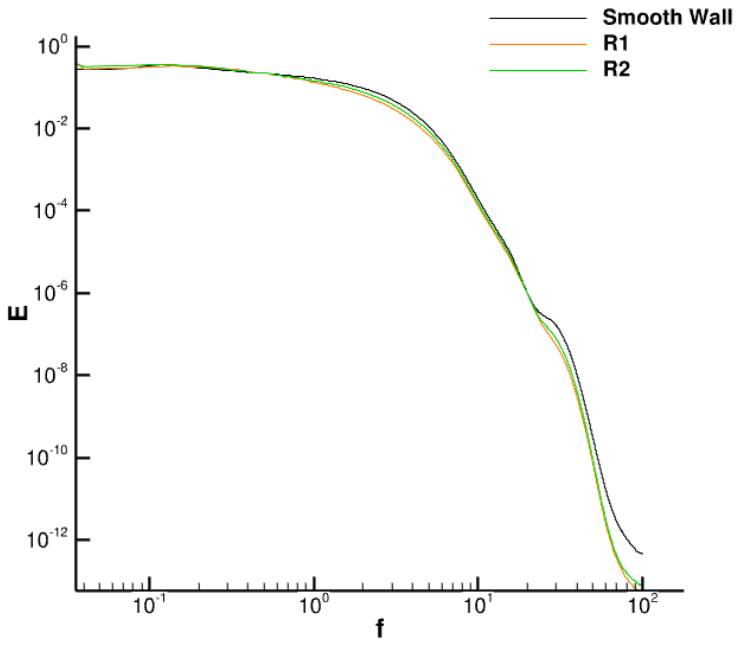

Figure 3.33. Frequency domain spectra on the surface.

of the terms, the Kolmogorov length scale (η) was computed. Given in inner units the value of η^+ for the smooth wall, Case R1, and Case R2 is respectively 6.5, 7.0, and 6.9.

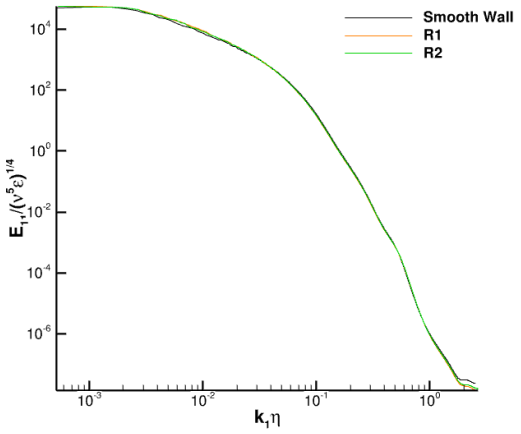

(a)

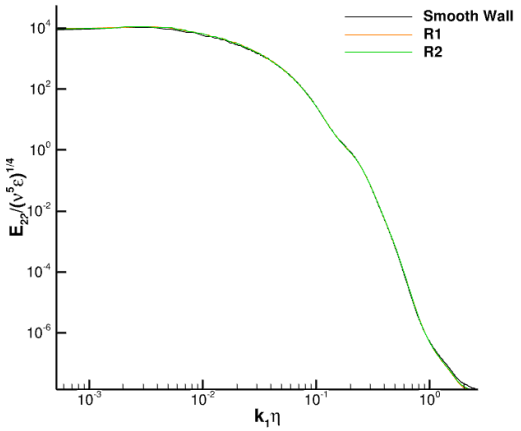

(b)

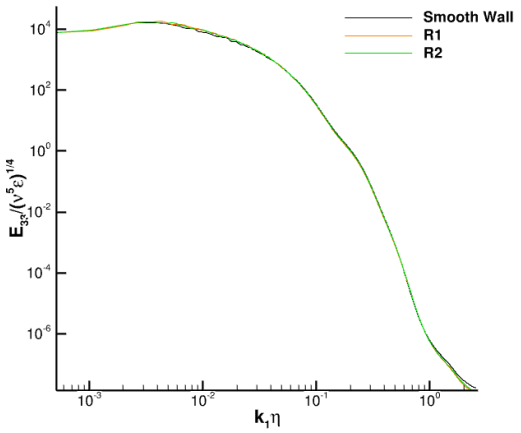

(c)

Figure 3.34. Velocity spectra taken at $y/\delta = 0.5$.

3.2.8 Probability Density Functions

Another tool to analyze a flow-field is probability density functions (PDF). When the PDF is integrated over a certain range of values, the result is the probability of observing a value between the limits of integration used. The total area under a PDF curve is equal to 1.0, meaning the PDF encompasses all possible values. For the three cases, PDF's were calculated for density (ρ) to observe how the density could vary according to the wall-normal distance in each case. The wall-normal locations chosen were the same from the visualized density contour slices (Figures 3.4, 3.11, 3.18). This way the differences that were seen in the density contours can potentially be quantified in the form of PDF's. The plots can be seen in Figure 3.35.

In Figures 3.35a 3.35b 3.35c there are differences between the smooth wall and rough wall cases. The primary difference is leftward shifted curves in the rough cases, meaning the density tends to be lower than the baseline smooth case. This intuitively is reasonable because the roughness elements act as sources of low-speed low-density fluid that comes from the surface of the roughness. The elements introduce a no-slip condition further from the wall than the smooth wall case and bring with it the changes in density.

In Figure 3.35d the curves seem to collapse on each other. This is what was observed in the density contours as well, where no discernible differences between the flow was seen. Figure 3.35e shows the curves are very similar as well at the edge of the boundary layer. This would be a piece of evidence perhaps in favor of the presence of wall-similarity in this flow. Smith and Smits [57] showed similar bimodal behavior of the PDF at a significant fraction of the boundary layer thickness ($y/\delta = 0.72$) for mass flow.

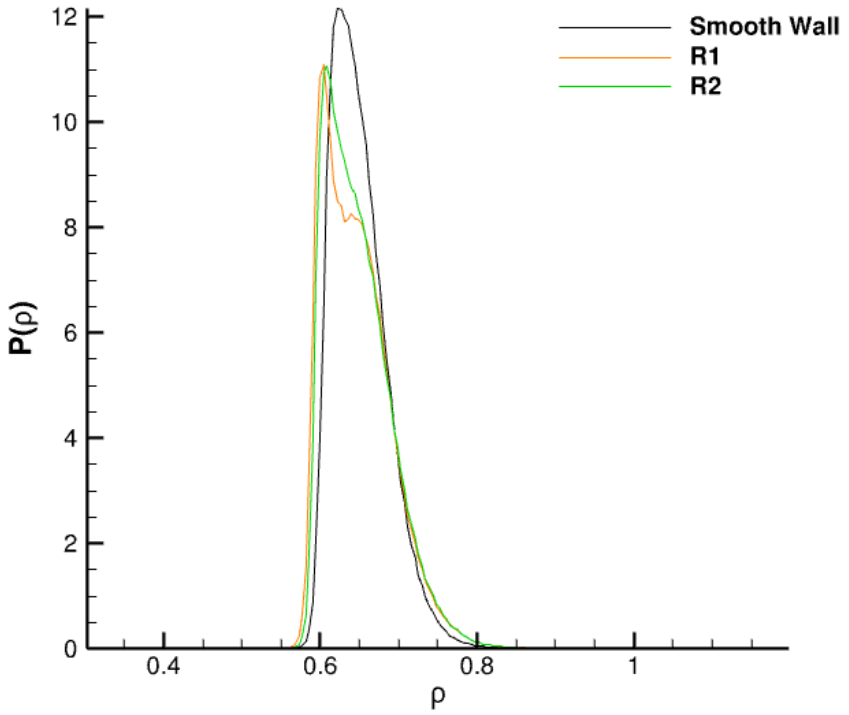

(a) $y^+ = 18$, $y/\delta = 0.005$

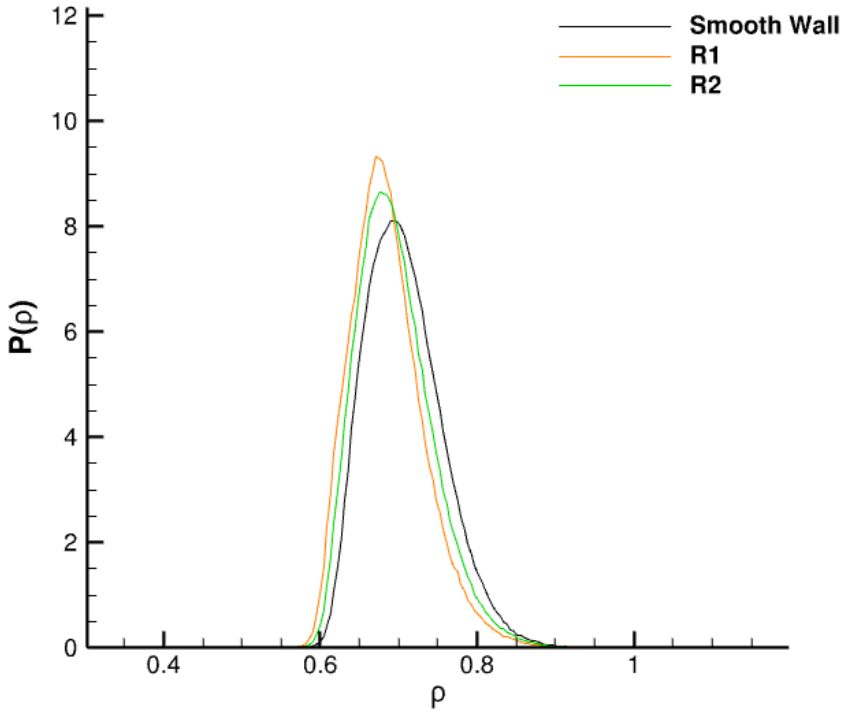

(b) $y^+ = 55$, $y/\delta = 0.015$

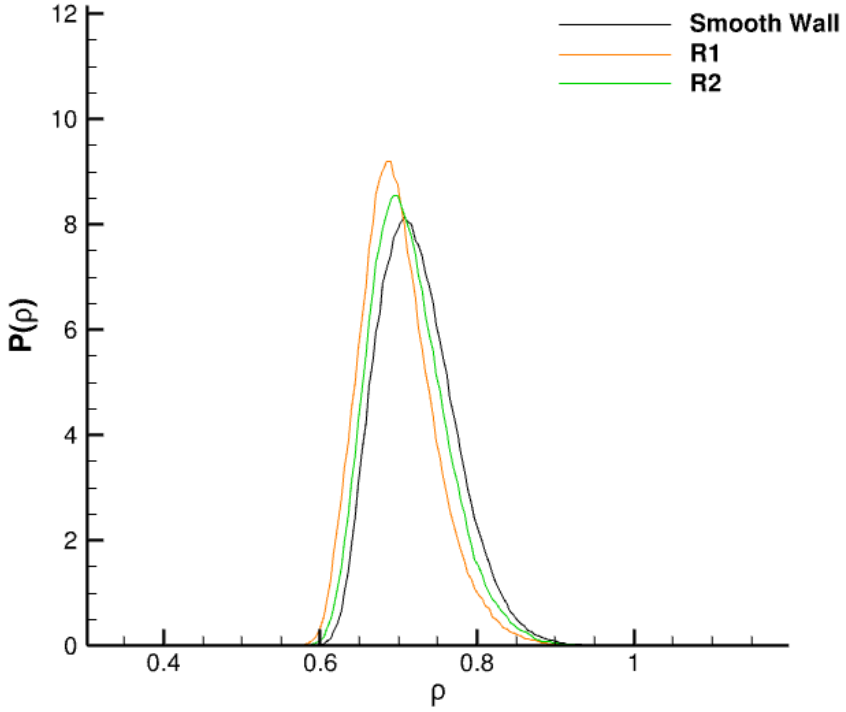

(c) $y^+ = 80$, $y/\delta = 0.021$

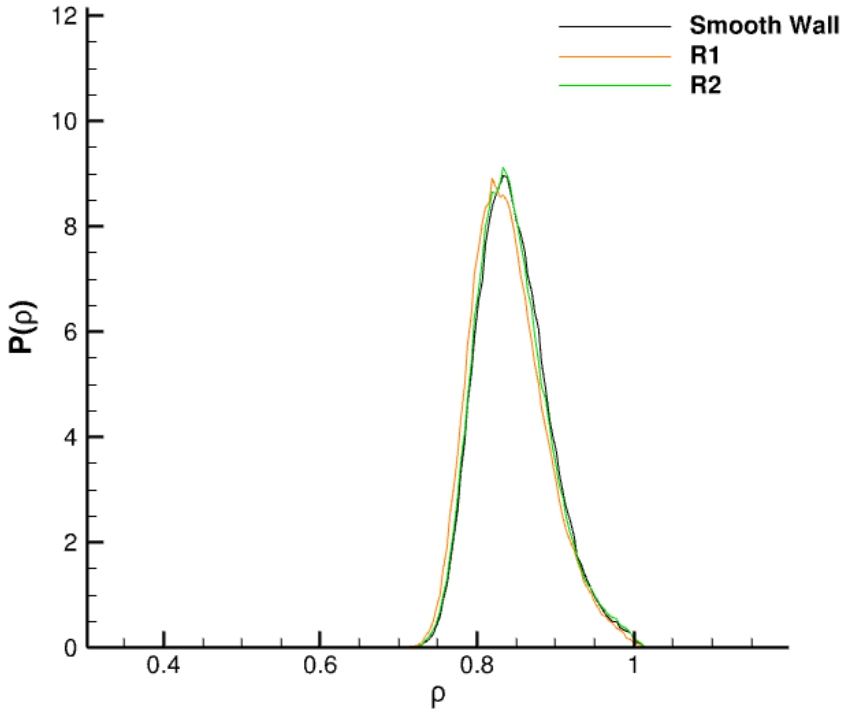

(d) $y^+ = 1100$, $y/\delta = 0.3$

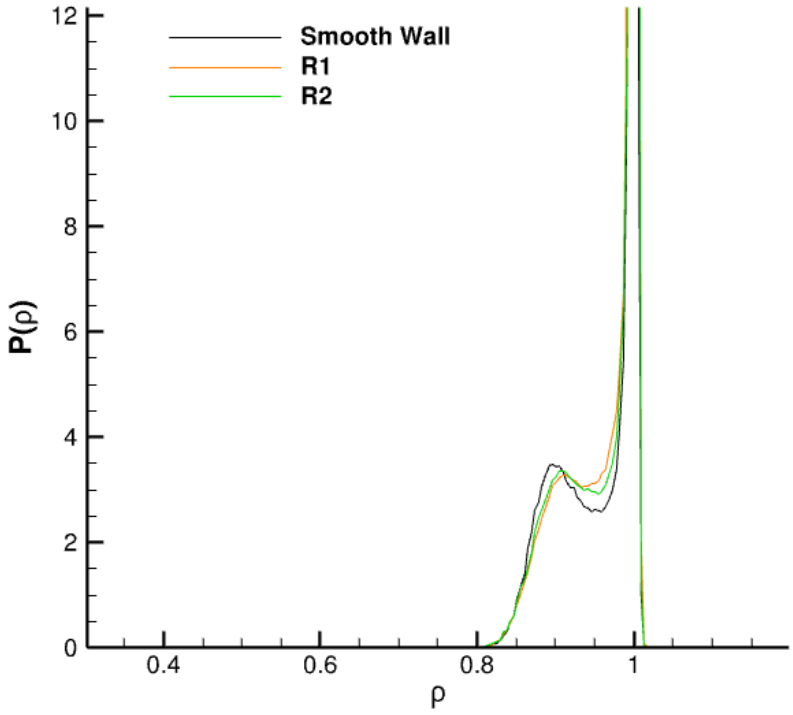

(e) $y^+ = 3480$, $y/\delta = 0.95$

Figure 3.35. Probability density functions of density at various wall-normal locations.

3.2.9 Heat Transfer

Heat transfer across the boundary layer is investigated in this section. The turbulent Prandtl number is the ratio of momentum diffusion to thermal diffusion. Many turbulence models will assume a turbulent Prandtl number of 0.85 [58] or 0.89 [59]. For these simulations, the nominal adiabatic wall temperature was selected. The turbulent Prandtl numbers were calculated for each case and are seen in Figure 3.36.

In Figure 3.36 the general constancy of the Prandtl number can be seen. The value is roughly 0.9 for each case. The roughly constant nature of the Prandtl number seems to deviate below $y^+ < 10$. Figure 3.36a shows a comparison from the smooth wall values to the values used in turbulence models. Some variation can be seen from the constant values of 0.85 and 0.89. Turbulence models may need to be adjusted in the future for the deviation from constancy.

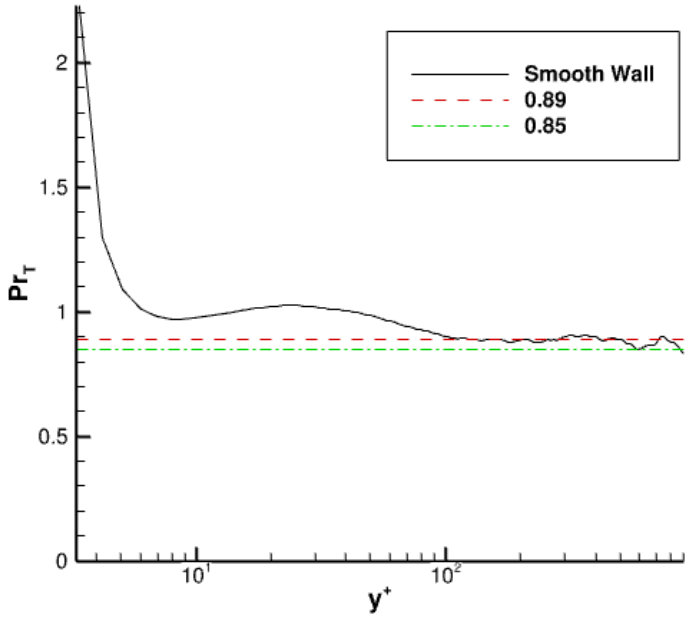

(a) Smooth Wall

Also of interest is the turbulent heat flux. This vector is an energy transport variable analogous to Reynolds stresses and are representative of the average correlations of velocity

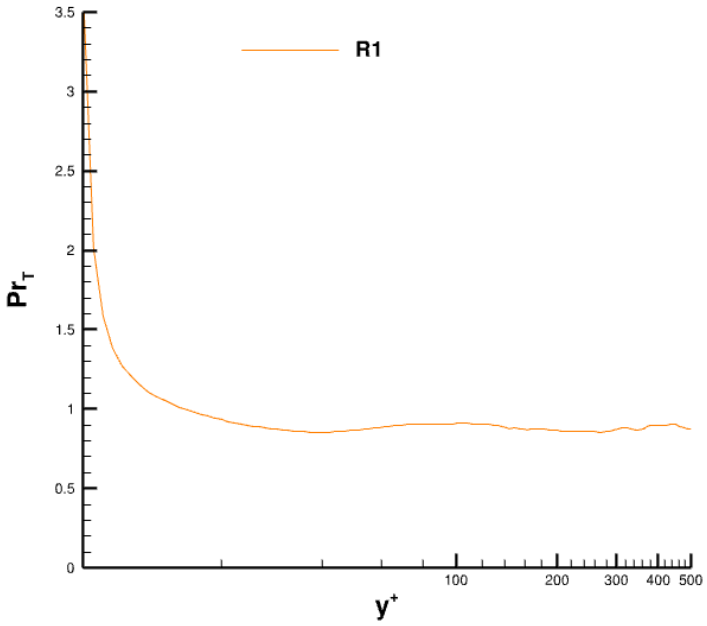

(b) Case R1

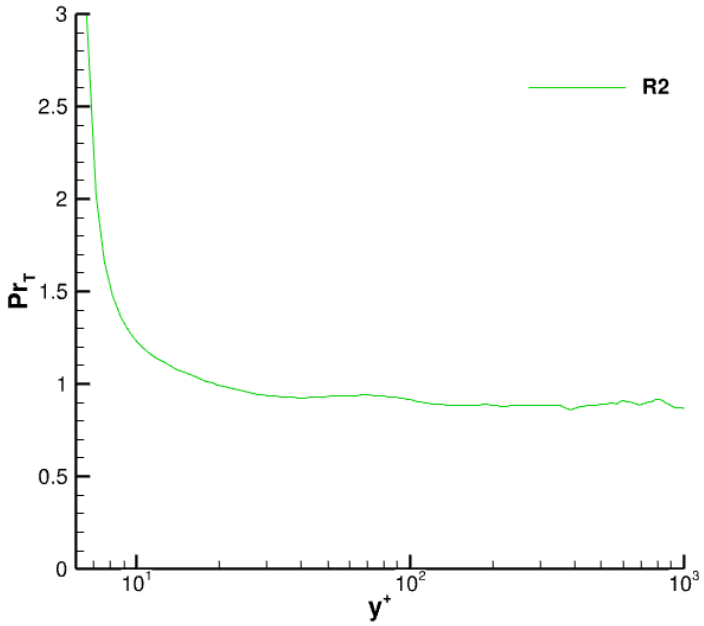

(c) Case R2

Figure 3.36. Turbulent Prandtl number for each case.

fluctuations with temperature fluctuations. Figure 3.37 shows the values of $\overline{u'T'}$ and $\overline{v'T'}$. There are differences between the smooth and rough cases. In all cases there is a negative correlation between u' and T'. The values of v' and T' are positively correlated. In all cases the profiles generally collapse above $y^+ > 1000$. This would again suggest wall-similarity is being observed since the direct effect of the roughness elements can be observed generally to $5k_s^+$.

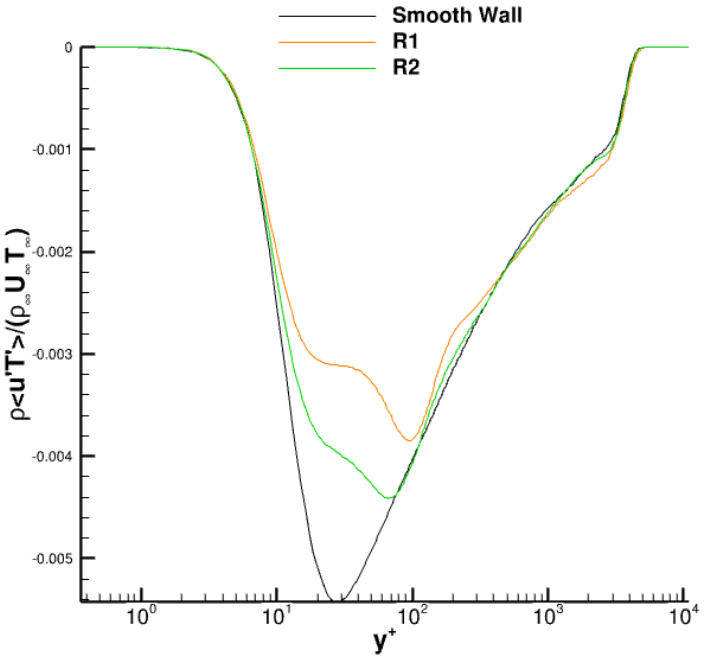

(a)

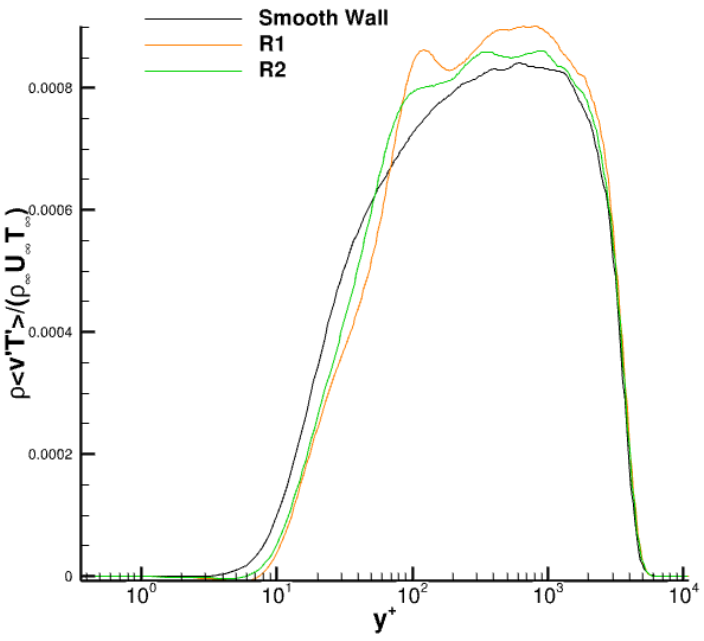

(b)

Figure 3.37. Turbulent heat fluxes.

4. CONCLUSIONS

This study aimed to investigate roughness effects on a compressible turbulent boundary layer. Wall-similarity was generally observed in all statistics with the exception of the Reynolds stresses. The Reynolds stresses show a slight shift downwards in the rough wall cases as compared to the smooth wall case. This is most likely due to a missing scaling parameter used in the scaling of the Reynolds stresses. The Reynolds stresses are scaled using inner units, which in compressible studies involves the Morkovin modified friction velocity. Inner units are derived without the assumption that some geometric length scale of the surface is a relevant scaling parameter. In rough wall flows, a scaling parameter which involves some geometry of the roughness topology may be necessary. The current study was classified as transitionally rough due to the friction on the surface being from viscous forces as opposed to form drag on the roughness elements (by an order of magnitude).

The presence of roughness elements near the wall disturbs the near wall streaks when observed in constant y planes with contours of density. Though the streaks are difficult to observe, when using a three dimensional method such as Q-criterion the vortices which are associated with the streaks can be observed again. Plotting planes of constant wall-normal distance also shows the presence of streaks which group together due to the presence of the roughness elements. Depending on the height of the roughness elements, the vortices associated with the streaks tend to stack themselves, as opposed to being quasi-planar in the smooth wall case. Some hypothesis have suggested that disruption of these streaks can affect wall-normal motions in the flow, and subsequently large scale motions in the flow. The streaks have also been observed to become more fine with larger Reynolds numbers [47]. The vortices associated with the streaks observed in this study seem resilient and organize themselves around the roughness elements. Wall-similarity is also generally observed in studies with high enough Reynolds numbers [26]. The current author's hypothesis is that at low Reynolds numbers, the streaks and associated vortices have a characteristic width which is on the order of the width of the roughness elements, and can be easily disturbed. This would result in a loss of wall-similarity. As Reynolds numbers increase, the characteristic width of the streaks would tend to become more fine and easily organize around the roughness

topology. The streaks are allowed to develop into wall-normal motions and wall-similarity is upheld. A series of tests with various Reynolds numbers would be needed to investigate this hypothesis.

Future work would involve the continued analysis of the given data. The production of turbulence should be investigated at different locations relative to the roughness elements. Two-point correlations to investigate the average sizing of turbulent structures is also in progress. A RANS computation with a transition model (to mimic the effect of the body force trip in the simulations) is in progress so that the ILES data from this study can be compared to modeled data. To gather further data on compressible turbulent rough wall studies that may be useful, a set of experiments with various Reynolds numbers and an increased effective slope of the surface geometry may be needed. A simulation which also shows shock waves and expansion fans on the roughness elements may prove useful as well since that phenomena has been observed in many high-speed flows. To ensure resolution between the roughness elements is sufficient, it would be useful to maintain a stricter DNS grid spacing where $\Delta x_{\mathrm{i}} < 5$ including at the boundary layer edge. Investigating the behavior of vortices near the wall may be of interest. DNS studies provide unique opportunities to investigate these structures and perhaps could provide clarity on the effects they hold in the boundary layer.

REFERENCES

[1] G. Hagen, *Über den Einfluss der Temperatur auf die Bewegung des Wassers in Röhren*. Berlin: Kgl. Akademie der Wiss, 1854.

[2] H. Darcy, *Recherches expérimentales relatives au mouvement de l'eau dans les tuyaux*. Paris, Mallet-Bachelier, 1857.

[3] J. Jiménez, "Turbulent flows over rough walls," *Annual Review of Fluid Mechanics*, vol. 36, no. 1, pp. 173–196, 2004. DOI: 10.1146/annurev.fluid.36.050802.122103.

[4] J. Nikuradse, *Laws of flow in rough pipes*. [Online]. Available: https://ntrs.nasa.gov/citations/19930093938.

[5] C. F. Colebrook, "Turbulent flow in pipes, with particular reference to the transition region between the smooth and rough pipe laws.," *Journal of the Institution of Civil Engineers*, vol. 11, no. 4, pp. 133–156, 1939. DOI: 10.1680/ijoti.1939.13150. [Online]. Available: https://doi.org/10.1680/ijoti.1939.13150.

[6] L. Moody, "Friction factors for pipe flow," *ASME Trans.*, vol. 66, pp. 671–684, 1944.

[7] M. Kadivar, D. Tormey, and G. McGranaghan, "A review on turbulent flow over rough surfaces: Fundamentals and theories," *International Journal of Thermofluids*, vol. 10, p. 100 077, 2021, ISSN: 2666-2027. DOI: https://doi.org/10.1016/j.ijft.2021.100077, This article was published in International Journal of Thermofluids, Vol. 10, Mohammadreza Kadivar and David Tormey and Gerard McGranaghan, A review on turbulent flow over rough surfaces: Fundamentals and theories, 100077, Copyright Elsevier 2021.

[8] M. J. Lighthill, "The structure of turbulent shear flow," *Journal of Fluid Mechanics*, vol. 1, no. 5, pp. 554–560, 1956. DOI: 10.1017/S0022112056210366.

[9] A. E. Perry and M. S. Chong, "On the mechanism of wall turbulence," *Journal of Fluid Mechanics*, vol. 119, pp. 173–217, 1982. DOI: 10.1017/S0022112082001311.

[10] M. R. Raupach, R. A. Antonia, and S. Rajagopalan, "Rough-wall boundary layers," *Applied Mechanics Reviews*, vol. 44, pp. 1–25, 1991.

[11] J. Anderson, *Fundamentals of Aerodynamics*. McGraw Hill Education, 2017, pp. 34–40.

[12] S. B. Pope, *Turbulent Flows*. Cambridge University Press, 2020.

[13] T. Wei and W. Willmarth, "Reynolds-number effects on the structure of a turbulent channel flow," *Journal of Fluid Mechanics*, vol. 204, no. 5, pp. 57–95, 1989.

[14] D. Coles, "The law of the wake in the turbulent boundary layer," *Journal of Fluid Mechanics*, vol. 1, no. 2, pp. 191–226, 1956. DOI: 10.1017/S0022112056000135.

[15] D. B. Spalding, "A Single Formula for the "Law of the Wall"," *Journal of Applied Mechanics*, vol. 28, no. 3, pp. 455–458, Sep. 1961, ISSN: 0021-8936. DOI: 10.1115/1.3641728.

[16] H. Reichardt, "Vollständige Darstellung der turbulenten Geschwindigkeitsverteilung in glatten Leitungen," *ZAMM - Journal of Applied Mathematics and Mechanics / Zeitschrift für Angewandte Mathematik und Mechanik*, vol. 31, no. 7, pp. 208–219, 1951. DOI: https://doi.org/10.1002/zamm.19510310704.

[17] S. Kline and S. K. Robinson, "Quasi-coherent structures in the turbulent boundary layer. I - status report on a community-wide summary of the data," 1990.

[18] S. Robinson, "Coherent motions in the turbulent boundary layer," *Annual Review of Fluid Mechanics*, vol. 23, pp. 601–639, 1991.

[19] J. Gaskins, J. Poggie, and G. A. Blaisdell, "A preliminary study of roughness effects on a compressible turbulent boundary layer," in *AIAA Scitech 2021 Forum*. DOI: 10.2514/6.2021-1445.

[20] M. R. Head and P. Bandyopadhyay, "New aspects of turbulent boundary-layer structure," *Journal of Fluid Mechanics*, vol. 107, pp. 297–338, 1981.

[21] A. E. Perry, S. Henbest, and M. S. Chong, "A theoretical and experimental study of wall turbulence," *Journal of Fluid Mechanics*, vol. 165, pp. 163–199, 1986.

[22] A. E. Perry and I. Marusic, "A wall–wake model for the turbulence structure of boundary layers," *Journal of Fluid Mechanics*, vol. 298, pp. 361–388, 1995.

[23] M. Schultz and K. Flack, "Outer layer similarity in fully rough turbulent boundary layers," *Experiments in Fluids*, vol. 38, pp. 328–340, 2005.

[24] F. H. Clauser, "Turbulent boundary layers in adverse pressure gradients," *Journal of the Aeronautical Sciences*, vol. 21, no. 2, pp. 91–108, 1954. DOI: 10.2514/8.2938.

[25] F. R. Hama, "Boundary-layer characteristics for rough and smooth surfaces," *Society of Naval Architects and Marine Engineers*, 1954.

[26] K. A. Flack and M. P. Schultz, "Roughness effects on wall-bounded turbulent flows," *Physics of Fluids*, vol. 26, no. 10, p. 101 305, 2014. DOI: 10.1063/1.4896280.

[27] K. A. Flack, M. P. Schultz, and J. S. Connelly, "Examination of a critical roughness height for outer layer similarity," *Physics of Fluids*, vol. 19, no. 9, p. 095 104, 2007. DOI: 10.1063/1.2757708.

[28] M. P. Schultz and K. A. Flack, "The rough-wall turbulent boundary layer from the hydraulically smooth to the fully rough regime," *Journal of Fluid Mechanics*, vol. 580, pp. 381–405, 2007. DOI: 10.1017/S0022112007005502.

[29] J. Jiménez and P. Moin, "The minimal flow unit in near-wall turbulence," *Journal of Fluid Mechanics*, vol. 225, pp. 213–240, 1991. DOI: 10.1017/S0022112091002033.

[30] E. Napoli, V. Armenio, and M. De Marchis, "The effect of the slope of irregularly distributed roughness elements on turbulent wall-bounded flows," *Journal of Fluid Mechanics*, vol. 613, pp. 385–394, 2008. DOI: 10.1017/S0022112008003571.

[31] M. P. Schultz and K. A. Flack, "Turbulent boundary layers on a systematically varied rough wall," *Physics of Fluids*, vol. 21, no. 1, p. 015 104, 2009. DOI: 10.1063/1.3059630.

[32] A. Musker, "Universal roughness functions for naturally-occurring surfaces," *Transactions of the Canadian Society for Mechanical Engineering*, vol. 6, no. 1, pp. 1–6, 1980. DOI: 10.1139/tcsme-1980-0001.

[33] S. Beck and R. Collins. "Moody diagram." (2016), [Online]. Available: https://en.wikipedia.org/wiki/Moody_chart#/media/File:Moody_EN.svg. accessed: 2021-07-01.

[34] R. M. Latin and R. D. W. Bowersox, "Flow properties of a supersonic turbulent boundary layer with wall roughness," *AIAA Journal*, vol. 38, no. 10, pp. 1804–1821, 2000. DOI: 10.2514/2.862.

[35] R. M. Latin and R. D. W. Bowersox, "Temporal turbulent flow structure for supersonic rough-wall boundary layers," *AIAA Journal*, vol. 40, no. 5, pp. 832–841, 2002. DOI: 10.2514/2.1749.

[36] B. D. Kocher, C. S. Combs, P. A. Kreth, and J. D. Schmisseur, "Characterizing the streamwise development of surface roughness effects on a supersonic boundary layer," in *2018 Fluid Dynamics Conference*. DOI: 10.2514/6.2018-4047.

[37] I. W. Ekoto, R. D. W. Bowersox, T. Beutner, and L. Goss, "Supersonic boundary layers with periodic surface roughness," *AIAA Journal*, vol. 46, no. 2, pp. 486–497, 2008. DOI: 10.2514/1.31729.

[38] I. W. Ekoto, R. D. W. Bowersox, T. Beutner, and L. Goss, "Response of supersonic turbulent boundary layers to local and global mechanical distortions," *Journal of Fluid Mechanics*, vol. 630, pp. 225–265, 2009. DOI: 10.1017/S0022112009006752.

[39] S. J. Peltier, R. A. Humble, and R. D. W. Bowersox, "Crosshatch roughness distortions on a hypersonic turbulent boundary layer," *Physics of Fluids*, vol. 28, no. 4, p. 045 105, 2016. DOI: 10.1063/1.4944657.

[40] D. Sahoo, A. Smits, and M. Papageorge, "PIV experiments on a rough wall hypersonic turbulent boundary layer," AIAA paper 2010-4471. DOI: 10.2514/6.2010-4471.

[41] J. Poggie, N. J. Bisek, and R. Gosse, "Resolution effects in compressible, turbulent boundary layer simulations," *Computers and Fluids*, vol. 120, pp. 57–69, 2015. DOI: https://doi.org/10.1016/j.compfluid.2015.07.015.

[42] F. M. White, *Viscous Fluid Flow*, 2nd. McGraw-Hill, New York, 1991.

[43] N. J. Mullenix, D. V. Gaitonde, and M. R. Visbal, "Spatially developing supersonic turbulent boundary layer with a body-force-based method," *AIAA Journal*, vol. 51, no. 8, pp. 1805–1819, 2013. DOI: 10.2514/1.J051861.

[44] J. Poggie, "Large-scale structures in implicit large-eddy simulation of compressible turbulent flow," AIAA paper 2014-3328. DOI: 10.2514/6.2014-3328.

[45] R. M. Beam and R. F. Warming, "An implicit factored scheme for the compressible navier-stokes equations," *AIAA Journal*, vol. 16, no. 4, pp. 393–402, 1978. DOI: 10.2514/3.60901.

[46] D. Garmann, "Characterization of the vortex formation and evolution about a revolving wing using high-fidelity simulation," University of Cincinnati, 2013. [Online]. Available: https://etd.ohiolink.edu/.

[47] S. Pirozzoli and M. Bernardini, "Turbulence in supersonic boundary layers at moderate reynolds number," *Journal of Fluid Mechanics*, vol. 688, pp. 120–168, 2011. DOI: 10.1017/jfm.2011.368.

[48] S. Pirozzoli and M. Bernardini, "Probing high-reynolds-number effects in numerical boundary layers," *Physics of Fluids*, vol. 25, no. 2, p. 021 704, 2013. DOI: 10.1063/1.4792164.

[49] L. Duan, I. Beekman, and M. P. Martin, "Direct numerical simulation of hypersonic turbulent boundary layers. part 2. effect of wall temperature," *Journal of Fluid Mechanics*, vol. 655, pp. 419–445, 2010. DOI: 10.1017/S0022112010000959.

[50] L. Duan, I. Beekman, and M. P. Martin, "Direct numerical simulation of hypersonic turbulent boundary layers. part 3. effect of mach number," *Journal of Fluid Mechanics*, vol. 672, pp. 245–267, 2011. DOI: 10.1017/S0022112010005902.

[51] M. V. Morkovin, "Effects of compressibility on turbulent flows.," *Mécanique de la turbulence,*, A. Favre, Ed., pp. 367–380, 1962, CNRS.

[52] E. R. Van Driest, "Turbulent boundary layer in compressible fluids," *Journal of Spacecraft and Rockets*, vol. 40, no. 6, pp. 1012–1028, 2003. DOI: 10.2514/2.7048.

[53] F. H. Clauser, "The Turbulent Boundary Layer," in ser. Advances in Applied Mechanics, H. Dryden and T. von Kármán, Eds., vol. 4, Elsevier, 1956, pp. 1–51. DOI: https://doi.org/10.1016/S0065-2156(08)70370-3.

[54] T. Wei, R. Schmidt, and P. McMurtry, "Comment on the clauser chart method for determining the friction velocity," *Experiments in Fluids*, vol. 38, pp. 695–699, 2005. DOI: https://doi.org/10.1007/s00348-005-0934-3.

[55] E. R. Van Driest, "On turbulent flow near a wall," *Journal of the Aeronautical Sciences*, vol. 23, no. 11, pp. 1007–1011, 1956. DOI: 10.2514/8.3713.

[56] N. J. Georgiadis, D. P. Rizzetta, and C. Fureby, "Large-eddy simulation: Current capabilities, recommended practices, and future research," *AIAA Journal*, vol. 48, no. 8, pp. 1772–1784, 2010. DOI: 10.2514/1.J050232.

[57] M. W. Smith and A. J. Smits, "Visualization of the structure of supersonic turbulent boundary layers," *Experiments in Fluids*, vol. 18, pp. 288–302, 1995. DOI: https://doi.org/10.1007/BF00195099.

[58] W. M. Kays, "Turbulent Prandtl number—where are we?" *Journal of Heat Transfer*, vol. 116, no. 2, pp. 284–295, May 1994, ISSN: 0022-1481. DOI: 10.1115/1.2911398.

[59] S. Roy and K. Sinha, "Turbulent heat flux model for hypersonic shock–boundary layer interaction," *AIAA Journal*, vol. 57, no. 8, pp. 3624–3629, 2019. DOI: 10.2514/1.J058334.